Eva Gasser, BSc

Characterization of Gas and Particles Released During Thermal Runaway of Li-ion Batteries

MASTER'S THESIS

to achieve the university degree of

Diplom-Ingenieurin

Master's degree programme: Advanced Materials Science

submitted to

Graz University of Technology

Supervisor

Ao.Univ.-Prof. DI Dr Werner Grogger
Co-Supervisor: DI Dr Armin Zankel

Institute of Electron Microscopy and Nanoanalysis

Graz, May 2019

AFFIDAVIT

I declare that I have authored this thesis independently, that I have not used other than the declared sources/resources, and that I have explicitly indicated all material which has been quoted either literally or by content from the sources used. The text document uploaded to TUGRAZonline is identical to the present master's thesis.

Date

Signature

Abstract

Developing and improving lithium-ion (Li-ion) batteries for the application in electrical vehicles represents a highly relevant field of research. One of the main challenges is the increase of the range, which the vehicle can drive without recharging the battery. This goal can be achieved by raising the energy density of the Li-ion batteries. However, a higher energy density also goes along with safety hazards.

Failure of the Li-ion cells, e.g. caused by traffic accidents, poor cell design or manufacturing flaws can lead to exothermic reactions. The result is a self-accelerating chain reaction (thermal runaway), producing high amounts of heat together with the release of gases and solid particles from the cells.

In this Master's thesis the particles and gases which are released from Li-ion cells during thermal runaway are investigated. The gases were analyzed using gas chromatography (GC) and Fourier transformation infrared spectroscopy (FTIR). One of the main goals was to establish and to quantify the composition of the released gases.

Particle analysis was performed using scanning electron microscopy (SEM) combined with energy dispersive X-ray spectroscopy (EDX). The aim was to characterize the size distribution of the particles and to analyze the elemental composition, which provides information about the compounds formed from solid battery components during thermal runaway.

For this analysis, it is highly relevant to collect a representative sample of the particles. To this end, several methods for sampling the particles were developed and compared. Additionally, the difficulties of analyzing particles in the micrometer range are described and discussed in this work.

The overall outcome of this thesis is the development of a strategy for SEM analysis of the particles and an enhanced characterization of the particles and gases formed during thermal runaway. These results may contribute to the assessment of the health hazard of Li-ion batteries undergoing thermal runaway.

Kurzzusammenfassung

Die Entwicklung und Verbesserung von Lithium-Ionen-Batterien für Elektrofahrzeuge ist ein aktuell hoch relevantes Forschungsfeld. Eine der größten Herausforderungen ist dabei die Erhöhung der Reichweite der Fahrzeuge, die erreicht werden kann, ohne die Batterie wieder aufzuladen. Dieses Ziel kann durch Steigern der Energiedichte der Li-Ionen-Batterie erreicht werden. Jedoch steigt mit der Energiedichte auch das Sicherheitsrisiko.

Fehler einer Batteriezelle, beispielsweise ausgelöst durch einen Verkehrsunfall, schlechtes Zelldesign oder Herstellungsfehler können zu exothermen Reaktionen in der Zelle führen. Dies führt wiederum zu einer sich selbst beschleunigenden Kettenreaktion (Thermal Runaway), wodurch eine große Menge an Wärme sowie Gase und Partikel aus der Zelle freigesetzt werden.

Diese Masterarbeit untersucht die Partikel und Gase, die beim Thermal Runaway einer Li-Ionen-Zelle entstehen. Die Gase wurden mittels Gaschromatographie (GC) und Fourier-Transform-Infrarotspektroskopie (FTIR) analysiert. Eines der Hauptziele war es, die Komponenten des freiwerdenden Gases zu bestimmen und zu quantifizieren.

Die Partikelanalyse wurde mit einem Rasterelektronenmikroskop (REM), das mit einem Detektor für energiedispersive Röntgenspektroskopie (EDX) ausgestattet ist, durchgeführt. Das Ziel war es, die Größenverteilung der Partikel und die elementare Zusammensetzung zu charakterisieren. Die Zusammensetzung liefert Informationen über die Verbindungen, die beim Thermal Runaway aus festen Bestandteilen der Batterie entstehen.

Für diese Analyse ist es notwendig, eine repräsentative Probe der Partikel zu sammeln. Dazu wurden verschiedene Probenahme-Methoden verglichen. Zudem werden in dieser Arbeit die Schwierigkeiten einer Analyse von mikrometergroßen Partikeln beschrieben und diskutiert.

In dieser Arbeit wurde eine Vorgangsweise entwickelt, um Partikel, die durch einen Thermal Runaway entstehen, zu charakterisieren. Es wurde ein verbessertes Verständnis über die Zusammensetzung der durch den Thermal Runaway gebildeten Gase und Partikel erreicht. Diese Ergebnisse können dazu beitragen, die beim Thermal Runaway von Li-Ionen-Batterien entstehende Gesundheitsgefahr besser zu beurteilen.

Acknowledgements

This thesis was performed in collaboration between the Institute of Electron Microscopy and Nanonanalysis (FELMI, TU Graz) and Virtual Vehicle Research Center. The FELMI together with the Center for Electron Microscopy is also known as Austrian Center for Electron Microscopy and Nanoanalysis (FELMI-ZFE). The Center for Electron Microscopy is member of Austrian Cooperative Research (ACR).

The setup of the electron microscope Sigma 300 VP was enabled by the project "HRSM-Projekt ELMINet Graz" (cooperation of KFU, MedUni und TUG), which was financed by the Austrian Federal Ministry of Education, Science and Research (BMBWF). The combination with the EDX detector could be realized by the project "Innovative Materialcharakterisierung" (SP2016-002-006), which is part of "ACR Strategisches Projektprogramm 2016" of the Austrian Cooperative Research (ACR), where a support by the Austrian Federal Ministry for Digital and Economic Affairs is to be mentioned.

VIRTUAL VEHICLE Research Center in Graz is funded by the COMET Programme of the Federal Ministry for Transport, Innovation and Technology (BMVIT), the Federal Ministry for Digital, Business and Enterprise (BMDW), the Austrian Research Promotion Agency (FFG), the Province of Styria and the Styrian Business Promotion Agency (SFG).

The topic of this thesis is part of the K-project SafeBattery, funded by BMVIT, BMDW, Austria and Land Styria within the program COMET – Competence Centers for Excellent Technologies. The strategic objectives of COMET are: developing new expertise by initiating and supporting long-term research co-operations between science and industry in toplevel research, and establishing and securing the technological leadership of companies. By advancing and bundling existing strengths and by integrating international research expertise Austria is to be strengthened as a research location for the long term.

Furthermore, I would like to express my thanks to the supporting industrial and scientific project partners, namely Kreisler Electric GmbH, AVL LIST GmbH, Daimler AG, Robert Bosch AG, SFL technology GmbH, AUDI AG, Dr. Ing. h.c. F. Porsche AG, the Graz University of Technology (TU Graz), the Vehicle Safety Institute (VSI, TU Graz) and the Institute for Chemistry and Technology of Materials (ICTM, TU Graz).

I want to express my gratitude to all the people who supported me during this thesis. First, I would like to thank Prof. Werner Grogger for supervising this thesis and for his support. Special thanks go to Armin Zankel for all his guidance, for our insightful and enriching discussions and for always being available for my many questions during my thesis. Moreover, I am grateful to Manfred Nachtnebel for his patience and time in supporting me with my SEM measurements. In addition, I would like to thank all my colleagues at FELMI-ZFE for helping me with any questions and for the friendly working atmosphere.

I am grateful to the Virtual Vehicle Research Center for a great 6-month internship in the course of this thesis, and for providing a fascinating research topic. In particular, I would like to express my gratitude to Christiane Essl for her proficient advices and guidance. In addition, a very big thank to Rene Planteu, Oliver Korak and Bernhard Rasch for all their help in the laboratory. Further, I wish to thank Alexander Thaler and Andrej Golubkov and all my colleagues of the battery group. I have really enjoyed working at the Virtual Vehicle Research Center and I have learned a lot.

Last but not least, I am thankful to my partner for morally supporting me during writing this thesis, and for discussing numerous chemical questions with me. Finally, I want to cordially thank my parents and my entire family for all their support and encouragement during the time of my studies.

Table of Contents

1. Introduction

1.1 General Information

The first electric car was developed in 1834. However, electric cars disappeared by 1930, since fuel-based cars got more popular due to their cost-efficiency. During the oil crises in the 1970s, some countries were temporarily interested in electric cars. In the last few years there is again a growing interest in the development of electric vehicles. One of the main driving forces is climate change. Fossil fuel-based vehicles drastically contribute to climate change, due to the emission of greenhouse gases. Therefore, alternatives to fossil fuels are highly desired.[1]

In general, the climate is strongly changing since the beginning of industrialization, mainly caused by greenhouse gas emissions, including carbon dioxide (CO_2), methane (CH_4) and nitrous oxide (N_2O). Nowadays, the transport sector is one of the main causes of greenhouse gas emissions in Austria, corresponding to 29 % of the total emissions. The emission in this sector has dramatically increased by 66 % since 1990. Additionally, in the European Union (EU) and worldwide, a crucial contribution to greenhouse gas emissions comes from the transport sector and has strongly increased since 1990 (*Figure 1.1*). Fossil fuel-based vehicles deliver high carbon dioxide (CO_2) and nitrogen oxide (NO_x) emissions and massively contribute to the fine particulate pollution. Electrical cars have the potential to minimize these pollutions and emissions. Therefore, the EU commission aims to reduce the number of fossil fuel-based cars by 50 % until 2030 and eliminating them until 2050.[2,3]

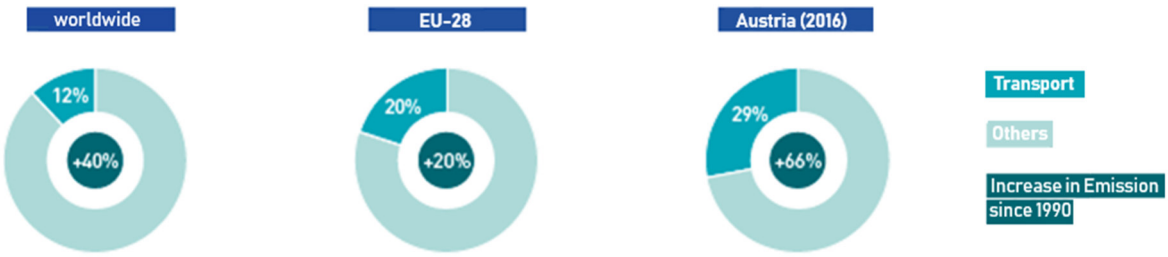

Figure 1.1: *Contribution and increase of transport sector to greenhouse gas emission worldwide, in the EU and Austria.*[3]

To reach this goal, the batteries used for electric vehicles have to be improved. The most important type of batteries for electric vehicles are lithium ion (Li-ion) batteries, which consist of electrodes with a host structure for Li-ions. Among other factors, the success of Li-ion batteries is due to their high specific energy and their light weight compared to other battery types.

Alternative types of batteries which are used for electric vehicles are valve-regulated-lead-acid (VRLA) batteries and nickel-metal-hydride (NiMH) batteries. Lead acid batteries use metallic lead as the negative electrode and lead dioxide as the positive electrode. They provide save and maintenance free operation and are cost-effective. However, they have a low specific energy and short lifetime. Nickel-metal-hydride (NiMH) batteries consist of a nickel oxide anode and a metal-hydride cathode. They are expensive due to a high nickel demand and they provide an insufficient specific energy for pure electric vehicles.[4]

Although Li-ion batteries have a high specific energy, an average electric car with a battery pack of about 220 L can merely reach approximately a range of 150 – 200 km. This is a considerably lower distance compared to a fossil-fuel car.[5] To reach greater distances, batteries with higher energy density are necessary. In the last years, enormous developments towards battery cells with high energy density have been performed. State-of-the-art batteries feature higher energy densities without significantly increased masses or costs of the battery.[3]

To increase the energy density further, the electrode material may have to be changed. For example, the anode may have to be changed from graphite to a mixture of silica and carbon and the cathode may have to be changed from LFP (lithium iron phosphate) to a Ni rich NMC (nickel manganese cobalt) cathode. The disadvantage of such high energy density batteries is that they are less safe. The main risk factor of batteries with high energy density is that they can undergo thermal runaway more easily. Thermal runaway is characterized by an overheating of the battery, going along with the release of gases and particles into the environment.[6]

Thermal runaway can be caused for example by a poor cell design, cell manufacturing flaws or external abuse of the cell (e.g. due to traffic accidents). If a thermal runaway happens, exothermic reactions occur in the cell, which accelerate further reactions and result in a highly overheated cell, reaching temperatures higher than 1000°C.[7] Thus, a significant amount of gases are released. The composition of these gases has been characterized previously. These gases include carbon monoxide (CO), carbon dioxide (CO_2), methane (CH_4), hydrogen fluoride (HF), hydrogen (H_2), ethane (C_2H_6) and ethylene (C_2H_4), which are partly toxic and easily flammable.[8,9,10]

1.2 Thesis Outline

This thesis examines the thermal runaway of Li-ion batteries triggered by cell abuse. As described above, a thermal runaway causes venting of gases from the battery cell. The composition of the gas mixture depends on the battery design (e.g. the used cathode material, electrolytes etc.). In this work, the vent gas of four batteries is analyzed using gas chromatography (GC) and Fourier transformation infrared spectroscopy (FTIR). To achieve a quantitative determination of the gases, the gas chromatograph was calibrated.

Additionally, the particles of the cell are analyzed using a scanning electron microscope (SEM) equipped with an energy dispersive X-ray detector (EDX). This analysis is performed in order to gain information about the particle size distribution and the elemental composition of the particles.

Analyzing small particles with scanning electron microscopy is fraught with difficulties, since various effects occur, which affect the accuracy. In this respect, a standard is measured and Monte-Carlo simulations are performed, in order to diminish errors. Since SEM analysis is performed with a very small amount of particles, it is essential to collect a representative sample. An appropriate sampling method is therefore crucial for the SEM analysis of particles generated during thermal runaway. However, a standard procedure for sampling such particles has not been described in literature yet. In this work, several methods for sampling the particles generated during thermal runaway are developed and compared to each other.

This thesis consists of eight chapters. Chapter 2 provides a basic introduction about Li-ion batteries and their safety. In Chapter 3, the used methods (GC, FTIR and SEM/EDX) are explained and a literature overview of the sample preparation of the particles is given. Chapter 4 describes the performed thermal runaway experiments and how the gas and particle analysis were carried out. In Chapter 5, the calibration of the GC and the gases, which are detected from the Li-ion battery after thermal runaway, are described and discussed. Chapter 6 discusses pretests of the particle analysis and the final results of SEM/EDX analysis of the particles released from the Li-ion batteries during thermal runaway. Chapter 7 gives a conclusion of the thesis and in Chapter 8 the references are listed.

2. Basics of Li-ion Batteries

Li-ion batteries are typically used as the electrochemical energy storage system for electric vehicles. The advantages of Li-ion batteries comprise a high cycle-resistivity and a high energy density. In addition, they are lighter than other battery types and they do not have a memory effect (no capacity loss after frequent partial discharges).[7]

In this chapter the components as well as the basic principles of Li-ion batteries are described.

2.1 Components of Li-ion Cells

The major components of Li-ion cells are two electrodes (anode and cathode), a separator between these electrodes, an electrolyte consisting of a salt dissolved in an organic solvent and additives to improve the properties of the battery. Additionally, a so-called solid electrolyte interface (SEI) is formed at the anode during the first charge. The setup of a Li-ion cell is shown in *Figure 2.1*. A battery comprises several cells, which are connected in series.

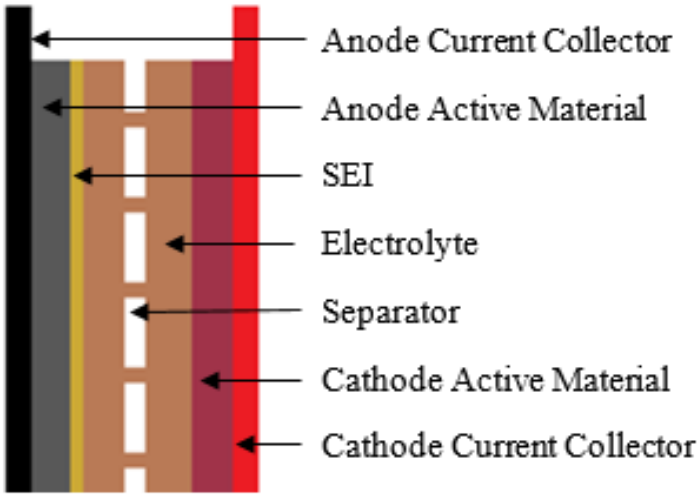

Figure 2.1: *Components of a Li-ion cell*

2.1.1 Electrodes

The positive electrode (cathode) and negative electrode (anode) consist of a current collector, which is coated with an active material. For the coating, the powdery active material is mixed with a binder such as polyvinylidene difluoride (PVdF).

Cathode

The cathode is made of an aluminum foil, which works as the current collector, and an active material such as $LiCoO_2$ (LCO), $LiFePO_4$ (LFP), $LiMn_2O_4$ (LMO), $LiNi_xCo_YMn_zO_2$ (NMC)

and $LiNi_{0.8}Co_{0.15}Al_{0.05}O_2$ (NCA). Among others, an important requirement for the active material is that the Li-ions can intercalate and deintercalate reversibly.[7]

Anode

The current collector of the anode is made of copper. Aluminum cannot be used as anode material, since lithium reacts with aluminum at low potentials. The current collector is usually coated with a blend of the graphitic carbon or treated graphite and a binder. Appropriate materials should exhibit high electric conductivity, whereas the irreversible capacity loss as well as the volume change during (dis)charging are expected to be low.[7, 11]

2.1.2 Separator

The electrodes are separated by a polyolefin film, which electrically disconnects the electrodes, but is permeable for the Li-ions. Therefore, the separator should be an electrical isolator and should have a minimal electrolyte (ionic) resistance. Additionally, the separator should be chemically, mechanically and geometrically stable. Typically, the separator is about 30 µm thin and consists of a microporous film of polypropylene or polyethylene or laminates of both. These materials are used since they have the required mechanical properties as well as high chemical stability and they are cost-effective.[7]

2.1.3 Electrolyte

A salt dissolved in an organic solvent represents the electrolyte. The usually used solvents are ethylene carbonate (EC), ethyl methyl carbonate (EMC), propylene carbonate (PC), dimethyl carbonate (DMC) and diethyl carbonate (DEC). $LiPF_6$ is the preferred salt, because it has the best combination of properties including conductivity, ionic mobility as well as thermal and chemical stability. It is essential that the electrolyte is conductive for ions but insulating for electrons.[7]

2.1.4 Additives

Electrolyte additives are used to change and improve the properties of the electrolyte. For example, flame-retardant agents, overcharge protection agents and cathode protection agents can be added. Even minimal amounts of additives have a significant impact on the performance of the battery.[7]

2.1.5 Solid Electrolyte Interface (SEI)

During the first charge, a layer between anode and electrolyte is formed by decomposition of the electrolyte. This layer is called solid electrolyte interface. The formation of the SEI is the

primary reason for the irreversible capacity loss during the first charge. However, it also has various benefits. It has a high electronic resistivity, mechanical stability and flexibility, as well as a good adhesion to the anode. The SEI prevents further decomposition of the electrolyte, since it disconnects the anode and electrolyte. It is beneficial for the safety and the cycle-resistivity of the battery. Without the formation of the SEI, the anode would be destroyed faster, since the graphite layer would extent and contract during charging and discharging. The quality of the SEI depends on the electrolyte, while some electrolytes lead to an insufficient or no SEI. EC forms a very good SEI and therefore it is added to nearly every electrolyte. Additionally, additives are added to improve the formation of the SEI. For that the additive vinylene carbonate (VC) is commonly used.[7, 11]

2.2 Principle of a Li-ion battery

In a battery cell, chemical energy is converted into electrical energy. The electrochemical discharging reaction of a Li-ion battery is almost reversible, allowing multiple conversions of chemical energy into electrical energy. To achieve a high cell voltage, the difference between the redox potentials of the anode and cathode should be high.[12]

Figure 2.2 schematically presents the discharging process of a Li-ion cell. During discharging the negative electrode releases electrons (oxidation), whereas the positive electrode accepts electrons (reduction). During charging, the reduction happens at the negative electrode and an oxidation at the positive electrode. At the anode, by definition, an oxidation process and at the cathode a reduction occurs. Since the oxidation and reduction is changing, there is a convention that the name of the electrodes is given according their function during discharge.[12]

While electrons are moving also Li-ions move through the electrolytes to the electrodes. During discharging, the Li-ions deintercalate from the anode into the cathode via the electrolyte and during charging, Li-ions intercalate back into the anode.[7]

The following equations show the reactions of the anode (active material Li_xC_n), cathode (active material LiMO, (M = Co, Mn, Ni)) and the overall cell reaction during discharge. During charging the reverse reaction occurs.[12]

Anode: $Li_xC_n \rightarrow C_n + xLi^+ + xe^-$

Cathode: $Li_{1-x}MO_2 + xe^- + xLi^+ \rightarrow LiMO_2$

Cell reaction: $Li_{1-x}MO_2 + Li_xC_n \rightarrow LiMO_2 + C_n$

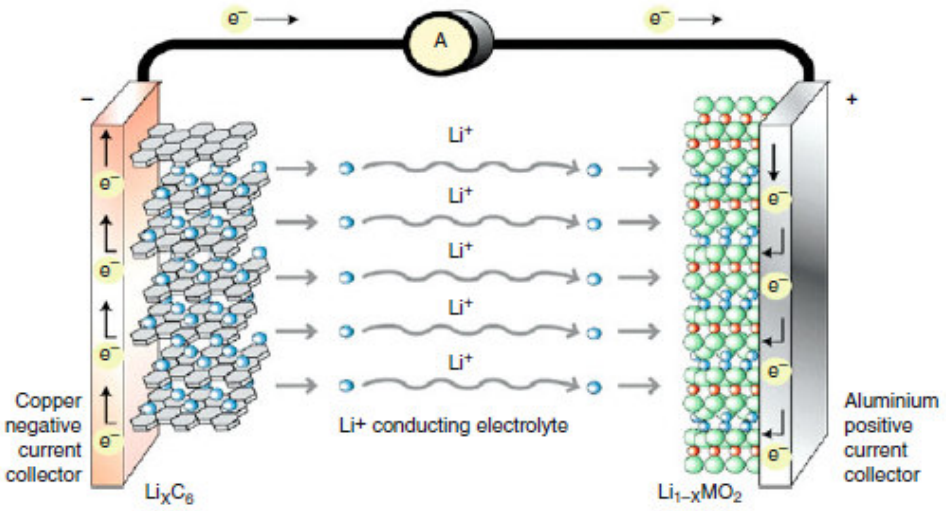

Figure 2.2: *Discharging process of a Li-ion cell* [7]

2.3 Design of a Li-ion battery

There are different kinds of housings for Li-ion batteries. Commonly used types are cylindric, prismatic and pouch cells (*Figure 2.3*, left). The housings of these cells are made of metal. Typically, aluminum and stainless steel are used for cylindric and prismatic cells and a refined aluminum polymer composite foil for pouch cells. A metal housing has to be used since it prevents humidity to enter the cell, resulting in a reaction of water and the conductive salt ($LiPF_6$) to hydrogen fluoride (HF). This could lead to a leak out of the electrolyte. Pouch cells are built up with a stacking technology (*Figure 2.3*, right). Unit cells consisting of a cathode, separator and the anode are repeated many times within one cell.[11]

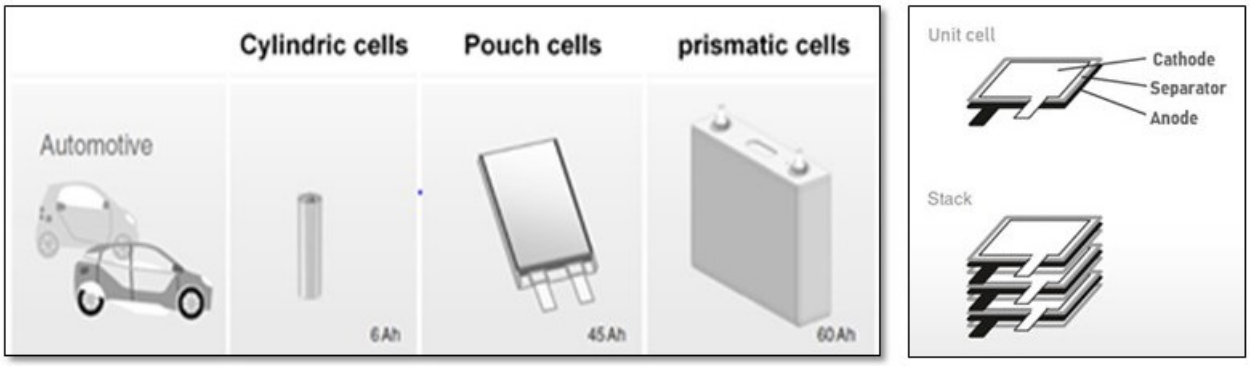

Figure 2.3: *left: comparison of cylindric, pouch and prismatic cells; right: stacking technology of a pouch cell.*[11]

2.4 Safety of Li-ion Batteries

A main concern of electric vehicles is their safety because of the large amount of Li-ion batteries. With the request of reaching bigger distances, the trend goes to Li-ion batteries with higher energy density, resulting in a bigger safety problem. If it comes to the worst, an abuse condition can lead to a thermal runaway. To increase the safety of batteries, various improvements are implemented, such as passive defense systems and warning systems. However, there is also much research on material modifications.

2.4.2 Thermal Runaway (TR)

The reasons of a battery to undergo thermal runaway can be separated into mechanical abuse, electrical abuse, thermal abuse and internal short circuits (ISC, see *Figure 2.4*). Mechanical abuse, like collision and crash, can lead to a deformation of the battery. This may result in a leakage of the flammable electrolyte or in the connection of anode and cathode, leading to an ISC. Another cause of an ISC can be penetration of the battery.[6]

One type of electrical abuse are external short circuits. The electrodes can get connected by various ways such as contamination with conductors and water immersion. Overcharge as well as overdischarge are further types of electrical abuse. Overcharge mostly occurs because of a failure of the battery management system (BMS). During overcharge, heat and gases are generated. Heat generation is caused by ohmic heat and side reactions. Gas generation is initiated by excessive deintercalation of Li-ions in the cathode, producing molecular oxygen. Subsequently, the oxygen reacts with the electrolyte and decomposes it. The vast amount of gas can open the safety valve, so that the active material gets in contact with air, producing further excessive gas. A failure of the BMS can also lead to an overdischarge. The overdischarge can cause a capacity loss of the battery because of different reasons, including the amorphization of the cathode, the formation of a new SEI after it is deposed by delithiation as well as deposition of Cu on the anode, resulting in the dissolution of the copper collector.[6]

Thermal abuse can be a result of mechanical and electrical abuse or contact loss of the cell connector. In the case of contact loss, high current flows through the affected part, generating a large amount of heat. Another cause of thermal abuse can be a fire in the car, for example due to a electrolyte leak.[6]

However, the main reason for thermal runaway is an internal short circuit. Beside the above-mentioned reasons, the ISC can also be self-induced by defects or impurities from

manufacturing, which may take a long period of time (several months). Therefore, it is possible to detect this failure by the BMS.[6]

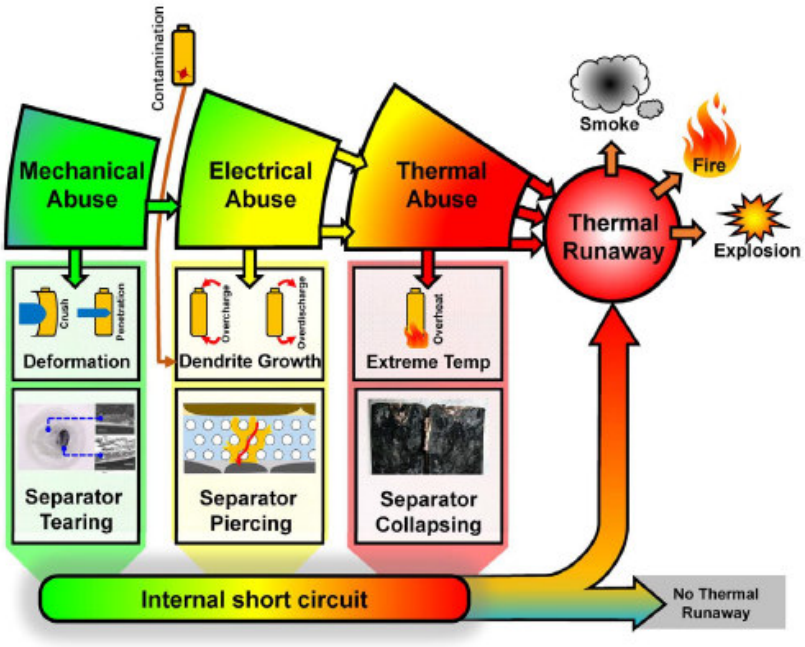

Figure 2.4: *Abuse conditions of batteries resulting in thermal runaway.*[6]

Thermal Runaway Mechanism

All described types of abuse increase the temperature in the battery, favoring further follow-up reactions. Finally, a chain reaction is induced, and the battery undergoes thermal runaway (*Figure 2.5*)[6].

The TR starts with the decomposition of the SEI, followed by simultaneous recombination and decomposition of the SEI. Upon reaching 250°C, the structure of the graphite anode collapses.[6]

Concerning the cathode, decomposition occurs after its onset temperature is reached, and further exothermic reactions are triggered afterwards. The stability of the cathode during TR depends on the cathode material. The onset temperatures of the different cathodes vary between 150°C and 310°C.[6]

During TR, the electrolyte reacts with the anode and the cathode and leads to electrolyte decomposition. Additionally, the electrolyte itself can decompose. An example includes the reaction of $LiPF_6$ to LiF and PF_5. The amount of generated heat can depend on the amount of electrolyte. The total heat generation for LCO cathodes is independent from the electrolyte, whereas for LMO the amount of electrolyte influences it.[6]

The TR also affects the separator, which typically consists of porous polypropylene (PP) or polyethylene (PE) with a melting point of around 170°C and 130°C, respectively. The pores close when the melting point is reached. In principle, this is favorable to avoid abuse conditions. However, shrinkage of the separator upon melting can result in a short circuit. A safer alternative is a trilayer separator consisting of PP/PE/PP. Among these polymers, PE exhibits the lowest melting point and will therefore melt first, while the outer layer remains stable until its melting point is reached. Another option is to use a separator with a ceramic coating, which collapses at a temperature of approximately 200-260°C. To prevent an ISC, the collapse temperature of the separator has to be higher than the decomposition temperature of the cathode and the anode.[6]

Thermal runaway can even induce a fire. To ignite a fire, a flammable fuel, an ignition source and oxygen is needed. The organic solvent of the electrolyte and some of the generated gases are highly flammable. Ignition sources include the arc generated by the external short current and the friction between the high-speed outflow and the safety valve. Within the cell, insufficient oxygen is produced to inflame. However, a fire can be triggered once the gases escape out of the cell to the air.[6]

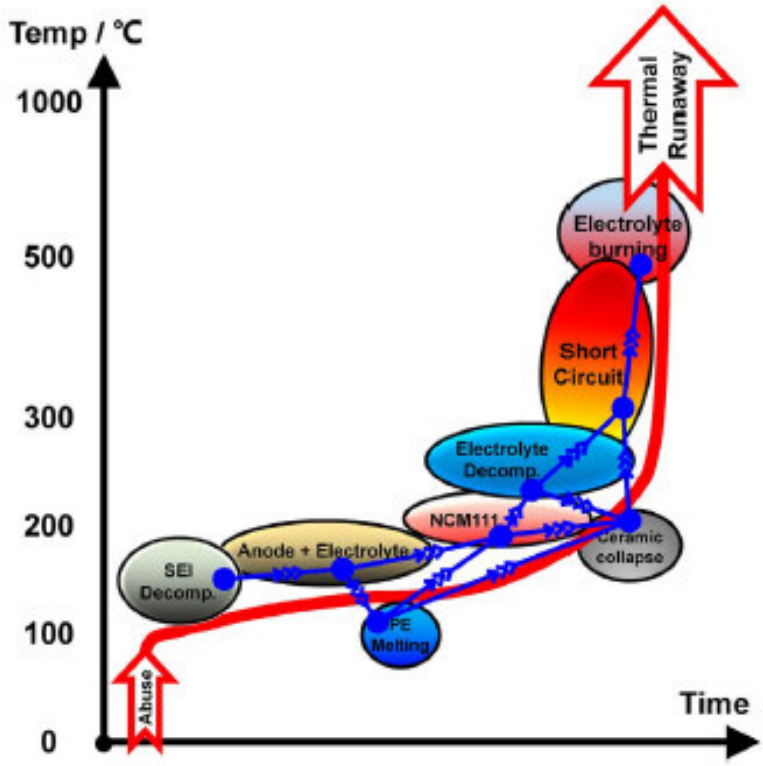

Figure 2.5: *Chain reaction during thermal runaway.*[6]

2.4.3 Safety Improvements

There are various strategies to improve the safety of batteries, including material modification as well as passive defense systems. Another important aspect is minimizing the hazard after a TR already occurred.[6]

The safety of the battery can be greatly improved by applying electrode materials with increased thermal stability, since highly stable electrodes can cut off the chain reactions. Surface coating represents a feasible way to stabilize the electrodes. The coating of the cathode can consist of e.g. phosphates, fluoride and solid oxide and for the anode e.g. Al_2O_3 can be used. Also, diverse additives can be added to the electrolyte, which (among other factors) support the formation of the SEI, improve the flame-retardant and protect the battery of overcharge. $LiPF_6$ as the typical salt of the electrolyte is also problematic, since its decomposition products catalyze the decomposition of the SEI. The separator can be improved with a trilayer arrangement, as described above, and materials with higher collapse temperature.[6]

An important way to prevent a thermal runaway after occurrence of a failure is the battery management system (BMS), which can detect faults and diagnose them. Also, electronic devices like fuses and PTCs can inhibit a thermal runaway of a battery.[6]

In case there is no possibility to prevent the thermal runaway, early detection systems can be applied in order to warn the passenger, and to provide enough time to escape from danger.[6]

3. Methods

3.1 Chromatography

3.1.1 Basics

Chromatography is a method to separate a sample into its components and to analyze them qualitatively and quantitatively. For the separation, a mobile and stationary phase are necessary. The mobile phase is passed through the column. The inner surface of the column is coated or bonded with the stationary phase. The time, the component needs to pass the column (retention time), depends on the strength of the interaction forces between the stationary phase and every molecule. The components with weak interactions leave the column and reach the detector the fastest, while those with the strongest bonds elute at the end.[13]

The interaction forces, which act between the stationary phase and the molecules of the sample, are intermolecular forces. They are classified in dispersion forces, polar forces and ionic forces. Dispersion forces are the result of charge fluctuations, which emerge from fluctuations of the nuclei and the electrons. The strength of the dispersion force depends mainly on the polarizability of the molecule. Polar forces arise from dipole-dipole or dipole-induced-dipole interactions. Permanent or induced dipoles lead to localized charges, as a result polar forces emerge between these charges. Ionic forces are resulting from ions which are oppositely charged and interact with each other.[13]

3.1.2 Gas Chromatograph (GC)

Chromatography is classified by the type of the mobile phase (carrier gas) in gas chromatography and liquid chromatography. For this thesis a gas chromatograph (GC) with a thermal conductivity detector is used and therefore will be explained in more detail below.

A GC basically consists of an injector, a column, a column oven, a carrier gas, a detector and a data system. The temperature of the sample is regulated by using a heated manifold. The sample is injected into the column by an injector. The sample is split up according to the different interactions between the sample, the carrier gas and the column substrate. The separated gas is analyzed by a detector. There are various kinds of detectors including thermal conductivity (TCD), flame ionization (FID) and nitrogen–phosphorus detectors (NPD).[14]

Thermal Conductivity Detector (TCD)

The operating principle of the TCD is based on a Wheatstone bridge with four filaments and two channels – one channel for the eluate with the carrier gas and another one for the pure

carrier gas. Each gas is passed through two different filaments of the Wheatstone bridge. Due to the different gas compositions, the thermal conductivity of the filaments differs. Therefore, also the temperature of the filament varies. This leads to a change of the resistance, which can be used as signal. The detection limit of a TCD is determined by the difference between the thermal conductivities of the analytes and the carrier gas. Typically, helium is used as carrier gas, since it has a higher thermal conductivity than other gases. An advantage of a TCD is that it is a universal detector, hence it can detect every compound that can be analyzed using a GC. Additionally, the TCD is non-destructive, allowing further analysis of the gas.[15]

The most important specification factors of a detector are its sensitivity, the noise and the dynamic and linear dynamic range. The detection limit gives the lowest concentration, which can be detected. The detector noise arises from fluctuations of the baseline which do not emerge from the detected substances. The dynamic range comprises the range between the lowest and highest detectable concentration, where the signal of the detector doesn't change anymore. The linear dynamic range gives the range where signal intensity shows linear dependence on the concentration.[13]

3.1.3 Columns

According to the expected predominant interaction force the stationary phase, which coats the inner surface of the column, is selected. If there should be a separation according to the dispersive interactions a non-polar stationary phase is used. Other stationary phases separate substances with different polarity on basis of their polar forces. Ionic materials cannot be analyzed by a GC, since they are not volatile under the prevailing conditions.[13]

Depending on the type of column, one distinguishes between capillary and packed-column GC. However, in the last years, capillary columns are used almost exclusively. The separation, and therefore the resolution of capillary columns is higher. Further benefits are a faster analysis, smaller required sample size, and a higher sensitivity compared to packed columns. Today, capillary columns are made of fused-silica.[16]

Capillary columns can be divided into porous-layer open tubular (PLOT) columns and wall-coated open tubular (WCOT) columns. The stationary phase of PLOT columns is a solid (e.g. Al_2O_3, zeolites), whereas for WCOT columns a liquid or a gum such as polysiloxane is used.[17]

For the analysis of gaseous samples in this thesis two PLOT columns are applied. One column separates the components of the gas according to their polarity. The other one uses a molecular

sieve. The molecular sieves consist of a porous material, such as aluminum silicate. The separation is due to the different size of the molecules. Small molecules enter the pores, resulting in a longer travel distance and therefore longer retention time, while bigger molecules pass the pores.[14, 15]

3.2 Fourier Transformation Infrared Spectroscopy

Fourier transformation infrared spectroscopy (FTIR) is a type of IR spectroscopy based on irradiation of a sample with a polychromatic IR radiation source. Spectra are recorded using a Michelson-interferometer. A basic scheme of an interferometer is displayed in *Figure 3.1*. The radiation of the source is directed to a beamsplitter, the two resulting beams are directed onto a fixed mirror and a variable mirror, respectively. The rays are reflected at the mirrors and interfere at the beamsplitter. In the case that the mirrors do not have the same distance from the beamsplitter destructive interference occurs. However, if they reach the same distance, constructive interference arises, what is called center-burst. The recombined beam interacts with the sample and the transmitted part of the light reaches the detector.[18]

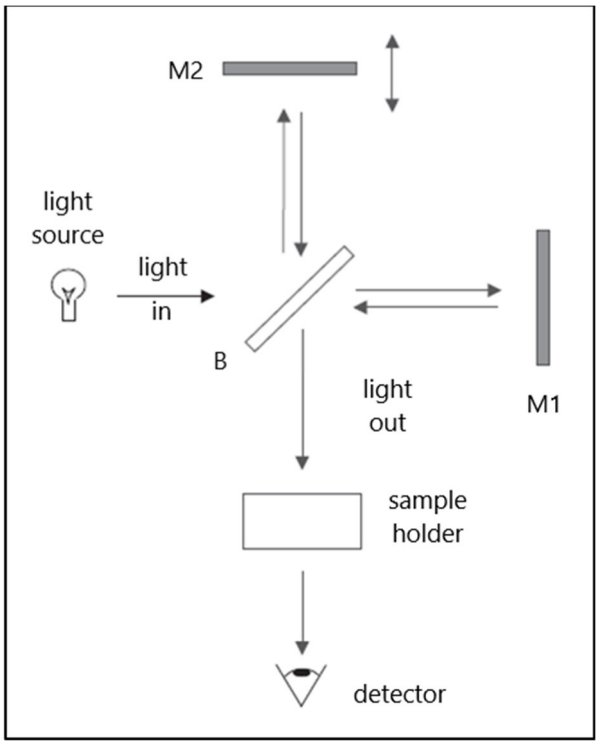

Figure 3.1: Basic scheme of an interferometer[18]

The position of the variable mirror is determined by a helium-neon laser. This is important, since the exact position has to be known in order to average the center-bursts of several measurements, and to calculate the spectrum via the Fourier transformation. The light of the

helium-neon laser passes the same way as the light of the source. From the interference pattern of the laser light, the position of the variable mirror can be determined.[18]

The resulting interferograms are Fourier transformed, to obtain the IR spectra. These spectra are typically plotted as transmission (signal intensity) versus wavenumber, allowing the qualitative and quantitative analysis of functional groups via their characteristic vibrations. Vibrations are only excited if the molecule has a dipole moment and the dipole moment changes. For example, HCl and H_2O are IR-active, while linear molecules such as H_2 are IR-inactive.[18]

3.3 Scanning Electron Microscopy

3.3.1 Interactions

Scanning Electron Microscopy (SEM) coupled with Energy Dispersive X-ray Spectroscopy (EDX) is based on the interaction of electrons with atoms of the sample, allowing small-scale imaging and obtaining elemental information. A primary electron beam scans the surface of the sample and interacts with the atoms of the sample. Various signals are generated including secondary electrons (SE), backscattered electrons (BSE), Auger electrons and characteristic X-rays, which can be used to create an image, diffraction pattern or elemental spectrum.[19]

The interaction of the primary electron beam with the sample leads to elastic and inelastic interactions. Elastic interactions are caused by Coulombic attraction of the atomic nucleus, leading to a change of the trajectory of the electron, without energy loss. The velocity almost keeps the same, resulting in an unchanged kinetic energy. The probability of an interaction between the primary electron beam and the atom is inversely proportional to the square of the primary beam energy (E^2) and proportional to the square of the atomic number (Z^2).[19]

Inelastic scattering leads to an energy loss of the electron, while the path of the electron changes less than 0.1°. The primary electrons release part of their kinetic energy to the atoms of the sample.[19]

Secondary electrons and X-rays result from inelastic scattering. BSE are primary electrons that are deflected by elastic scattering.[19]

The ratio of the number of BSE and the number of primary electrons gives the BSE coefficient η. The parameter η increases with the atomic number (Z) as shown in *Figure 3.2* (left). Due to this dependence a material contrast (compositional contrast, atomic number

contrast)[20] of the sample can be obtained by BSE analysis. Areas with higher Z, and therefore a higher amount of BSE, appear brighter.[19]

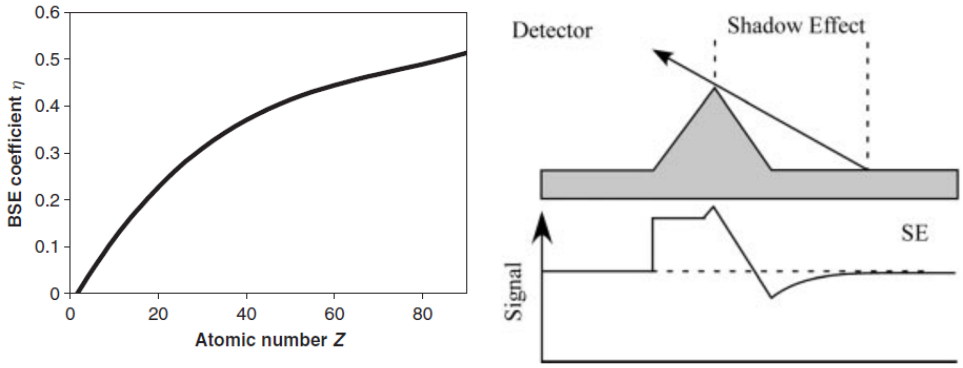

Figure 3.2: *Left: the BSE coefficient (η) versus atomic number Z – η rises with higher Z* [19]*; right: shadow effect of SE detection*[21]

In contrast to the BSE, SE are relatively insensitive to the atomic number of the sample. Because secondary electrons have only small energies, they can escape from a depth of a few nanometers of the surface.[19] Therefore, secondary electrons are surface-sensitive. From secondary electrons topographical information can be obtained, primarily due to the shadowing effect (*Figure 3.2*, right) and the higher generation of secondary electrons at edges and surface perturbations. These effects depend on the angle of the primary electron beam and the detector to the sample.[21]

Further, characteristic X-rays can be detected in SEM experiments. The high energetic electrons of the primary beam lead to ionization. Electrons of inner shells are ejected, and the empty places are refilled by electrons from outer shells with higher energy, resulting in the emission of characteristic X-ray radiation (*Figure 3.3*). Characteristic X-rays can be used to deduce the elemental composition of materials.[19]

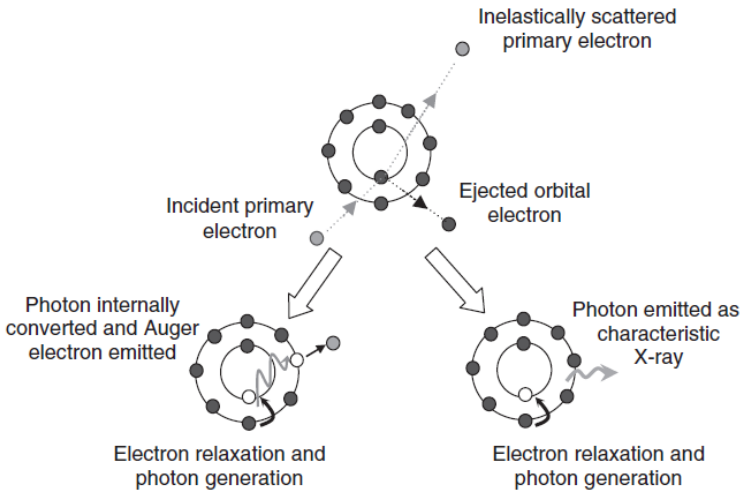

Figure 3.3: *Production of X-rays and Auger electrons*[19]

A schematic interaction volume of a primary electron beam is shown in *Figure 3.4*. Secondary electrons can only escape from about 5 - 50 nm of the sample surface, since they have low energies (< 50 eV). The high energetic BSE (> 50 eV) originate from deeper regions.[19]

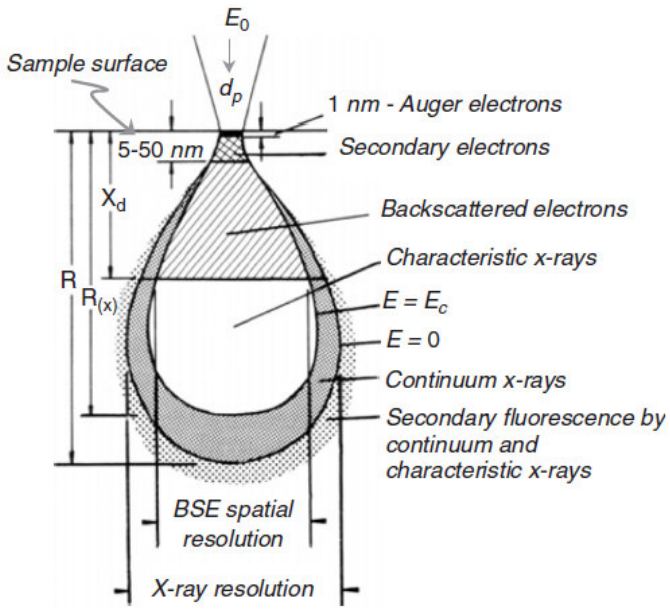

Figure 3.4: *Schematic image of the interaction volume*[19]

The interaction volume of the primary beam can be influenced by the beam energy and the chemical composition of the sample (see *Equation 1*).

$$R = 0.0276 \frac{A \cdot E_0^{1,67}}{Z^{0.89} \cdot \rho} \qquad (1)$$

In the equation Z is the atomic number, A the atomic weight, ρ the density in g/cm³ and E_0 the electron energy in keV.[19]

Monte Carlo simulations are performed using the software Casino, to visualize the influence of the beam energy on the interaction volume[21] (For more information on Monte Carlo simulations and the software Casino see *Chapter 3.3.4*). In *Figure 3.5*, the results of Monte Carlo simulations of manganese (Mn Z = 25) with a beam energy of 10 keV, 15 keV and 20 keV are compared. With a higher beam energy, the interaction volume gets bigger - the radial distribution and the depth increase.

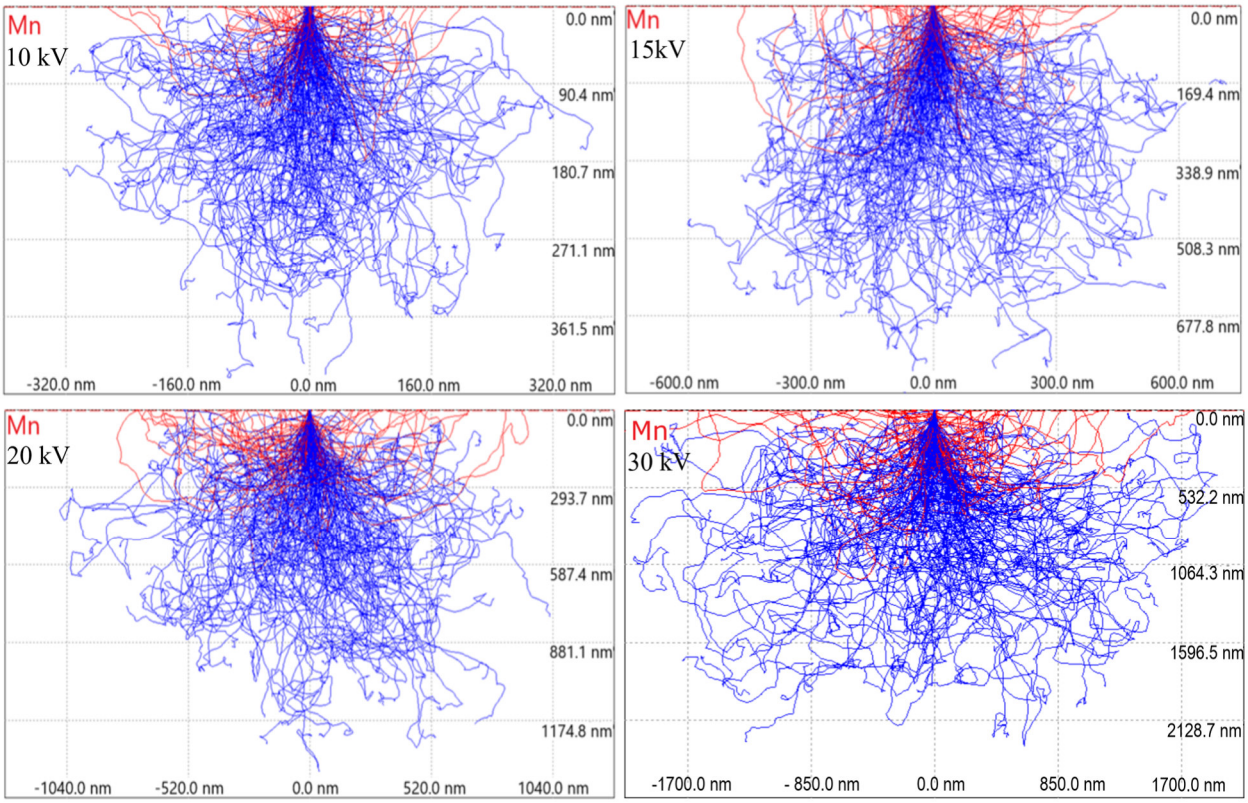

Figure 3.5: *Simulations of the electron trajectories of a substrate of Mn at different beam energies (10 keV, 15 keV, 20 keV and 30 keV); number of electrons to simulate = 2000; tilt of the specimen = 0°; beam radius = 10 nm (Casino)*[22]

As can be seen in *Equation (*1), the interaction volume also depends on the chemical composition. The atomic number is inversely correlated to the size of the interaction volume. In *Figure 3.6* simulations of the electron trajectories of substrates of C (Z = 6), Mn (Z = 25), Ag (Z = 47) and Au (Z = 79) are compared: an increase in the atomic number (Z) leads to a decrease of the size of the interaction volume.

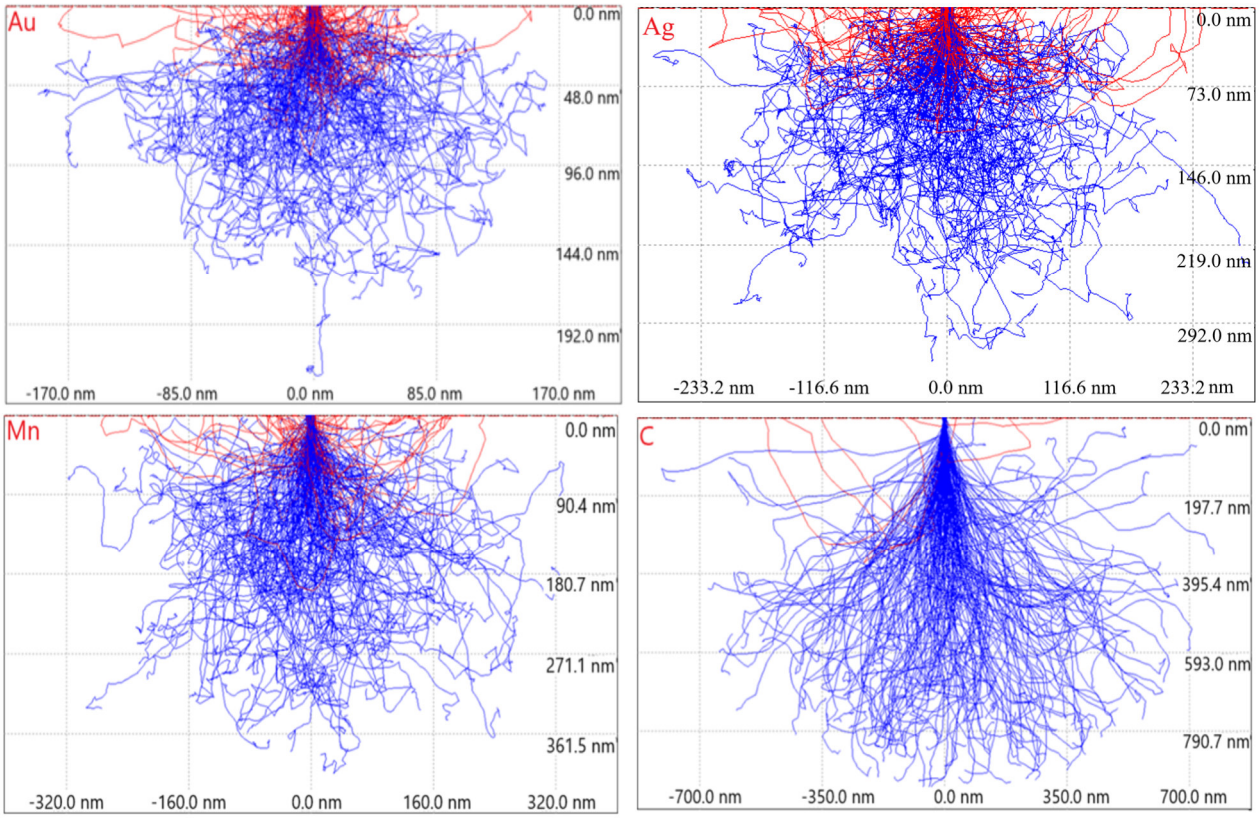

Figure 3.6: *Simulations of the electron trajectories of substrates of C (Z = 6), Mn (Z = 25), Ag (Z = 47), Au (Z = 79); beam energy=10 keV; number of electrons to simulate = 2000; tilt of the specimen= 0°; beam radius =10 nm (Casino)*[22]

3.3.2 Components of an SEM

3.3.2.1 Generation of the Electron Beam

In *Figure 3.7* a schematic of an SEM is shown. The electron beam is formed using an electron source. The filament provides electrons which are accelerated to the anode. The Wehnelt cap, which has a negative bias, focuses the electrons. The filament can be a thermionic emitter or a field emission source. A thermionic emitter releases electrons by overcoming their work function by resistively heating. Typically, a tungsten v-shaped 'hairpin' or a lanthanum hexaboride (LaB_6) single crystal are used for this kind of filament. In case of field emission sources electrons tunnel to the fine, sharp single crystal tungsten tip without thermic energy by applying a very high electrical field.[19]

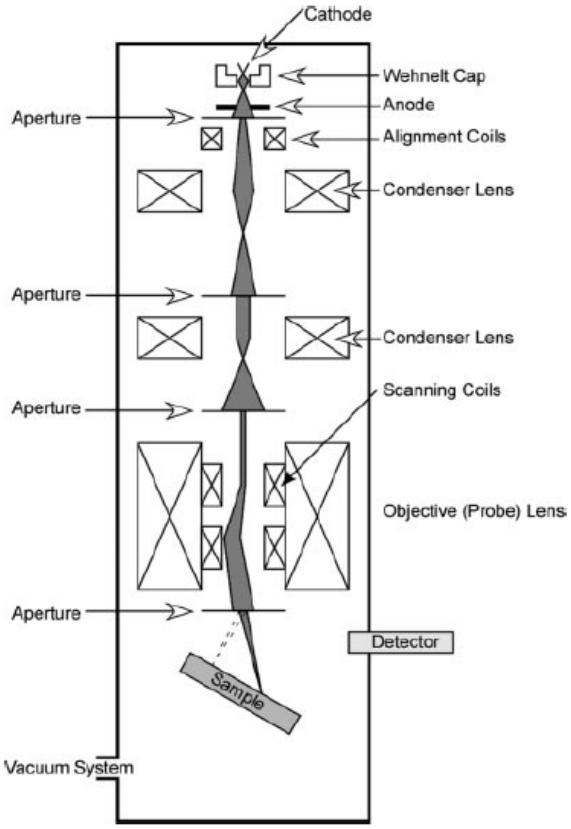

Figure 3.7: *Scheme of an SEM* [21]

3.3.2.2 Lenses

The condenser lens and the objective lens are focusing the electron beam onto the specimen. Since they are electromagnetic lenses, a change of the current in the lenses leads to a variation of the field strength, resulting in a change of the trajectory of the electrons and the crossover point of the beam.[19]

Electromagnetic lenses exhibit lens aberrations, which are limiting the resolution. Examples include spherical aberration, chromatic aberration, aperture diffraction and astigmatism. Spherical aberration is the result of different deflections of the electrons depending on the position, where the electron reaches the lens. Electrons at the outside of the lens are deflected stronger than electrons in the middle of the lens. Chromatic aberration leads to different focal planes of the electrons, because of the spread in electron energy. The diffraction of the electrons with higher energy is higher than of electrons with lower energy. Aperture diffraction depends on the size of the aperture. The smaller the aperture, the more electrons are diffracted and the larger is the beam diameter. Astigmatism results from asymmetries of the lens or contaminations. Two focal lengths in perpendicular directions arise, leading to a broader beam.[19]

3.3.2.3 Detectors

To detect SE typically an Everhart-Thornley detector is used. The detector consists of a szintillator which is surrounded by a metal grid, a light guide and a photomultiplier. The electrons are collected and create photons. The photons are transferred via a light guide to the photomultiplier. Electrons are ejected and accelerated to a positively charged dynode, where further electrons emerge. These electrons are accelerated to further dynodes, resulting in a multiplication of electrons and therefore, an amplified signal.[21]

BSE can be analyzed by a solid-state detector. If a BSE hits the active area of the detector, consisting of a semiconducting material, an electron-hole pair is generated. In the electric field, the electron and the hole are separated and a current pulse is generated.[21]

An energy dispersive X-ray spectrometer (EDX) can be used to detect X-rays. It is based on a solid-state detector. Either a Si(Li) detectors or a silicon drift detectors (SDD) are used. The EDX detector is sheltered by a window, to prevent contaminations. Typically, elements with an atomic mass (Z) of 5 (boron) or higher can be detected. However, the detection of elements with a low X-ray energy is often imprecise, since the correlated X-rays are partly absorbed by the detector.[21]

To quantify the elemental composition of a sample, the signal intensity cannot only be related to a reference, since a matrix correction has to be done. Several effects occur, which must be considered. These effects are summarized by the ZAF coefficient (atomic number effect (Z), absorption (A) and fluorescence (F)). [21]

The concentration of the sample can be calculated by using *Equation 2*.

$$c = ZAF \cdot c_{ref} \cdot \frac{I}{I_{ref}} \qquad (2)$$

In *Equation 2* the concentration of the sample is c, the concentration of the reference is c_{ref}, the signal intensity of the sample is I and the signal intensity of the reference is I_{ref}.[21]

3.3.3 Software for the Simulation of Electron Trajectories and for SEM image analysis

Monte Carlo Simulations – Casino and NIST DTSA-II

Monte Carlo simulations can be performed to assess the trajectories of electrons. For Monte Carlo simulations an incremental simulation is applied. Various simplifications are used, since the scattering behavior of electrons cannot be described adequately by algebraic expressions. In this thesis the Monte Carlo simulation software Casino[22] and NIST DTSA-II[23] are used. Casino is the appropriate software for simulations of electron trajectories in bulks and thin films.

Besides other functions, the software NIST DTSA-II enables the simulation of trajectories of electrons through samples with different structures. Among others, spherical and cubic particles on a bulk substrate can be simulated. Additionally, it is possible to quantify measured spectra. *Figure 3.8* shows the graphical user interface of NIST DTSA-II.

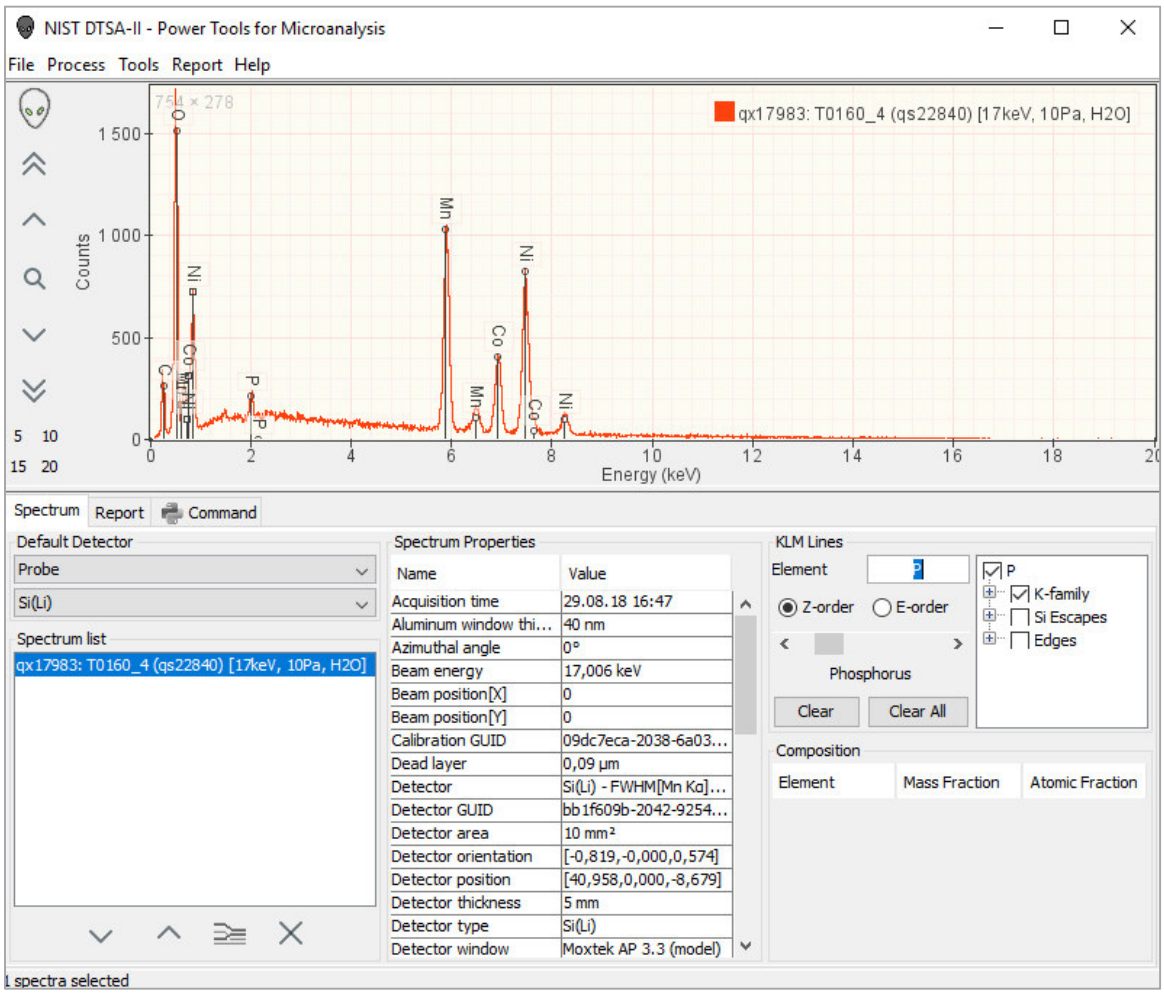

Figure 3.8: *Graphical user interface of NIST DTSA-II*

Fiji

A popular software for SEM image analysis is the open source program ImageJ. The software Fiji (acronym for "Fiji is just ImageJ") bases on ImageJ, but it is more user-friendly, since it is easy to install and bundles many plugins. The graphical user interface of Fiji is shown in *Figure 3.9*. Fiji can be used for creating a binary image by choosing a grey level threshold and obtaining e.g. the size distribution of the particles in an SEM micrograph.

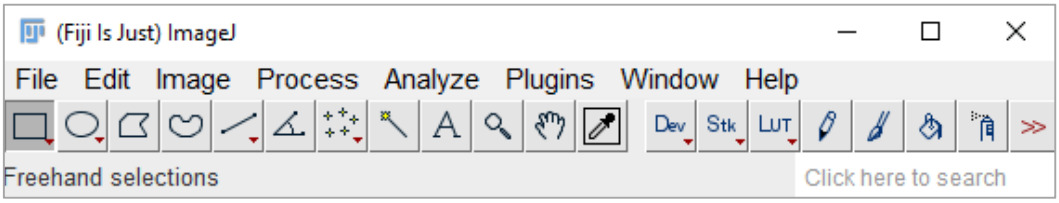

Figure 3.9: *Graphical user interface of Fiji*

3.3.4 Variable Pressure – Environmental Scanning Electron Microscopy (VP-ESEM)

VP-ESEM allows to examine an electrically non-conducting sample without applying a conductive coating on the surface. If an isolating sample is analyzed in the high vacuum (HV) mode the sample gets charged. This can be minimized or prevented with the variable pressure (VP) mode, where the specimen chamber is filled with imaging gases like water vapor or nitrogen with a pressure below about 200 Pa. The BSE and SE can undergo inelastic scattering with the gas molecules close to the surface, leading to ionized gas molecules and a production of further electrons. This multiplication of the electrons leads to the amplification of the SE signal (*Figure 3.10*). Additionally, the positive ions of the ionized gas molecules are attracted by the charged surface, resulting in a local dynamic charge neutralization.[19, 22]

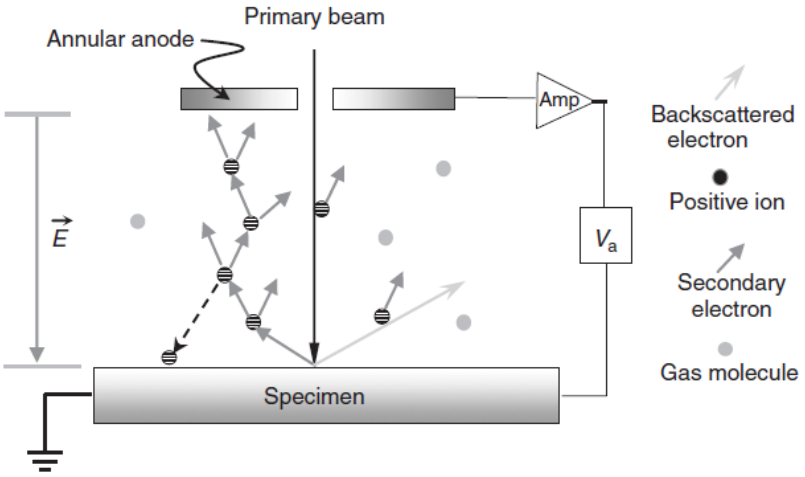

Figure 3.10: *Schematic image of the ionization of gas molecules leading to an amplified signal and neutralization of the specimen*[19]

A negative effect of the VP mode is that the beam electrons may scatter elastically with gas molecules. This effect is called skirt effect. The EDX quantification using the VP mode is more imprecise than with the HV mode because of the skirt effect. The radius of the skirt within the low-pressure mode can be minimized by lowering the pressure. An estimated skirt radius (Rs) gives *Equation 3*.[19]

$$R_S = \left(\frac{0.364 \cdot Z}{E}\right)\left(\frac{P}{T}\right)^{1/2} L^{3/2} \qquad (3)$$

In *Equation 3*, corresponds *Z* to the atomic number of the gas, *E* to the beam energy in keV, *p* to the pressure in Pa, *T* to the temperature in K and *L* to the path length in gas in m.[19]

To show the influence of the pressure in the VP mode and to compare the VP and HV mode, simulations were performed. A spherical Mn_2O_3 particle with a diameter of 1.0 µm on a carbon bulk substrate in HV and VP mode were simulated using NIST DTSA-II[23]. A beam energy of 10 keV was used. To quantify the spectra, carbon, manganese and oxygen are simulated as a bulk material and used as a standard.

Figure 3.11 displays the simulated spectrum and the quantification in the HV mode (the listed decimal points are results of the program and do not correlate to the accuracy of the method EDX). In the HV mode almost entirely the Mn_2O_3 particle is detected, only 3.32 wt% of carbon is quantified. In contrast, by changing to the VP mode a significant carbon peak appears. *Figure 3.12* presents the spectrum and the quantification of the VP with nitrogen and a pressure of 10 Pa. Using these conditions, the carbon fraction makes up 28.91 wt%. By increasing the pressure to 50 Pa the carbon fraction rises strongly to 66.51 wt% (*Figure 3.13).* This is reasoned by the skirt effect. The neighboring area contributes to the resulting signal, and consequently no accurate X-ray microanalysis can be performed.

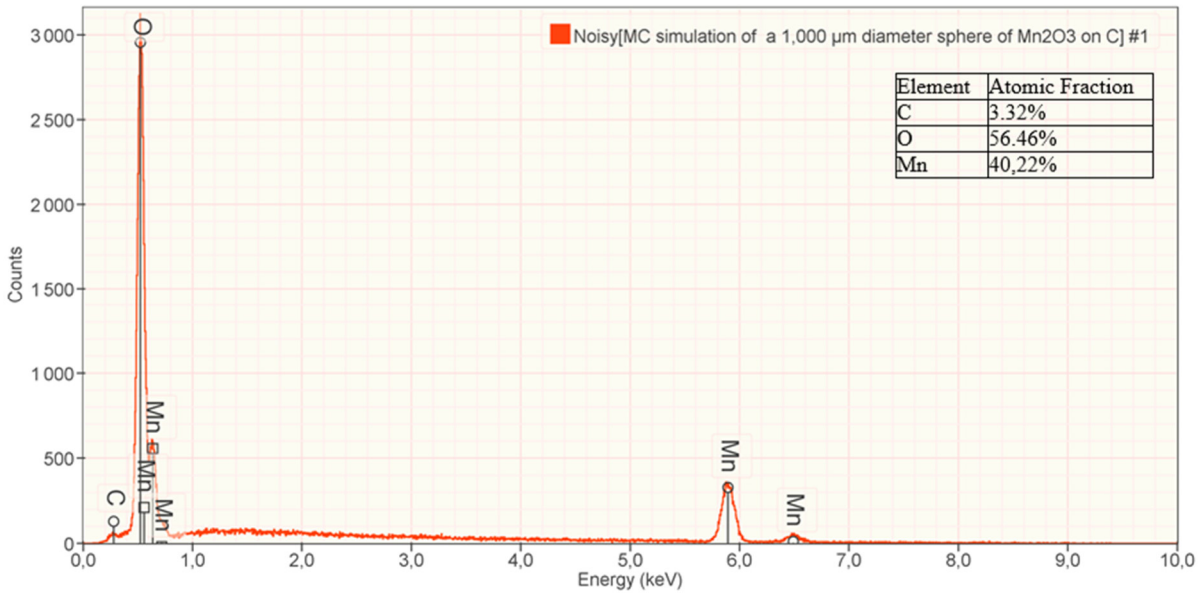

Figure 3.11: *Simulated spectrum and quantification of a 1.0 µm diameter sphere of Mn_2O_3 on C substrate; HV mode; beam energy =10 keV (NIST DTSA-II)*[23]

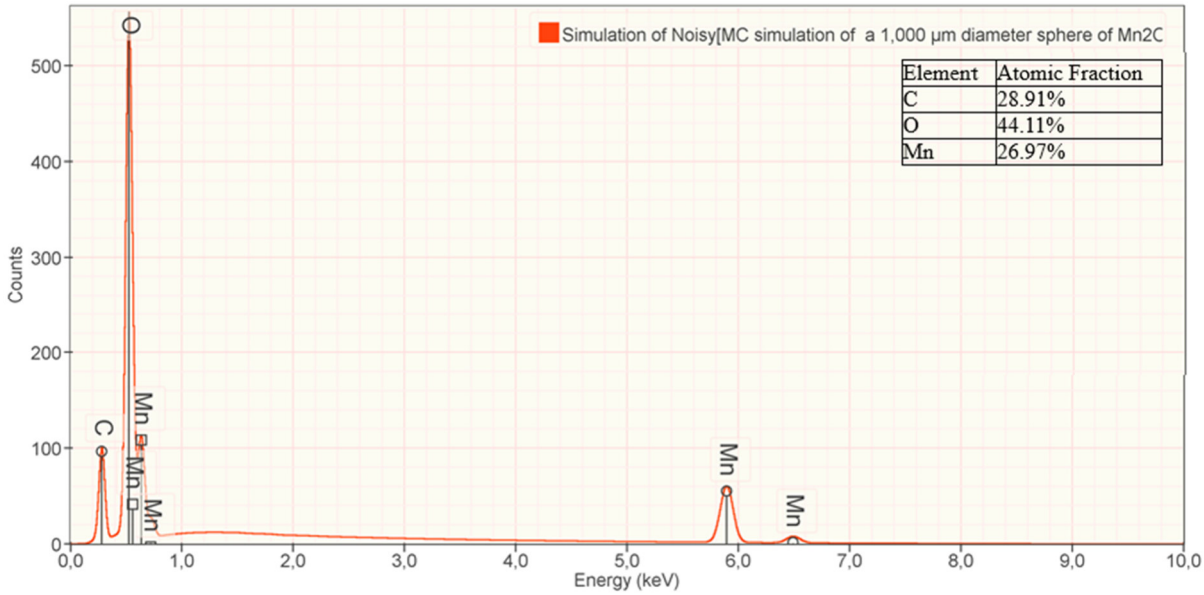

Figure 3.12: *Simulated spectrum and quantification of a 1.0 µm diameter sphere of Mn_2O_3 on C substrate; VP mode: nitrogen, 10 Pa; beam energy =10 keV (NIST DTSA-II)*[23]

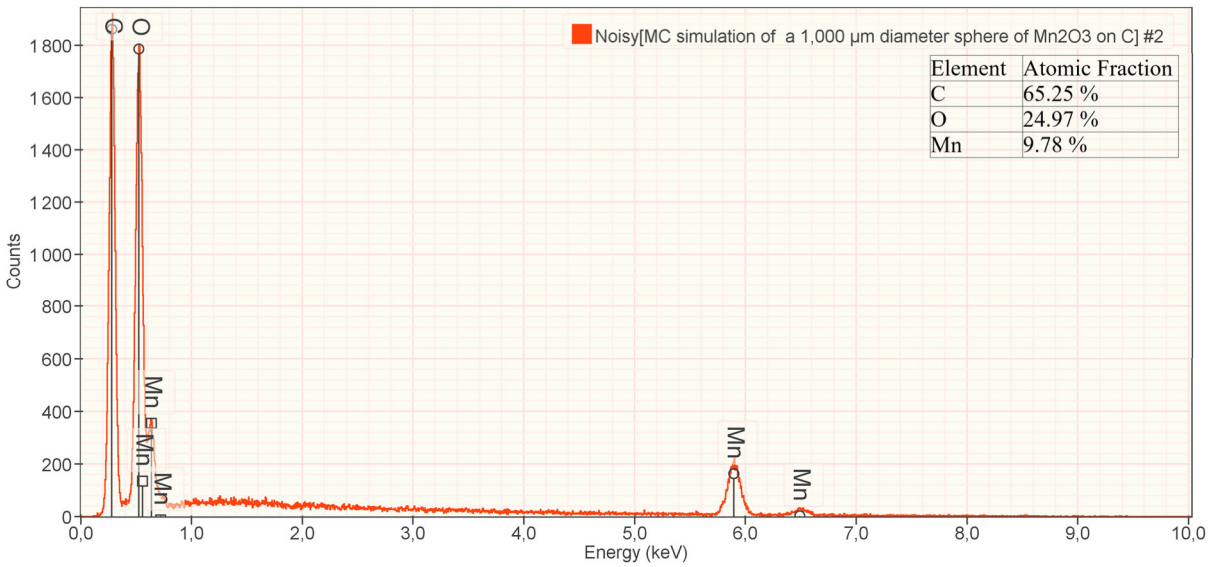

Figure 3.13: *Simulated spectrum and quantification of a 1.0 µm diameter sphere of Mn_2O_3 on C substrate; VP mode: nitrogen, 50 Pa; beam energy =10 keV (NIST DTSA-II)*[23]

3.3.5 Particle Analysis using SEM/EDX

An SEM equipped with an EDX detector can be used for the analysis of elemental composition and size distribution of microscopic particles. However, various effects have to be taken into account. If the particle is smaller than the interaction volume, the beam electrons can penetrate through the side and the bottom of the particle. As a result, the beam electrons can reach the substrate, where the particles are applied to. *Figure 3.14* compares simulations of spherical Mn_2O_3 particles with different diameters (0.2 µm, 0.5 µm, 1.0 µm and 1.5 µm) on a carbon substrate using NIST DTSA-II. In *Table 3.1* the simulated spectra of *Figure 3.14* are quantified. For the simulations the HV mode and a beam energy of 10 keV are used.

With smaller particle size, the C peak increases compared to the Mn and O peak. A Mn_2O_3 particle with a diameter of 0.2 µm on carbon substrate consists of approximately 65 atomic percent (at%) carbon. With bigger diameter the atomic fraction of the carbon gets dramatically smaller. A Mn_2O_3 particle with a diameter of 0.5 µm on a carbon substrate consists of about 8.5 at% carbon, a particle with a diameter of 1.0 µm 3.3 at% carbon and a particle with a diameter of 1.5 µm 1.5 at% carbon.

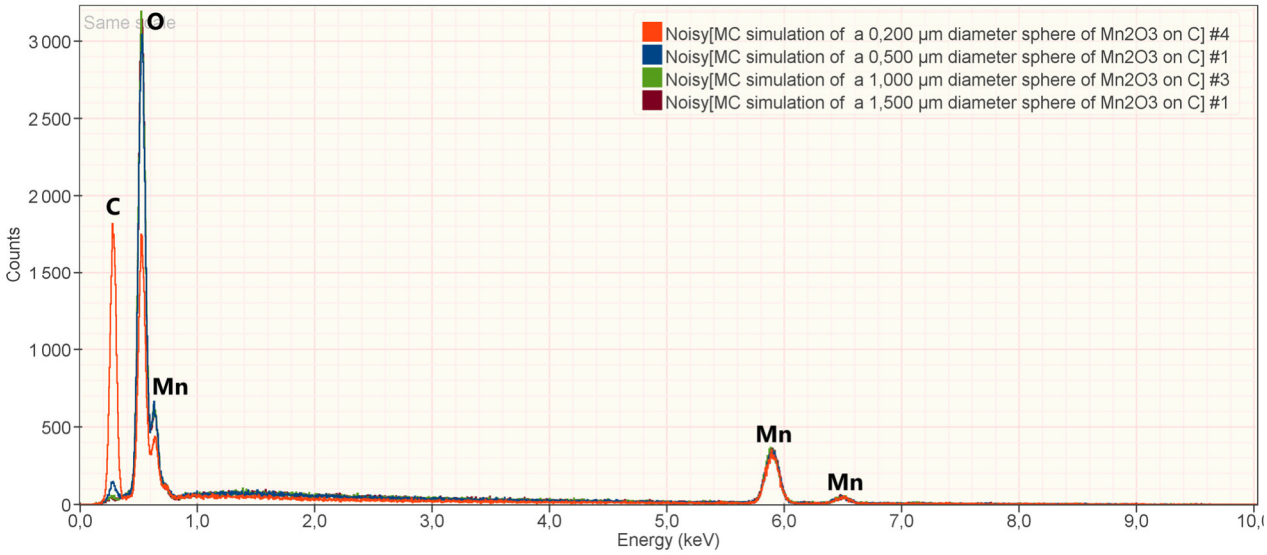

Figure 3.14: *Simulated spectrum of a 0.2 µm, 0.5 µm, 1.0 µm and 1.5 µm diameter sphere of Mn_2O_3 on C substrate; HV mode; beam energy = 10 keV (NIST DTSA-II)*[23]

Table 3.1: *Quantification of the simulated spectrum of a 0.2 µm, 0.5 µm, 1.0 µm and 1.5 µm diameter sphere of Mn_2O_3 on C substrate; HV mode; beam energy =10 keV*

Diameter of particle	**0.2 µm**	**0.5 µm**	**1.0 µm**	**1.5 µm**
C [at%]	64.56	8.44	2.24	1.49
O [at%]	22.00	53.26	57.27	57.48
Mn [at%]	13.44	38.31	40.50	41.03

When analyzing particles two particle geometry effects (particle mass effect and particle absorption effect) have to be considered additionally. The particle mass effect originates from the beam electrons, which are penetrating through the side and the bottom of the particle and therefore producing less X-rays than flat bulk samples. The second effect is the particle absorption effect. The surface curvature of the particle leads to a lower absorption path in a particle compared to a flat bulk sample. The X-ray absorption depends exponentially on the absorption path. Both effects are schematically shown in *Figure 3.15*.[22]

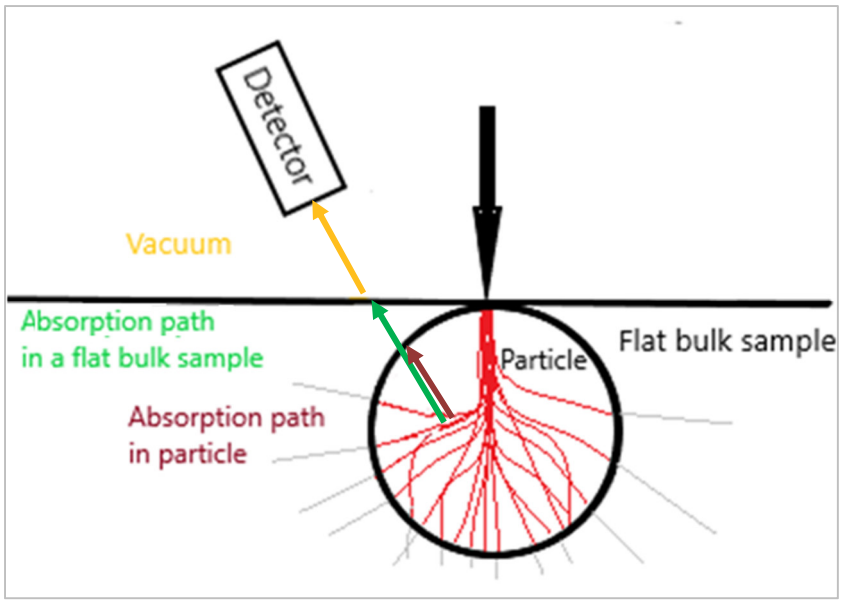

Figure 3.15: *Schematic image of the particle geometry effects; particle mass effect: lower X-ray production because of beam electrons penetrating through the side and the bottom of the particle (grey lines); particle absorption effect: absorption path of particle (red arrow) is smaller than absorption path of flat bulk surface (green arrow)*

3.3.6 Sampling and Sample Preparation of Particles for SEM/EDX Analysis

To analyze particles with an SEM/EDX the particles have to be transferred evenly onto a sample carrier. Therefore, it is essential to collect a representative sample. The most accurate approach for samples, which cannot be analyzed as a whole, is to document the collected parts properly.[24]

After sampling the particles, they have to be applied to a substrate. This substrate should not contain the elements of interest, since the electrons may penetrate through the side and the bottom of the particle into the substrate. A good choice for a substrate is a carbon tape. However, a blank spectrum has to be measured, since it can contain additional elements such as oxygen. Other possible substrates are silicon and aluminum.[25]

The particles should be well separated, to avoid that electrons scatter off to their neighboring particles. The particles can be sprinkled or blown onto an adhesive tape. The particles must stick properly, since loosely bounded particles can fly off easily under vacuum and contaminate the specimen chamber of the SEM. Various methods of sample preparation are discussed in literature. In the following paragraphs some methods are described.[24, 26]

According to the OECD guideline for particle size distribution, a suitable method is mixing the particles with a deionized water, drying them on a membrane filter and mounting the dried filter on the SEM sample holder using an adhesive copper tape. Additionally, other sources

recommend that a suspension of particles and alcohol such as methanol or acetone should be made. Another method of the OECD guideline is to cover an adhesive copper tape by using a pipette or an atomizer. Further a spatula can be used to sprinkle the adhesive tape with the powder.[26, 25, 27]

After depositing particles on a substrate, the loosely bounded particles, which do not stick to the tape, should be removed. To do this, first the SEM sample holder is gently tapped followed by a jet of air. Also, a thin (< 10 nm) carbon coating can be applied to better attach the particles and to make them conductive.[25, 24]

4. Experiments

4.1 Analyzed Battery Cells

In this thesis, the released gases and particles after thermal runaway of four Li-ion cells of the same type were analyzed. The cells are pouch cells with the same chemical composition and a capacity of 45 Ah and a voltage of 3.8 V.

An analyzation of the cells is provided by the Vehicle Safety Institute at Graz University of Technology: The cathode consists of nickel-manganese-cobalt-oxide and manganese-oxide, with particle sizes of about 12 µm (see *Figure 4.1*). The anode consists of graphite and the collectors are made of aluminum and copper.

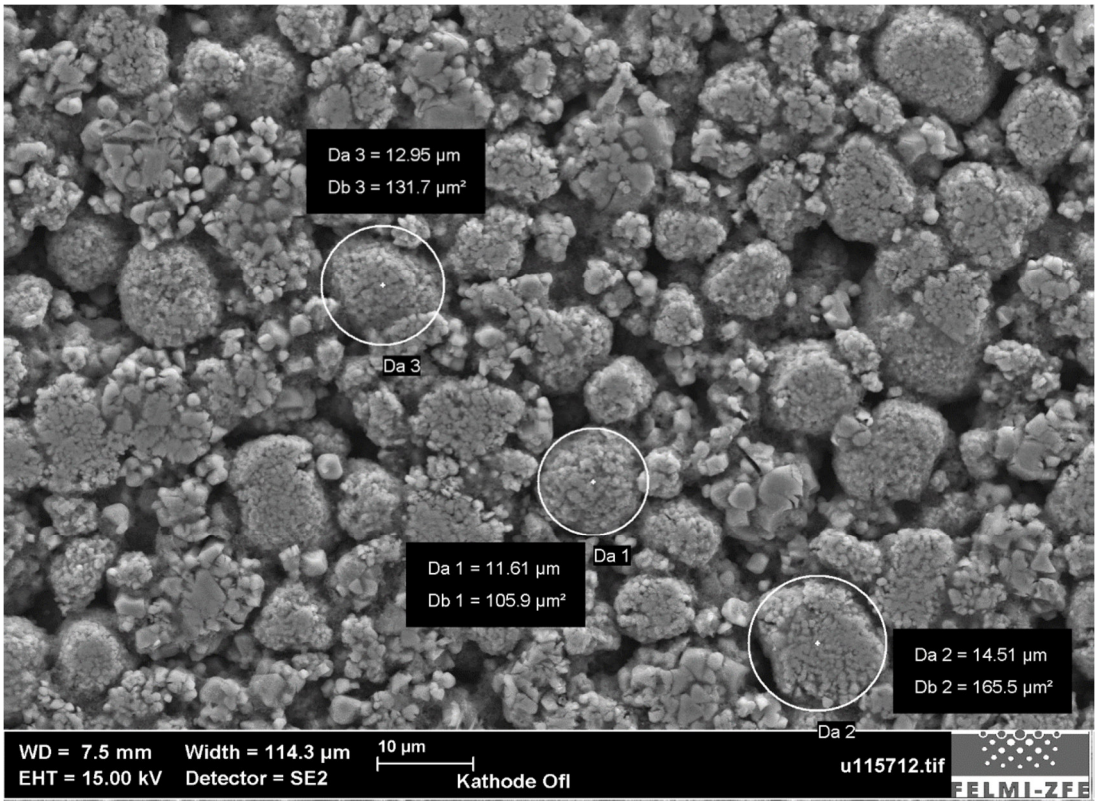

Figure 4.1: *SE image of the cathode (provided by the Vehicle Safety Institute at Graz University of Technology)*

4.2. Thermal Runaway Experiments

The thermal runaway experiments were carried out in a reactor filled with inert gas (N_2). The open and closed reactor is shown in *Figure 4.2*.

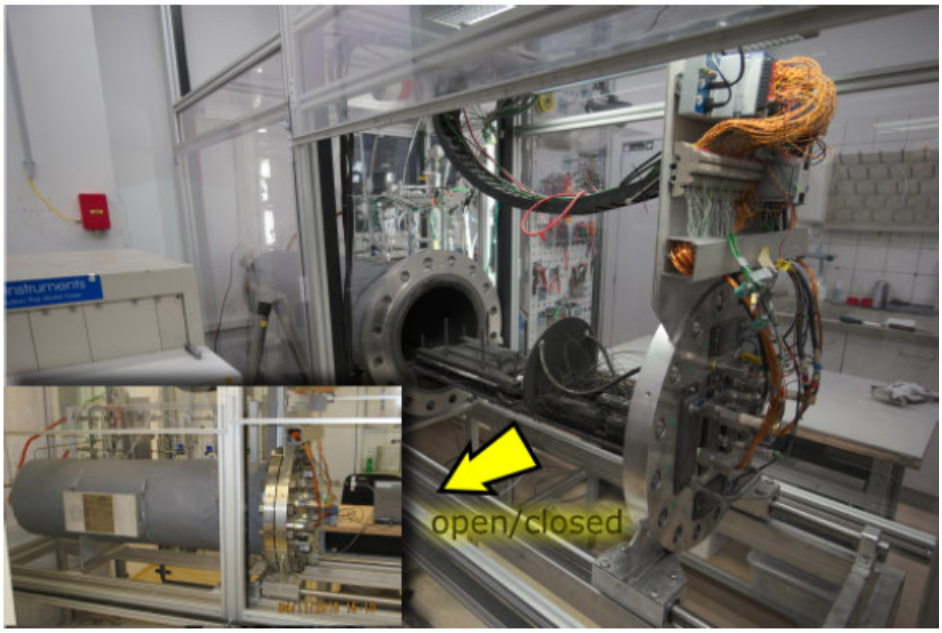

Figure 4.2: *Open and closed reactor, where the thermal runaway experiment takes place*

For the experiment, the cell is placed in the cell holder inside the reactor. The cell is surrounded by mica plates, which are thermally isolating. Through these mica plates a total of 24 thermocouples are connected to the outer surface of the pouch cell, to measure its temperature. The pouch cell with the mica plates and thermocouples is placed firmly between two pressure plates (*Figure 4.3*).

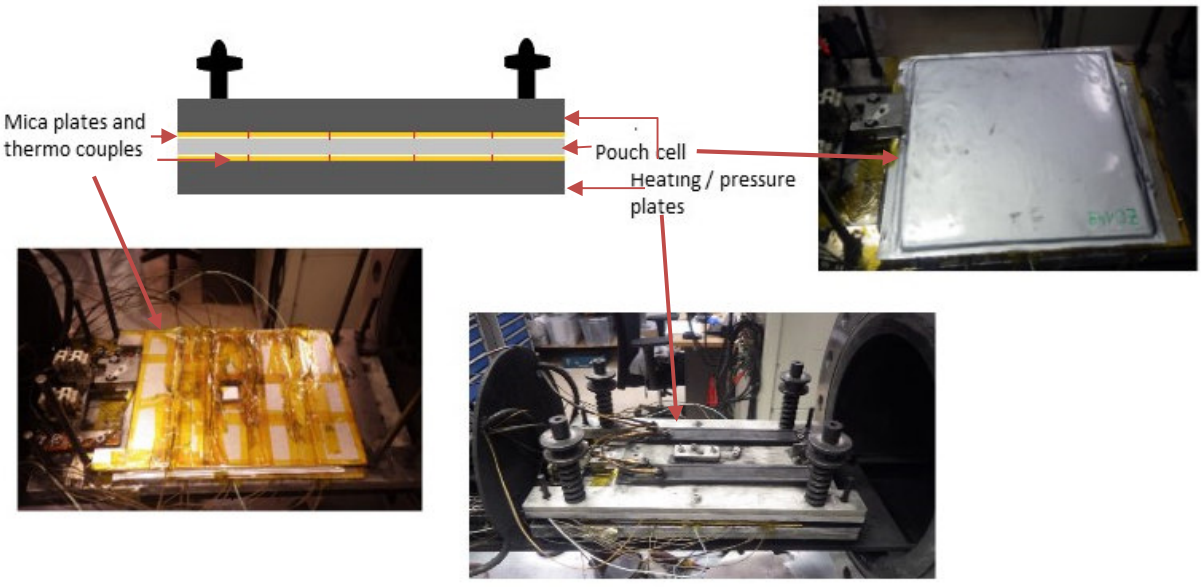

Figure 4.3: *Experimental setup of TR experiments: configuration of the cell within the cell holder*

After evacuating the reactor, it is filled with nitrogen until ambient pressure is reached. This inert gas leads to a non-flammable atmosphere within the reactor. A reference measurement of the gas atmosphere in the reactor is done using the GC. Once the reactor is hermetically sealed, the cell is repeatedly charged and discharged at normal conditions. Then, the thermal runaway experiment was started. In general, thermal runaway can be induced by various methods (e.g. overloading, heating or pressurizing the cell).

In experiment 1, it was tried to overload the battery. However, this method did not lead to thermal runaway. Therefore, the whole battery was heated with the heating plates until a thermal runaway occurred. In experiment 2 and 3 the battery was heated at one position in the middle of the pouch cell. In experiment 4, the cell was set under pressure and charged and discharged repetitively.

4.3 Gas Analysis

After a thermal runaway occurred, the gas within the reactor is transferred to a Fourier transformation infrared spectrometer (FTIR, Bruker MATRIX MG01) and a gas chromatograph (GC, Agilent 3000 Micro). The gas connection to the FTIR is heated to 140°C, therefore only the substances with condensation temperatures below 140°C will stay in gas phase and will be detected. Before the gas is transferred in the GC, it has to be washed in water wash bottles, since the columns of the GC are corrosion sensitive. The FTIR can determine small amounts of gases. Components of the released gas including hydrogen fluoride (HF), methane, carbon monoxide, carbon dioxide, water and the electrolytes DEC, DMC, EC and EMC can be quantified. However, an FTIR cannot determine molecules, such as nitrogen and oxygen. Therefore, additionally a GC is used. The GC is equipped with a thermal conductivity detector (TCD) and two columns (MolSieve 5A PLOT column and a PLOT U column). On the MolSieve 5A PLOT column the concentration of nitrogen, oxygen, hydrogen, carbon monoxide and methane in the vent gas are determined, whereas the PLOT U column is used to quantify carbon dioxide, acetylene, ethylene and ethane.

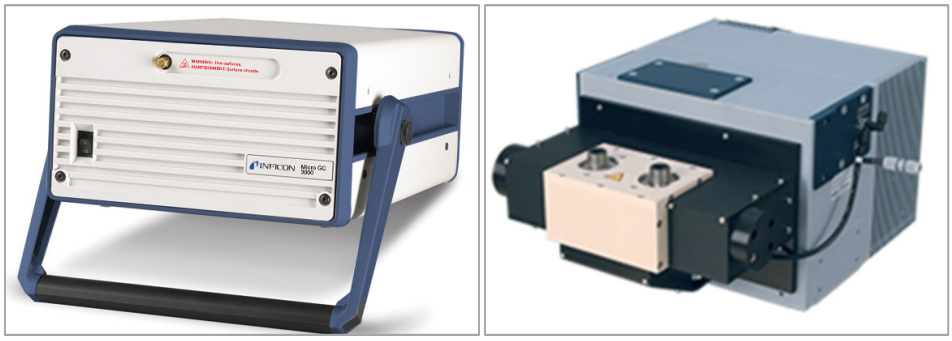

Figure 4.4: *left: GC, Agilent 3000 Micro; right: FTIR, Bruker MATRIX MG01*

4.4 Particle Analysis using SEM

The particles, which are released from the Li-ion cell during thermal runaway are analyzed using scanning electron microscopy (SEM). First pretests were performed to find a sampling method for the particles and to analyze them qualitatively using the Environmental Scanning Electron Microscope FEI ESEM Quanta 200, equipped with an energy dispersive X-ray detector (EDX, EDAX Genesis). Furthermore, a particle standard was measured and simulations (using NIST DTSA-II) were made to obtain the best possible parameters for the quantitative analysis of the particles. The quantitative analysis and the determination of the size distribution were performed using the Zeiss Sigma 300 VP equipped with an SDD Detector (Oxford) and the software AZtec (Oxford) for EDX analysis.

Figure 4.5: *Zeiss Sigma 300 VP*

5. Gas Analysis

5.1 Calibration of the Gas Chromatograph

Different analysis parameters were tested to achieve a good separation and detection. The analysis parameters are saved in a so-called GC method in the GC measurement program.

Test gases (obtained from Linde Gas GmbH, see appendix) were used and various parameters were changed, to determine, which GC method fits best for the gases in combination with the used columns. The following paragraphs describe the influence of the various parameters.

As described in Chapter 3.1.2, a TCD can analyze the components of the gas due to their thermal conductivities. Therefore, the intensity of the signal of the separated component is mainly influenced by the difference of the thermal conductivity (κ) of the carrier gas and the analyzed component. In the MolSieve 5A PLOT argon is used as carrier gas, since hydrogen is analyzed with this column and helium and hydrogen have similar thermal conductivities (κ(Helium, 300K) = 155.7 $mWm^{-1}K^{-1}$, κ(Hydrogen, 300K) = 186.6 $mWm^{-1}K^{-1}$, see *Table 5.1*). The small difference of the thermal conductivity of helium and hydrogen would result in a weak hydrogen signal. However, the disadvantage of argon is that the difference between the thermal conductivity of argon and the remaining analyzed gases (nitrogen, oxygen, carbon monoxide and methane) is smaller and therefore a weaker signal appears. The PLOT U column is operated with helium as carrier gas. The thermal conductivity of helium varies widely from the gases to be analyzed in the PLOT U column, resulting in a high intensity of the signal.

Table 5.1: Thermal conductivity at 300K of the used carrier gases (argon and helium) and the analyzed components of the vent gas of the Li-ion cell using a GC[28]

	Thermal conductivity at 300 K [mW m^{-1} K^{-1}]
Argon	17.7
Helium	155.7
Hydrogen	186.6
Nitrogen	26.0
Oxygen	26.5
Carbon monoxide	16.8
Methane	34.4
Carbon dioxide	16.8
Ethane	21.2
Ethylene	20.6
Acetylene	21.4

Although the choice of carrier gas has the highest impact on the intensity of the signal, other factors influence the separation of the different components of the gas including the

temperature, the pressure and the time. A peak of the chromatogram should be sharp, symmetric and well separated from the other peaks. The temperature of the column influences significantly the retention time and the peak width. If the temperature is too high, the peaks cannot be distinguished, since the peaks are too close. However, if the temperature is too low, a broad peak appears, resulting in a less accurate analysis of the concentration of the gas component. The injector is operated at a temperature above 100°C in order to avoid the deposition of contaminations. This is no problem for the columns, since they are heated to 180°C (MolSieve 5A PLOT column) and 160°C (PLOT U column) between the experiments.

The retention behavior considerably depends on the pressure of the carrier gas supply. To ensure an accurate measurement, the pressure should be constantly at 5.5 bar for helium (PLOT U column) as well as argon (MolSieve 5A PLOT column).

A higher injection time results in an increase of the signal and a slight decrease of the retention time. The duration of the measurement was adjusted to 2.5 minutes, since former experiments showed that every expected gas component elutes before.

The pressure of the column has to overcome a limit of 30 psi (2.07 bar), otherwise no chromatogram can be obtained. However, no significant changes were recognized when further increasing the pressure. A change of the pressure of the column and the sample pump time have only a little impact on the retention behavior.

After testing the different methods, the best one for the gases to be measured was chosen. The parameters of this method for column A (MolSieve 5A PLOT column) and B (PLOT U column) are shown in *Figure 5.1.*

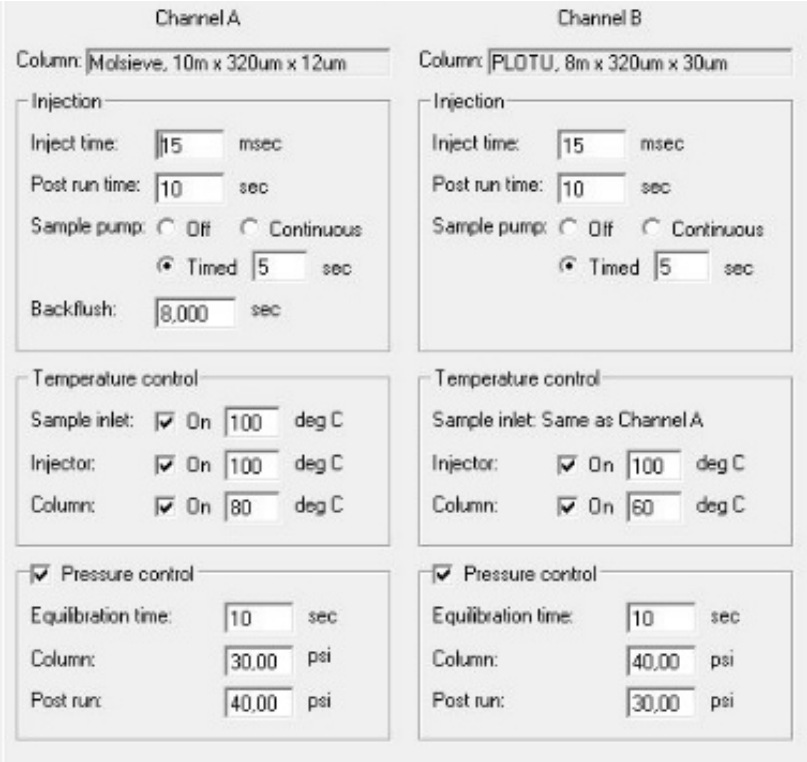

Figure 5.1: *Parameters of the GC method of choice for column A (MolSieve 5A PLOT column) and column B (PLOT U column)*

The GC method, which leads to the best results, was calibrated with synthetic air and three test gases with different concentrations of carbon dioxide, acetylene, ethylene, ethane, nitrogen, carbon monoxide and methane. Every test gas and the synthetic air was measured five times. The average value of every substance was used to generate the calibration curve for every substance. Within the calibration range the curve can be assumed as linear and the concentration can be calculated easily using the response factor (RF), which corresponds to the slope of the calibration curve.

$$RF = \frac{Amount\ in\ \%}{Area} \qquad (4)$$

Exemplarily, a calibration curve of CO_2 is shown in *Figure 5.2.*

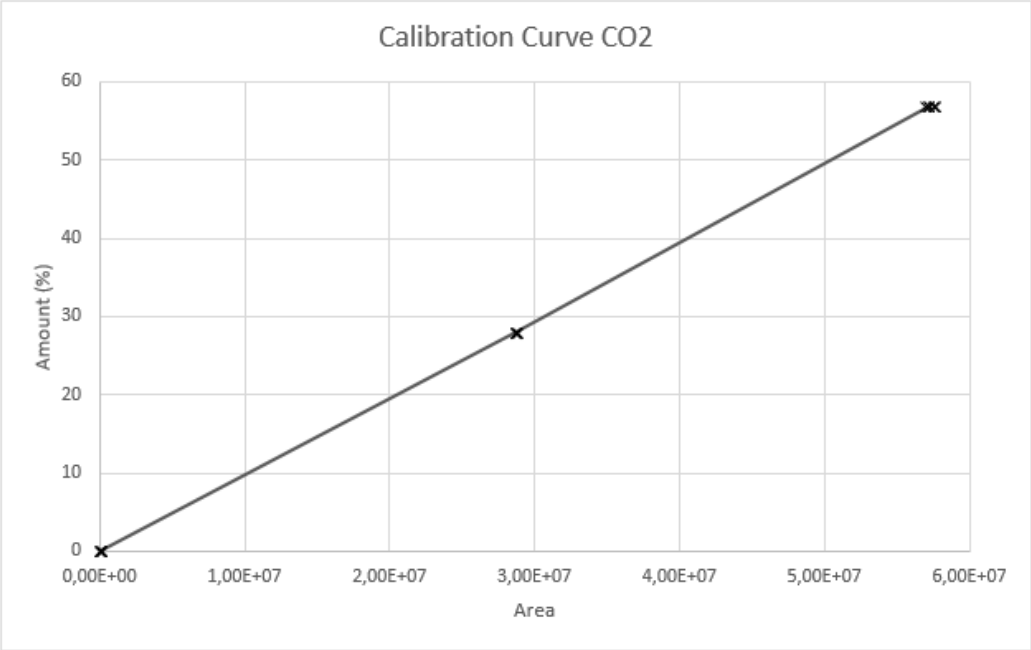

Figure 5.2: *Calibration curve of CO_2; amount of the component versus the area of the peak*

5.2 Results of the Gas Analysis

The gas, which is released by the Li-ion cell during thermal runaway was measured four times by GC. *Table 5.2* shows the average measured gas composition.

Table 5.2*: Concentration of the gas from the reactor after thermal runaway of experiment 1, 2, 3 and 4 determined using a GC*

	Experiment 1 c / %Vol	Experiment 2 c / %Vol	Experiment 3 c / %Vol	Experiment 4 c / %Vol
H_2	6.92 ± 0.11	7.24 ± 0.30	3.88 ± 0.10	5.82 ± 0.21
O_2	0.39 ± 0.02	0.59 ± 0.00	-	0.07 ± 0.03
N_2	70.13 ± 0.61	72.69 ± 1.13	70.33 ± 1.03	70.14 ± 1.01
CH_4	0.67 ± 0.01	0.82 ± 0.03	0.74 ± 0.03	0.87 ± 0.03
CO	3.56 ± 0.06	3.53 ± 0.15	1.83 ± 0.08	2.69 ± 0.10
CO_2	7.89 ± 0.26	6.47 ± 0.29	8.65 ± 0.46	9.25 ± 0.37
C_2H_4	0.88 ± 0.03	1.45 ± 0.06	1.98 ± 0.07	1.00 ± 0.04
C_2H_6	0.17 ± 0.01	0.16 ± 0.01	0.19 ± 0.01	0.23 ± 0.01
C_2H_2	-	-	-	-

Table 5.3*: Concentration of the gas from the reactor after thermal runaway of experiment 1 determined using a GC and an FTIR and the resulting concentration in percent per volume*

Gas	FTIR	GC	Result
	c/%Vol	c/%Vol	c/%Vol
O_2	-	0.39	0.39
N_2	-	70.13	70.13
H_2	-	6.92	6.92
C_2H_2	0.02	0	0.02
C_2H_4	1.17	0.88	0.88
C_2H_6	0	0.17	0.17
CH_4	0.71	0.67	0.71
CO	3.71	3.56	3.56
CO_2	11.37	7.89	11.37
DEC	0.95	-	0.95
DMC	0	-	0
EC	0	-	0
EMC	0.28	-	0.28
H_2O	3.15	-	3.15
C_6H_{14}	0	-	0
HF	0	-	0
C_4H_{10}	0.41	-	0.41

Not every component of the gas can be analyzed using GC. Therefore, an FTIR is used additionally. *Table 5.3* shows the results obtained from GC and FTIR for the vent gas analysis of experiment 1 (the other can be found in the appendix). Some gases are measured by the GC as well as the FTIR. For each component either GC or FTIR has a better accuracy. This was investigated by measuring test gases (obtained from Linde Gas GmbH, see appendix). The accuracy depends on the concentration of the component and the interference with other components. The concentration of each gas of the preferred method is marked in green in *Table 5.3*.

To know the amount of gases which are released from the cell, the amount of nitrogen originating from the inert atmosphere of the reactor, has to be subtracted. The composition of the gas of experiment 1 is shown in *Figure 5.3.* The main compounds of the gas released by the Li-ion battery are carbon dioxide (CO_2) with about 39 % and hydrogen (H_2) with approximately 24 %. Also, carbon monoxide (CO, 12.8 %) and water (H_2O, 10.9 %) are main parts of the gas. A minor fraction makes up oxygen (O_2, 1.3 %), acetylene (C_2H_2, 0.1 %), ethylene (C_2H_4, 3.1 %), ethane (C_2H_6, 0.6 %), methane (CH_4, 2.4 %), diethyl carbonate (DEC, 3.3 %), ethyl methyl carbonate (EMC, 1.0 %) and butane (C_4H_{10}, 1.4 %).

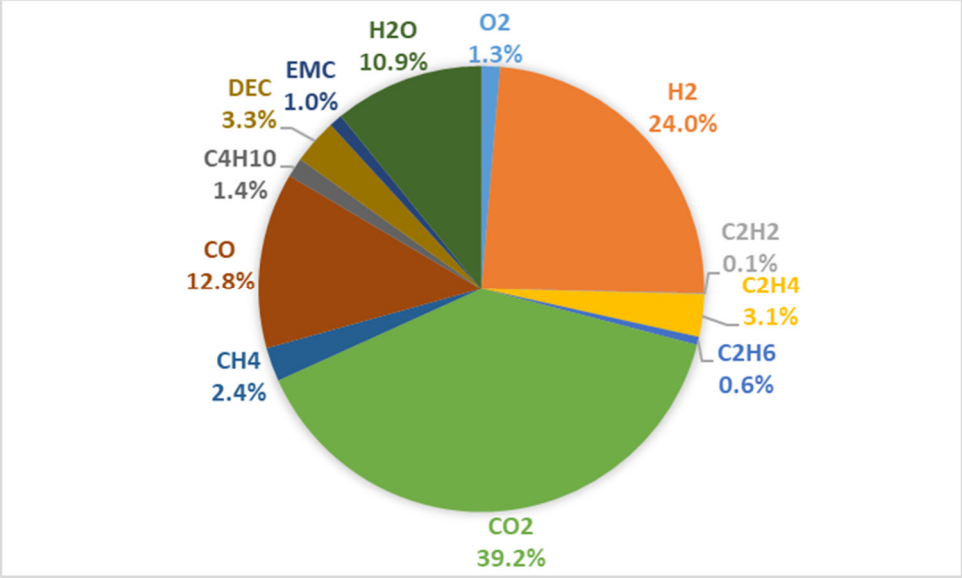

Figure 5.3: *Composition of the gas released form the Li-ion cell at thermal runaway of experiment 1*

Equations 5-16 describe possible chemical reactions, which might explain how the gases are generated.

Decomposition of the SEI lead to oxygen, ethylene and carbon dioxide:[6]

$$(CH2OCO_2Li)_2 \rightarrow Li_2CO_3 + C_2H_4 + CO_2 + 0.5\ O_2 \quad (5)$$

Carbon (e.g. from the anode) and hydrogen can react to methane:[29]

$$C + 2\ H_2 \rightarrow CH_4 \quad (6)$$

Carbon can also react with oxygen to carbon monoxide:[8]

$$C + 0.5\ O_2 \rightarrow CO \quad (7)$$

Carbon monoxide can further react with water to carbon dioxide and hydrogen:[8]

$$CO + H_2O \rightarrow CO_2 + H_2 \quad (8)$$

The electrolyte DEC can react with oxygen to water and carbon monoxide/dioxide:[6]

$$C_5H_{10}O_3\ (DEC) + 3.5\ O_2 \rightarrow 5\ CO + 5\ H_2O \quad (9)$$

$$C_5H_{10}O_3\ (DEC) + 6\ O_2 \rightarrow 5\ CO_2 + 5\ H_2O \quad (10)$$

The electrolytes DMC can react with lithium to ethane:[30]

$$C_3H_6O_3\ (DMC) + 2\ Li \rightarrow C_2H_6 + Li_2CO_3 \quad (11)$$

Hydrogen can result from the reaction of water with lithium or the binder (CH_2CF_2):[8,9]

$$2\ Li + H_2O \rightarrow Li_2O + H_2 \quad (12)$$

$$Li + CH_2CF_2 \rightarrow LiF + C_2HF + 0.5\ H_2 \quad (13)$$

The conducting salt $LiPF_6$ can react with water to hydrogen fluoride:[31]

$$LiPF_6 \rightarrow LiF + PF_5 \quad (14)$$

$$PF_5 + H_2O \rightarrow POF_3 + 2\ HF \quad (15)$$

$$LiPF_6 + H_2O \rightarrow LiF + POF_3 + 2\ HF \quad (16)$$

5.3 Discussion of the Gas Analysis

The gas released by the Li-ion cell during thermal runaway was analyzed. With the gas chromatograph, O_2, N_2 H_2, C_2H_2, C_2H4, C_2H_6, CH_4, CO and CO_2 were analyzed on a MolSieve 5A PLOT column and a PLOT U column. Quantifications of C_2H_2, C_2H_4, C_2H_6, CH_4, CO, CO_2, DEC, DMC, EC, EMC, H_2O, C_6H_{14}, HF and C_4H_{10} were performed using a Fourier transformation infrared spectrometer. Some of the gas components were measured with both methods (FTIR and GC). Only the results from the method with the smaller error were used for further discussions. For C_2H_2, CH_4, CO and CO_2 the results of the FTIR show a higher accuracy, while for C_2H_4 and C_2H_6 the GC is more accurate.

The main gas components of the released gas are CO_2 (30-50 %) and H_2 (20-35 %). Moreover, CO and H_2O are components with a larger fraction of about 10 % - 15 % each. Only few percentages of O_2, C_2H_2, C_2H_4, C_2H_6, CH_4, DEC, EMC and C_4H_{10} are contained in the gas. No hydrogen fluoride (HF) could be detected. However it is reported various times in literature, that the conduction salt reacts with water, forming HF.[6,10,31] It is presumed, that the HF reacts further with materials inside the reactor, since it is highly reactive. Several of these gases are toxic or inflammable. For example carbon monoxide is extremely inflammable and toxic [32] and hydrogen is extremely inflammable.[33]

Overall, the combination of GC and FTIR allows a good analysis of gases formed during thermal runaway. The analysis confirms the formation of hazardous gases.

6. Particle Analysis

6.1 Sampling and Sample Preparation

During thermal runaway, particles from the cell are spread out in the reactor. To analyze these particles and to achieve utilizable results, various sampling methods were tested and compared. The sampling method should provide a good separation, since this enables an automated determination of size and elemental composition of the particles. Additionally, the analyzed particles should represent all kinds of particles.

First, metal sheets with an area of 1 cm x 1 cm were placed on two sample holders inside the reactor before the thermal runaway experiment was started. One of the sample holders was placed at the shield between sample chamber and wiring and another one on the top of the upper pressure plate. For all experiments, titanium sheets (99.6 % pure titanium, thickness: 0.1 mm)[34] were used and for two experiments additionally a silicon metal sheet (sliced silicon-wafer) was tested. Titanium and silicon were chosen, since these elements are not expected to be contained in the battery. After thermal runaway, the metal sheets are applied to an SEM stub using a double sided adhesive carbon tape (in the following named: carbon tape). *Figure 6.1* shows the sampling method with the titanium and silicon sheets and their positioning within the reactor.

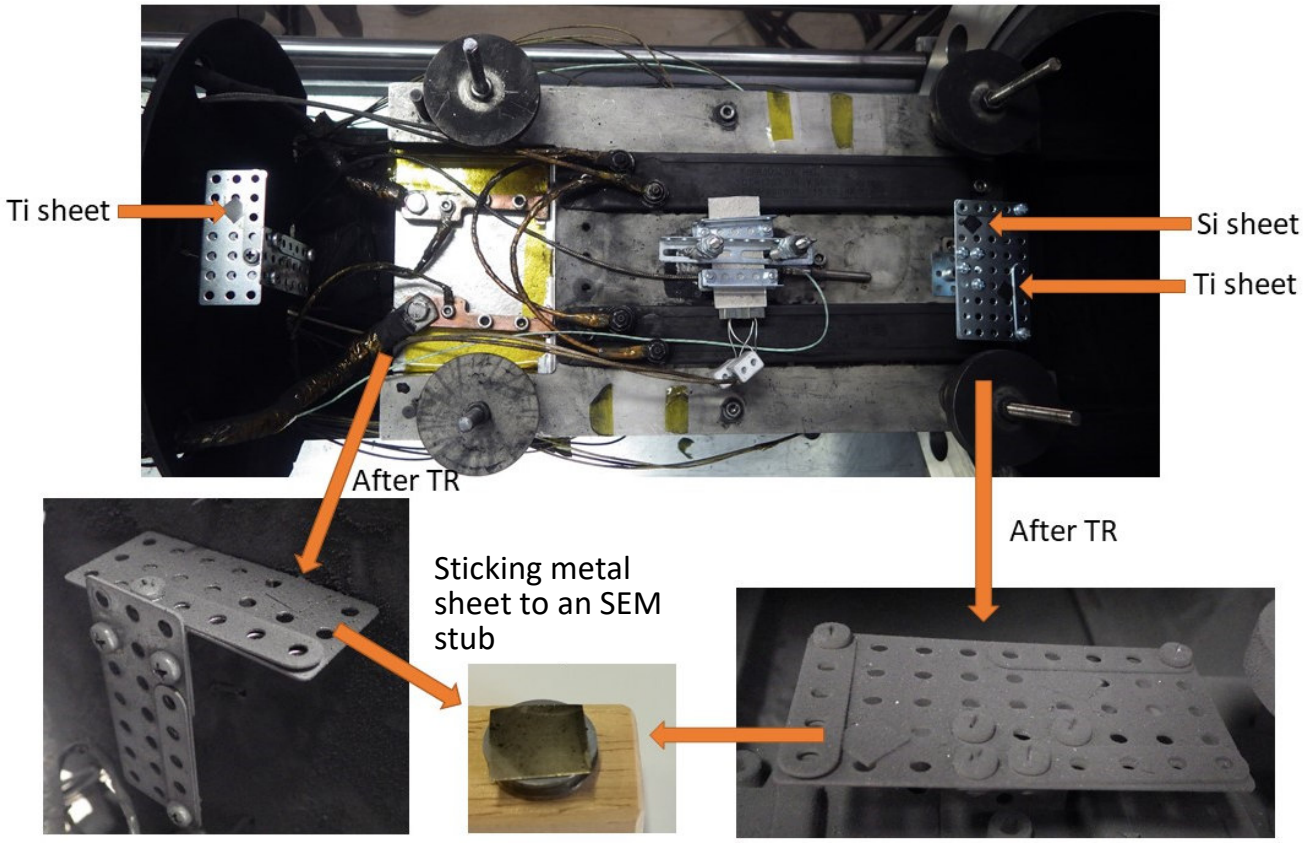

Figure 6.1: *Sampling with titanium and silicon sheets*

As a second method, the particles were directly collected from the reactor after thermal runaway using an SEM stub. A carbon tape was applied to the SEM stub and used like a stamp to stick the powder on the tape. (*Figure 6.2*)

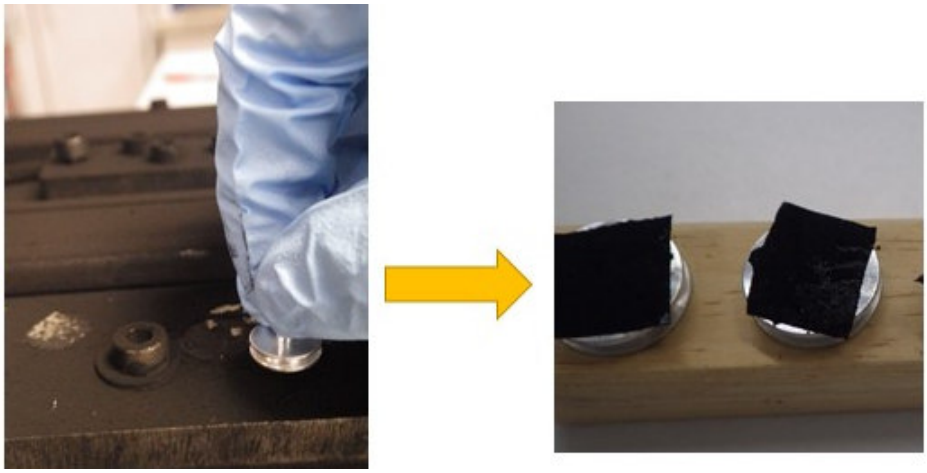

Figure 6.2: *Sampling by "stamping" directly from the reactor*

Another method is the direct sampling of the powder from the top of the upper pressure plate using a spatula (*Figure 6.3*). Afterwards the powder of the direct sampling has to be attached to a carbon tape on an SEM sample holder in various ways. The main disadvantage of these methods is the additional preparation step, which might introduce further errors.

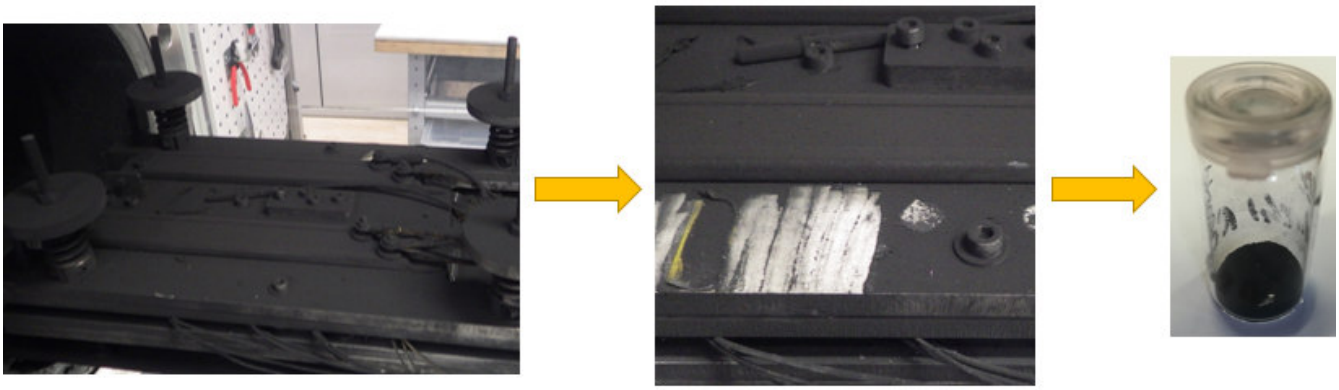

Figure 6.3: *Direct sampling of powder from the upper pressure plate*

One method to apply the particles of the direct sampling onto the carbon tape is to sprinkle them onto the tape by using a spatula. The advantage is, that all types of particles, independent of size and weight, are applied to the tape. However, the particles are not well separated and therefore the individual particles cannot be analyzed separately by automated particle analysis.

Another method was to put some particles of the direct sampling onto a glass microscope slide and use an SEM stub like a stamp as described before. The advantage was that the particles were evenly distributed. However, the particles were not sufficiently separated.

A further method was to take up the powder of the direct sampling by a pipette and spray them onto a carbon tape. The particles covered evenly the carbon tape. However, since the powder is inhomogeneous, the bigger/heavier particles were not taken up by the pipette. Therefore, with this method the particles are preselected and definitely not representative for the whole sample.

The method of choice was to deposit the particles by air-jetting. A small amount of the particles is given into a glass vial with a carbon tape attached to an SEM stub. The glass vial is closed except for a hole, where a jet of air (using Air Power from Green Clean[35]) can be blown through (*Figure 6.4*). By the jet of air, the particles are separated evenly and even the bigger and heavier particles stick to the carbon tape. The argument for choosing this method was the possibility of an automated size analysis.

Figure 6.4: *Sampling by air-jetting*

The commonly used method in literature[25, 26, 27] of making a suspension of water or alcohol with the particles was not chosen in this case, since the composition of the powder is unknown and therefore chemical reactions could happen.

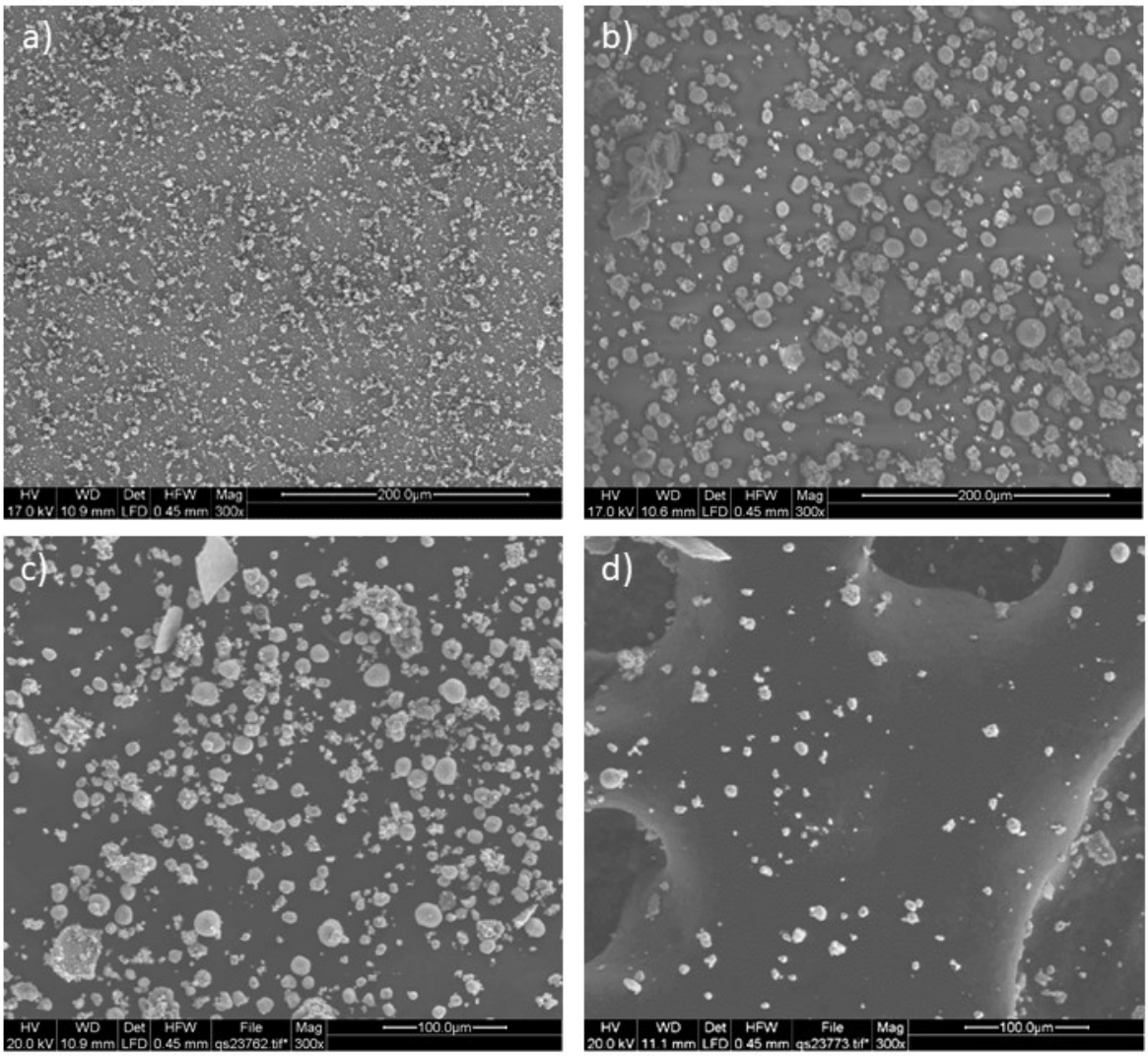

Figure 6.5: *Comparison of sampling methods: a) titanium sheet, b) „stamping" from the reactor, c) sprinkle particles on a tape using a spatula and d) air-jetting particles on a carbon tape*

In *Figure 6.5* four sampling methods are compared by using the low vacuum mode of the ESEM Quanta 200. In contrast to the other sampling methods, the particles applied by using a jet of air are assessed to be well separated. Therefore, the air jetting method is used for the quantitative analysis and the investigation of the size distribution of the particles.

6.2 Pretests

Different pretests were carried out. First, a spectroscopic measurement of the blank adhesive carbon tape, where the particles are to be applied to, was performed. Further, the particles were analyzed qualitatively, and a first analysis of the elemental composition was performed. Moreover, a first characterization of the size distribution of the particles of the Li-ion cell after thermal runaway was obtained. These tests were performed using the ESEM Quanta 200 instrument.

For the further analysis, the Zeiss SEM Sigma 300 VP and the detector (X-max 80) for energy dispersive X-ray spectroscopy (SDD-technology from Oxford) combined with the analyzation software AZtec (Oxford) is used. Exemplarily, an elemental mapping of an area on a titanium metal sheet, which was mounted in the reactor during thermal runaway, was performed. A particle standard is measured to show the dependence of the determined elemental composition on the size of the particle. Simulations with the software NIST DTSA-II are performed to find the beam energy, which enables the most accurate determination of the elemental composition.

6.2.1 Blank Measurement of the Adhesive Carbon Tape

The particles are attached to a substrate. Due to the interaction volume of the electrons, also the influence of the substrate has to be considered. Therefore, a blank measurement has to be performed. *Figure 6.6* shows the EDX spectrum of a blank measurement of the adhesive carbon tape, where the particles are to be attached to. The measurement was performed with a beam energy of 10 keV in the variable pressure mode (nitrogen as imaging gas) using the Zeiss SEM Sigma 300 VP. Beside the expected carbon peak, also a significant oxygen peak is detected.

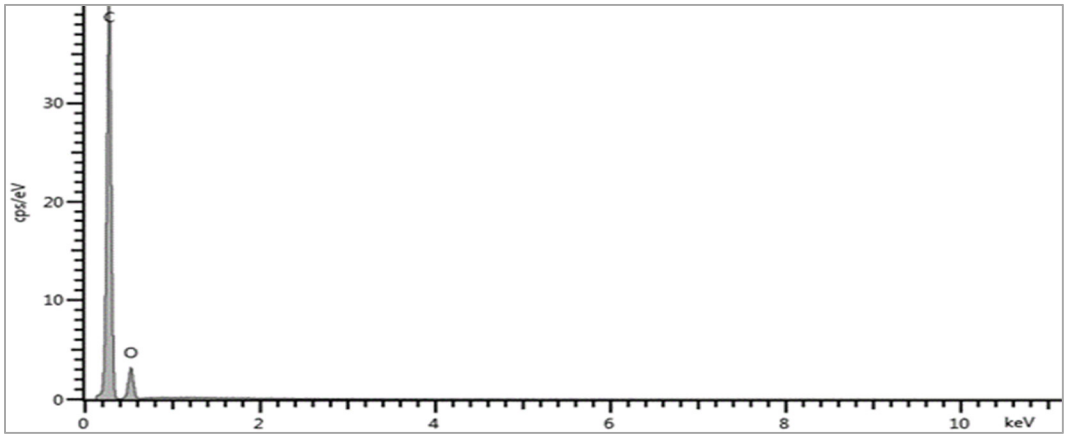

Figure 6.6: *EDX-spectrum of an adhesive carbon tape; beam energy = 10 keV; VP mode*

6.2.2 Elemental Composition of the Particles

First it was determined which elements are contained in the particles of the Li-ion cell in the low vacuum mode of the ESEM, using water vapor as imaging gas at a pressure of 10 Pa. Then, various areas of the sample with a beam energy of 17 keV, which has approximately the double energy of the element with the highest characteristic X-ray energy (nickel) are analyzed (*Figure 6.7*). The particles contain: carbon (C), oxygen (O), aluminum (Al) fluorine (F), nickel (Ni), phosphor (P), manganese (Mn) and cobalt (Co).

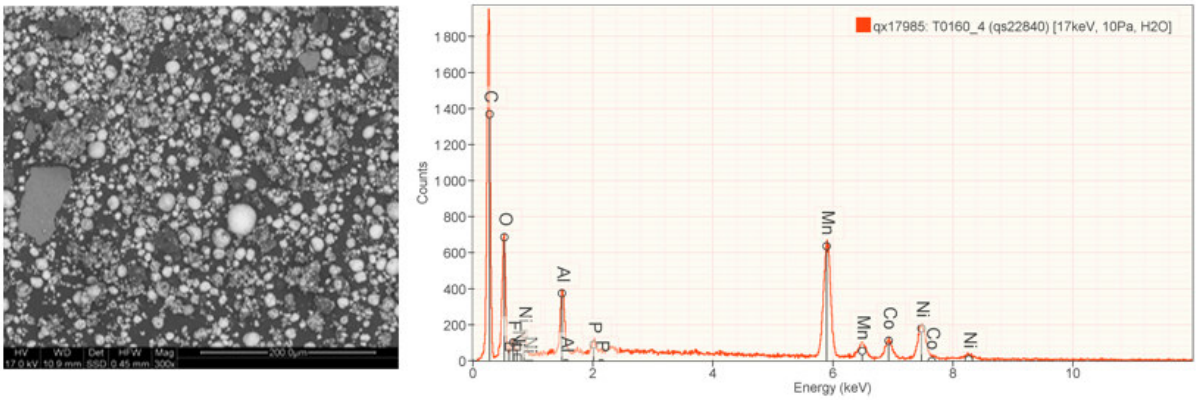

Figure 6.7: *Qualitative analysis of particles of experiment 2, beam energy = 17 keV; pressure = 10 Pa*

Then certain particles are analyzed. Overall, the particles can be classified in four groups: particles, which mainly contain aluminum and oxygen (*Figure 6.8*); particles, which mainly contain oxygen, nickel, manganese and cobalt (*Figure 6.9*); particles, which mainly contain carbon (*Figure 6.10*); particles, which mainly contain manganese and oxygen (*Figure 6.11*)

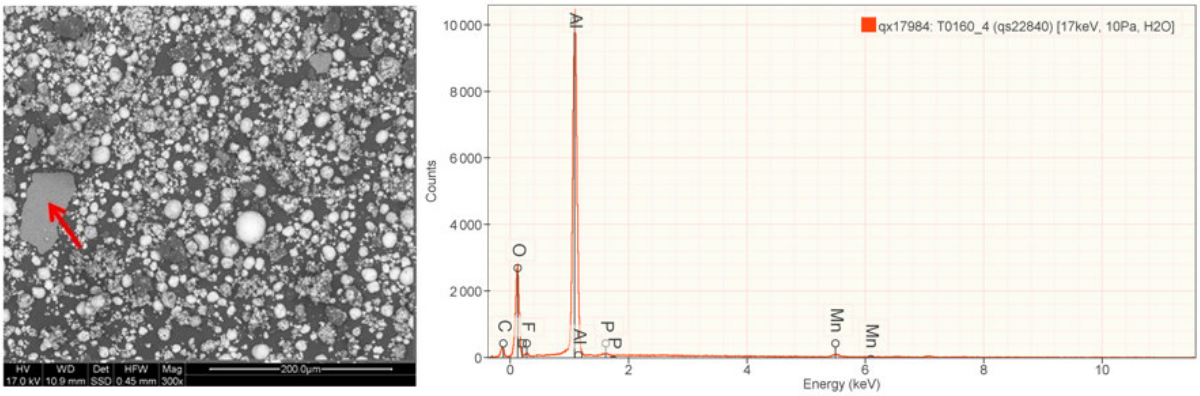

Figure 6.8: *Particle, which mainly contains aluminum and oxygen, experiment 2; beam energy = 17 keV; pressure = 10 Pa*

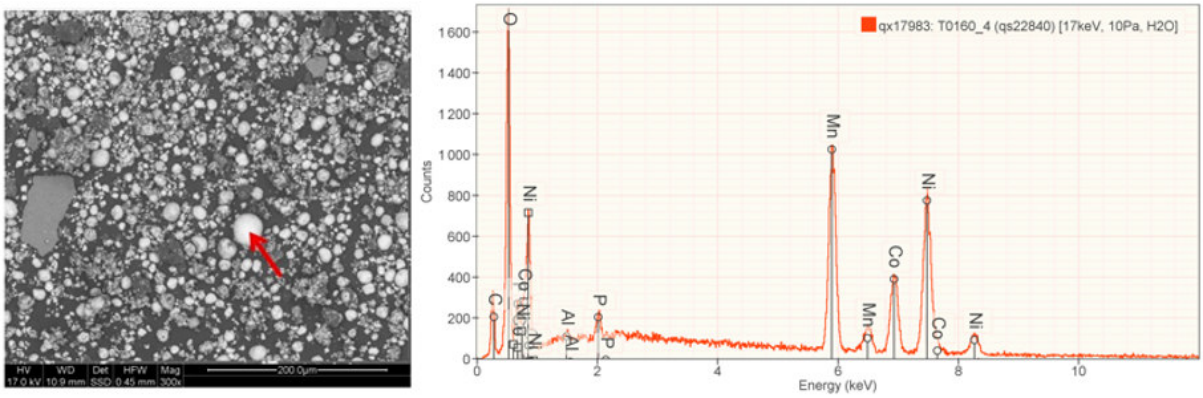

Figure 6.9: *Particle, which mainly contains oxygen, nickel, manganese and cobalt; experiment 2; beam energy = 17 keV; pressure = 10 Pa*

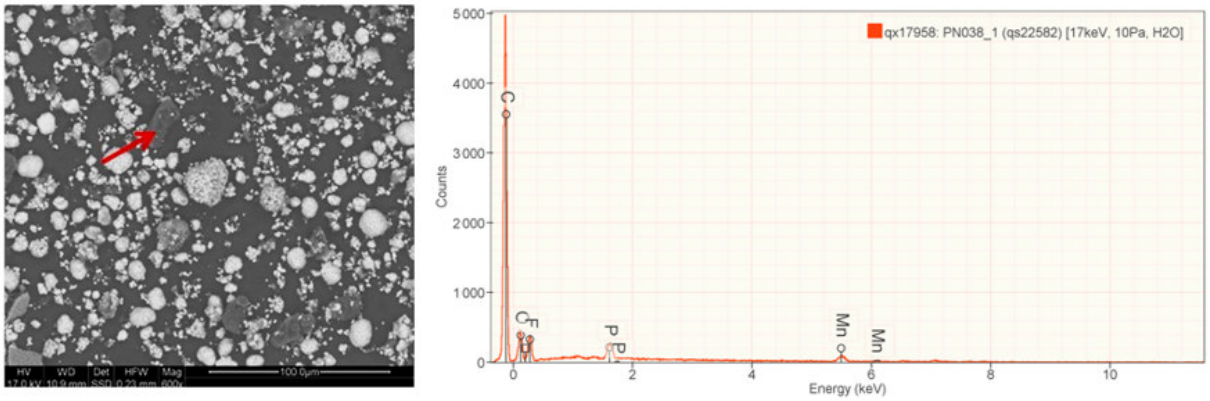

Figure 6.10: *Particle which mainly contains carbon; experiment 2, beam energy = 17 keV; pressure = 10 Pa*

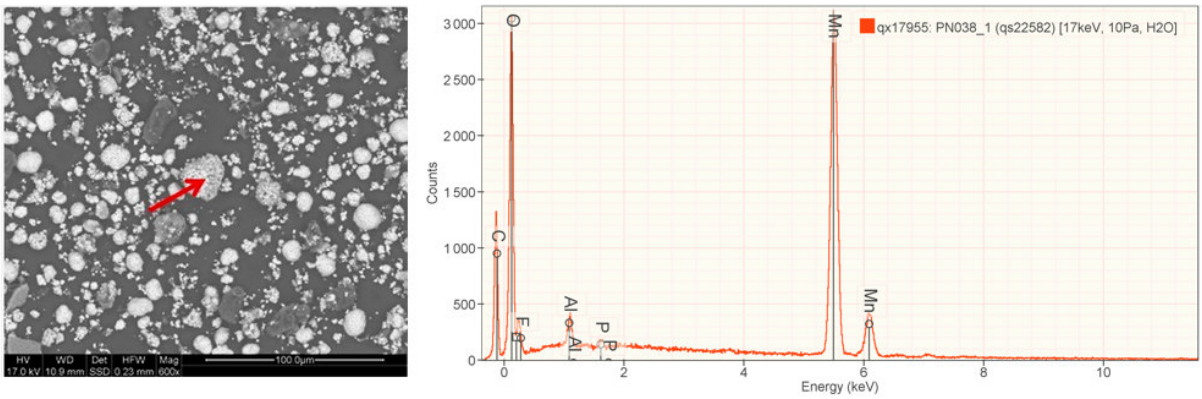

Figure 6.11: *Particle which mainly contains oxygen and manganese; experiment 2, beam energy = 17 keV; pressure = 10 Pa*

6.2.3 Determination of the Particle Size Distribution

An introductory size distribution of particles of experiment 3 is performed. Therefore, BSE images with a high magnification are taken in the variable pressure mode of the ESEM Quanta 200 at a pressure of 10 Pa (water vapor as imaging gas) and with a beam energy of 15 keV. The BSE images are stitched together using the program photoshop. The stitched images are analyzed using the software Fiji[36]. With this software the stitched BSE micrograph can be converted into a binary image by thresholding. The BSE image and a corresponding binary image are shown in *Figure 6.12.*

The size distributions of the particles of the generated binary images is shown in *Table 6.1.* To estimate the uncertainty, the threshold was set three times by different operators. As a result, especially the amount of particles between 0 – 0.2 µm² vary heavily. Depending on the operator the size distribution and the total amount of particles differs. Typically, a threshold cannot be set perfectly for each particle, which is also the reason for the high number of particles smaller

than 0.5 µm². Additionally, image noise can contribute to this circumstance. So, it has to be noted, that the error of this analysis is quite high.[37]

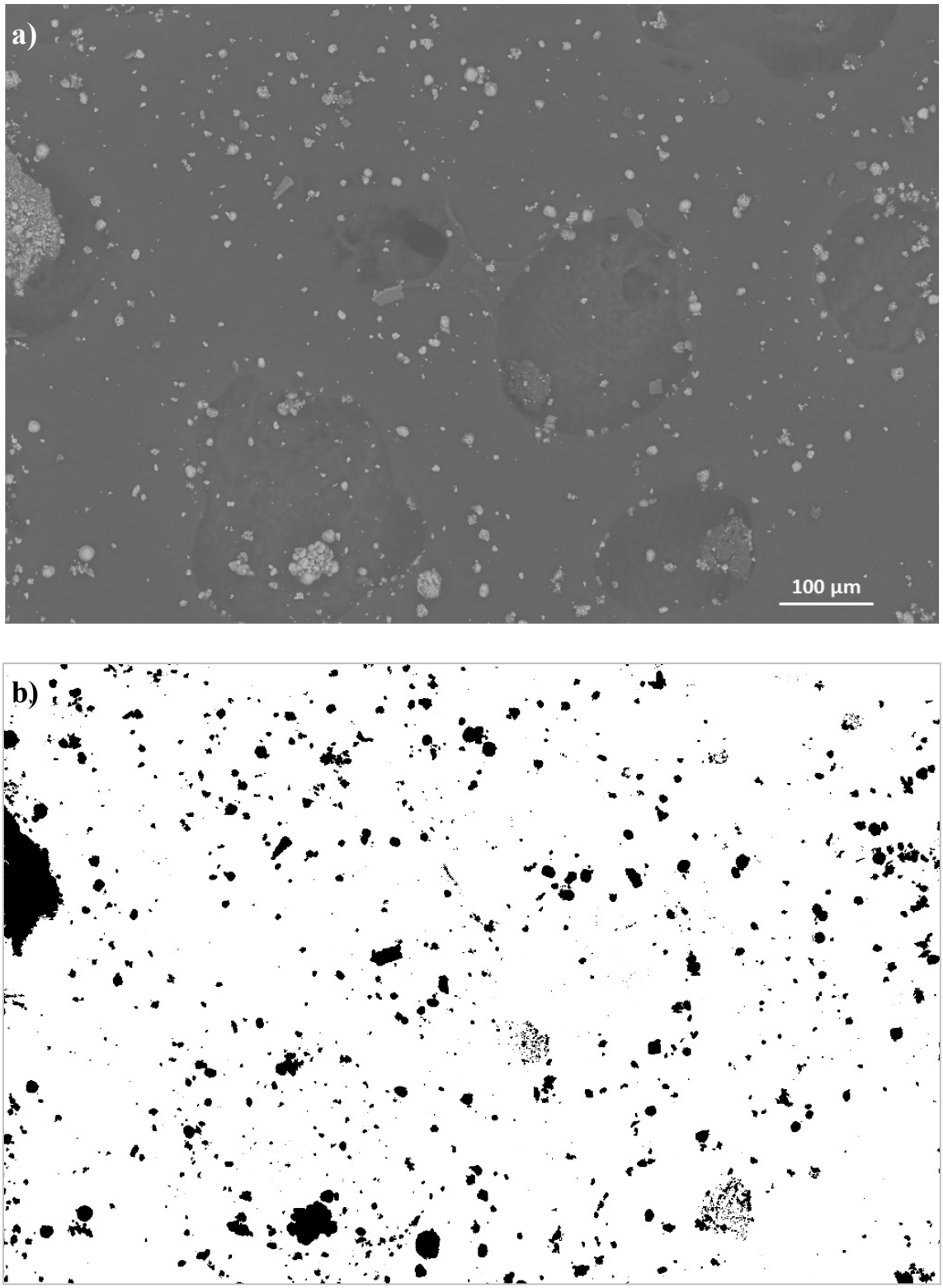

Figure 6.12: *a) BSE image of particles of experiment 3 on a carbon tape; b) binary image resulting from the BSE image via choice of the grey level threshold*

Table 6.1: *Size distribution of the particles of the Figure 6.12; Square brackets "[" mean that the value is included, round brackets ")" mean that the value is excluded*

	Operator 1		Operator 2		Operator 3		Average
Area of particles in µm²	Amount of particles	Amount of particles in %	Amount of particles	Amount of particles in %	Amount of particles	Amount of particles in %	Amount of particles in %
[0-0.2)	198	12.7	454	23.7	311	17.8	18.1 ± 5.5
[0-0.5)	178	11.4	212	11.0	207	11.9	11.4 ± 0.4
[0.5-1.0)	190	12.2	167	8.7	190	10.9	10.6 ± 1.8
[1.0-2.0)	182	11.7	181	9.4	177	10.2	10.4 ± 1.1
[2.0-3.0)	101	6.5	109	5.7	109	6.3	6.1 ± 0.4
[3.0-4.0)	59	3.8	77	4.0	54	3.1	3.6 ± 0.5
[4.0-5.0)	44	2.8	42	2.2	43	2.5	2.5 ± 0.3
[5.0-10.0)	132	8.5	158	8.2	160	9.2	8.6 ± 0.5
[10.0-20.0)	142	9.1	149	7.8	133	7.6	8.2 ± 0.8
[20.0-30.0)	95	6.1	95	5.0	95	5.5	5.5 ± 0.6
[30.0-40.0)	52	3.3	54	2.8	53	3.0	3.1 ± 0.3
[40.0-50.0)	39	2.5	48	2.5	47	2.7	2.6 ± 0.1
[50.00-100)	86	5.5	92	4.8	85	4.9	5.1 ± 0.4
[100-infinity)	62	4.0	81	4.2	79	4.5	4.2 ± 0.3
Total number of particles	1560		1919		1743		

6.2.4 Elemental Mapping of Particles on a Titanium Metal Sheet

Figure 6.13 shows a BSE image of an area of a titanium metal sheet, which was positioned in the reactor during the thermal runaway experiment 1. In this area an elemental mapping is performed *(Figure 6.14)*. It shows the spatial element distribution of the sample using a false color representation.

The measurement was performed with a beam energy of 10 keV in the variable pressure mode of the SEM Sigma 300 VP at a pressure of 10 Pa using nitrogen as imaging gas. Due to the variable pressure mode, the skirt effect occurs, which results in a less accurate determination compared to the high vacuum mode. The elements titanium (Ti), carbon (C), aluminum (Al), oxygen (O), phosphorous (P), fluorine (F), cobalt (Co), manganese (Mn) and nickel (Ni) are detected. The position of cobalt and nickel coincide. The lighter colored points of manganese match with cobalt and nickel. Some particle significantly contains aluminum. Nearly every particle contains fluorine. Few particles, which contain phosphorus, are found. Oxygen can be found in every particle.

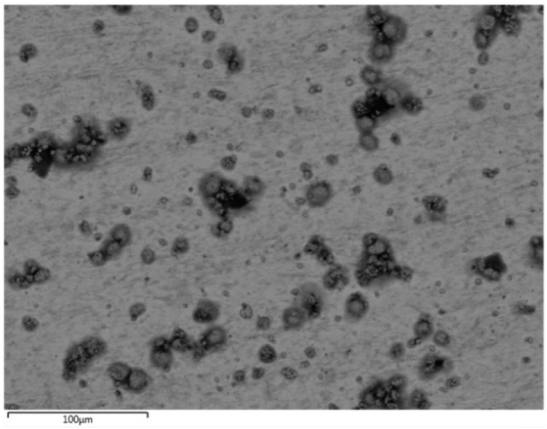

Figure 6.13: *BSE image of an area of a Ti metal sheet, which corresponds to the measuring area of the elemental mapping*

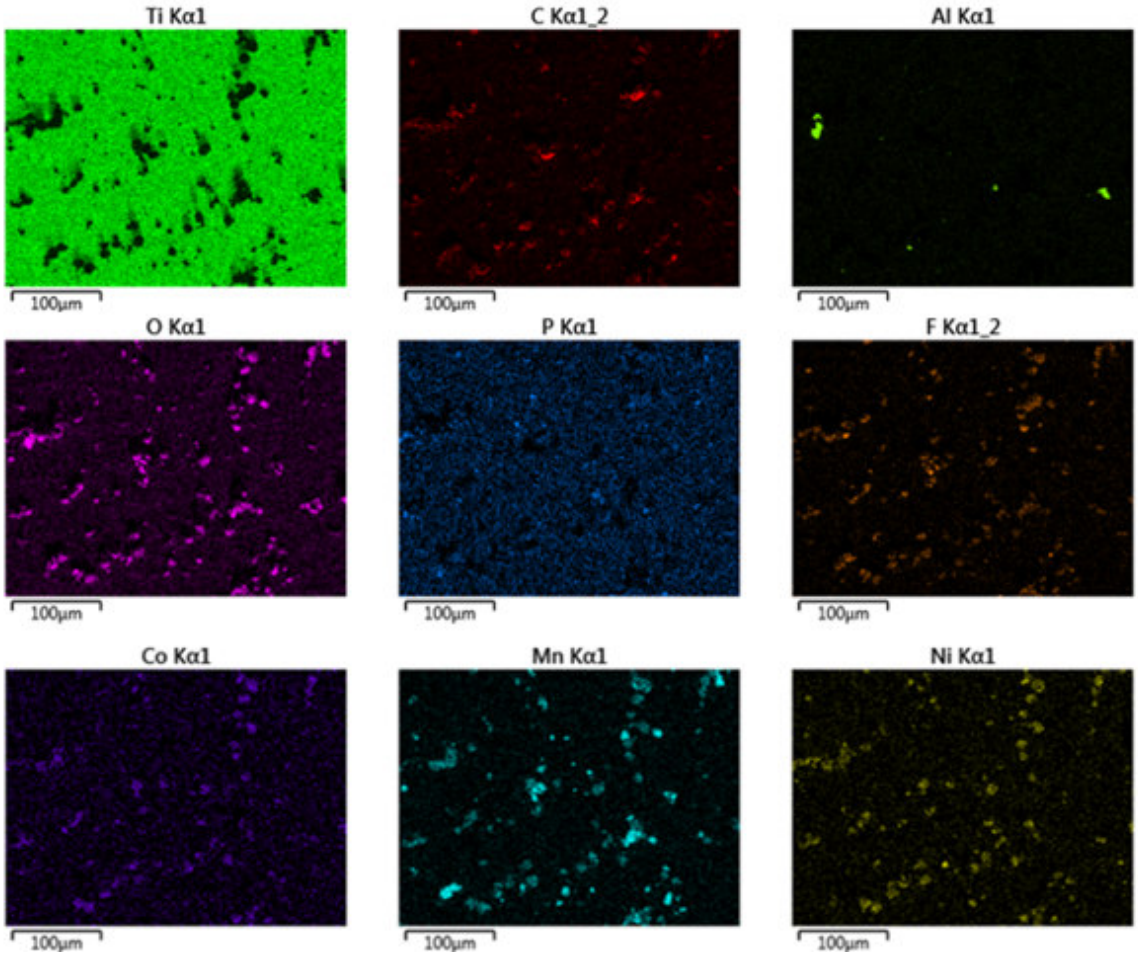

Figure 6.14: *Distribution of the elements Ti, C, Al, O, P, F, Co, Mn and Ni over the sample, as determined from elemental mapping. The elements are color coded.*

6.2.5 Determination of the Elemental Composition of a Particle Standard

To verify the accuracy of the measurement of particles using the SEM Zeiss Sigma 300 VP equipped with the EDX system, a $Mg(OH)_2$ standard with known chemical composition was investigated.[38] The $Mg(OH)_2$ standard was coated with carbon (10 nm) and measured in the HV mode with a beam energy of 7 keV. The expected chemical composition of the standard

$Mg(OH)_2$ correlates to 43.11 wt% magnesium (Mg) and 56.89 wt% of oxygen (O). The element hydrogen (H) cannot be determined by a SEM/EDX (see *Chapter 3.3.2.3*).

Figure 6.15 shows the weight fraction of Mg against the area of 350 particles. It can be seen that the quantification of the elemental composition gets more accurate with bigger particle diameter (the value 43.11 wt% is indicated). In *Table 6.2* the average atomic percentage of three size classes were compared. The smallest particles with a diameter smaller than 0.52 µm display a relative error of about 21 % and the particles with a diameter between 0.52 µm and 1.09 µm have a relative error of approximately 10 %. A far higher level of accuracy is found for the particles which have a diameter bigger than 1.09 µm with a relative error of only about 1 %.

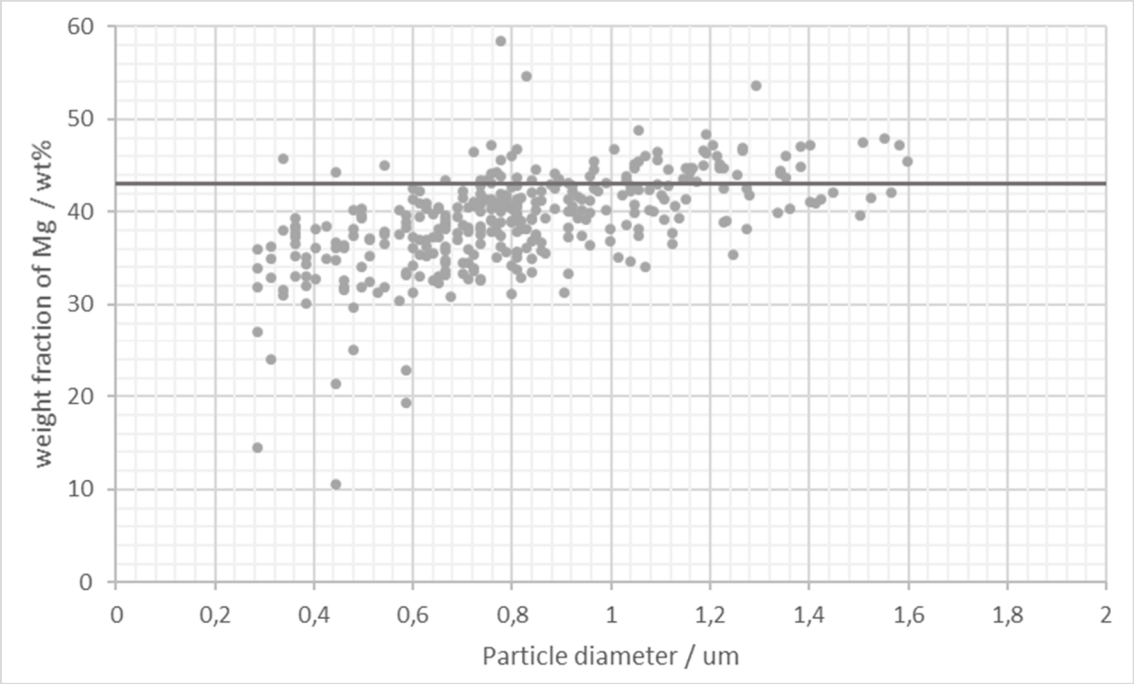

Figure 6.15: *Weight fraction of manganese plotted against the particle size*

Table 6.2: *Average Mg fraction of three size classes (< 0.52 µm, 0.52 - 1.09 µm, > 1.09 µm), rel. error rounded; the choice of the diameter range is according to the specifications of the standard*

Particle diameter / µm	**Average weight fraction of Mg wt%**	**Rel. error**
< 0.52	34.08	21
0.52 - 1.09	39.13	10
> 1.09	43.45	1

6.2.6 Influence of the Size of the Particle on the Determined Elemental Composition

The choice of the beam energy plays a major role for the accurate determination of the elemental composition. *Figure 6.16* shows simulated elemental compositions versus the size of spherical Al_2O_3 particles on a carbon substrate using a beam energy of 15 keV. Particles with a diameter bigger than 1.5 µm have the same determined atomic fraction as the bulk sample.

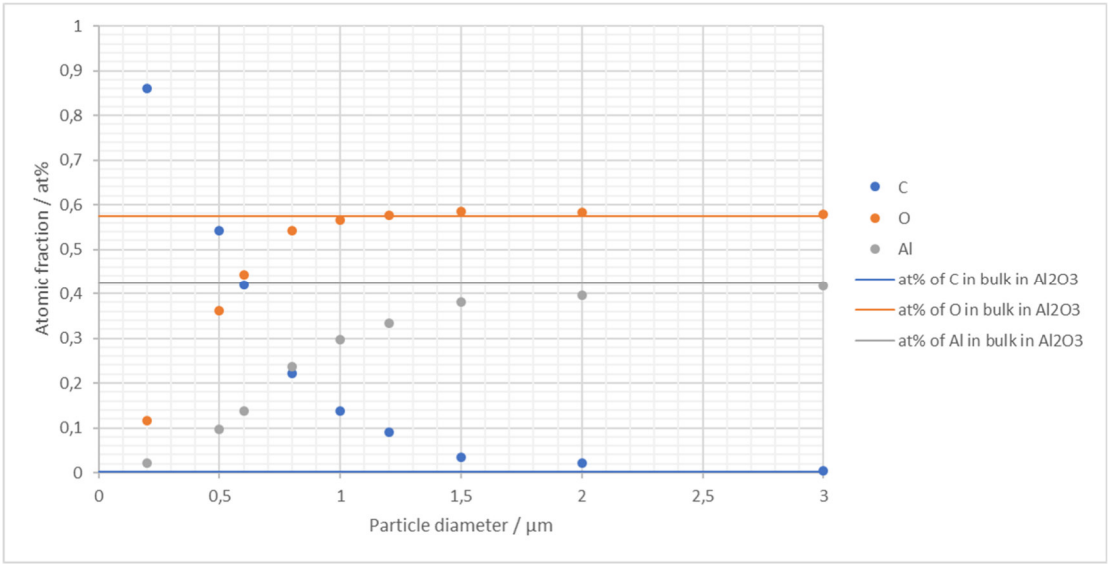

Figure 6.16: *Influence of the diameter of simulated spherical Al_2O_3 particles (on a carbon substrate) on the determined atomic fraction, compared to a bulk material of Al_2O_3; beam energy = 15 keV*

As shown in Chapter 3.3.1, the interaction volume is determined by the beam energy. The size of the interaction volume should be smaller than the particle, since the electrons travel through the side and the bottom of the particle, which leads to a faulty result. However, the beam energy must not be lower than the critical beam energy to excite also the high energetic elements in the sample.

Therefore, the lowest possible beam energy, where all present elements of the sample are detected by the EDX detector of the Zeiss Sigma 300 VP, was searched. With a beam energy of 9 keV the K-Line of Co (Kα = 6.9 keV) was not always detected. A beam energy of 10 keV for the measurements of the particles of the Li-ion cell was chosen to ensure the detection of the Co K-Lines.

Then, simulations of some particles, which are expected to be contained by the Li-ion cell, are performed with different sizes at a beam energy of 10 keV. The particle of *Figure 6.8* contains Al and O and the particle of *Figure 6.11* contains Mn and O. The formulas Al_2O_3 and Mn_2O_3 can be assumed. *Figure 6.17* and *Figure 6.18* compare the determined atomic fraction of

particles with different diameter using simulations of Mn_2O_3 and Al_2O_3 particles with diameters between 0.1 µm and 3 µm. Particles with a composition of Al_2O_3 have the same atomic fraction as a bulk sample if they exceed a diameter of 0.7 µm (*Figure 6.17*). In *Figure 6.18* it can be seen that Mn_2O_3 particles with a diameter of 0.8 µm or bigger have the same atomic fraction as the bulk sample. The resulting atomic fraction of particles smaller than 0.4 µm changes dramatically compared to the bulk sample.

Comparing *Figure 6.16 and 6.17* it can be quoted that by lowering the beam energy, the interaction volume gets smaller, resulting in a more accurate analyzation of smaller particles. For an Al_2O_3 particle a beam energy of 10 keV instead of 15 keV enables to measure particles with a diameter up to 0.7 µm compared to 1.5 µm more accurately.

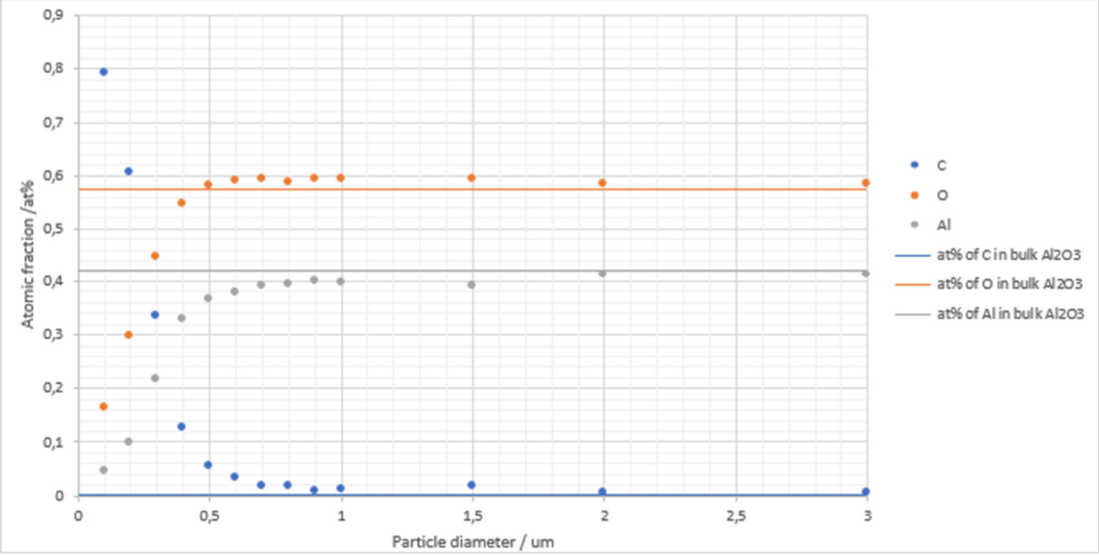

Figure 6.17: *Influence of the diameter of simulated spherical Al_2O_3 particles (on a carbon substrate) on the determined atomic fraction, compared to a bulk material of Al_2O_3; beam energy = 10 keV*

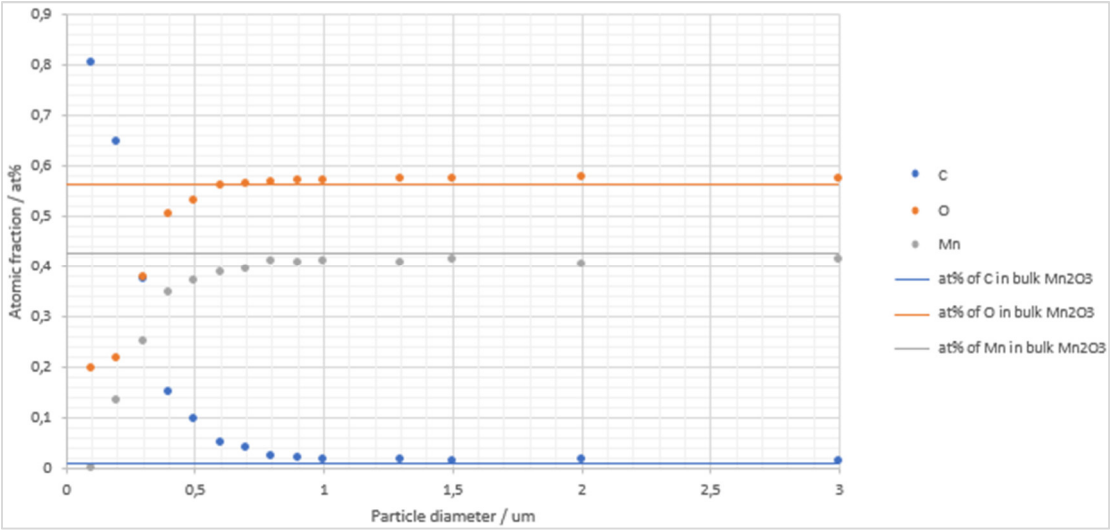

Figure 6.18: *Influence of the diameter of simulated spherical Mn_2O_3 particles (on a carbon substrate) on the determined atomic fraction, compared to a bulk material of Mn_2O_3; beam energy = 10 keV*

6.3 Results of the Particle Analysis

6.3.1 Measurement Details

Two samples of each Li-ion cell, which are prepared with the air-jetting sampling method, are analyzed. The samples are coated with a 10 nm thin carbon layer using EPA 100 (a high vacuum preparation tool developed by the Center for Electron Microscopy, Graz, in cooperation with the companies Leybold Heraeus, Germany, and Anton Paar GmbH, Austria). The coated samples are analyzed using the SEM Zeiss Sigma 300 VP equipped with EDX. The measurements were performed in high vacuum and with a beam energy of 10 keV.

First, for every experiment a minimum of 750 particles of each sample was analyzed with a fixed measurement time of 5 sec per particle using the software AZtec. These measurements were used for determining the size distribution. However, for a more accurate elemental composition further analysis of both samples of experiment 4 and one sample of each other experiment was performed with a minimum of 50 000 counts per particle.

6.3.2 Results

Figures 6.19 – 6.22 show the analyzed areas of one sample of each experiment.

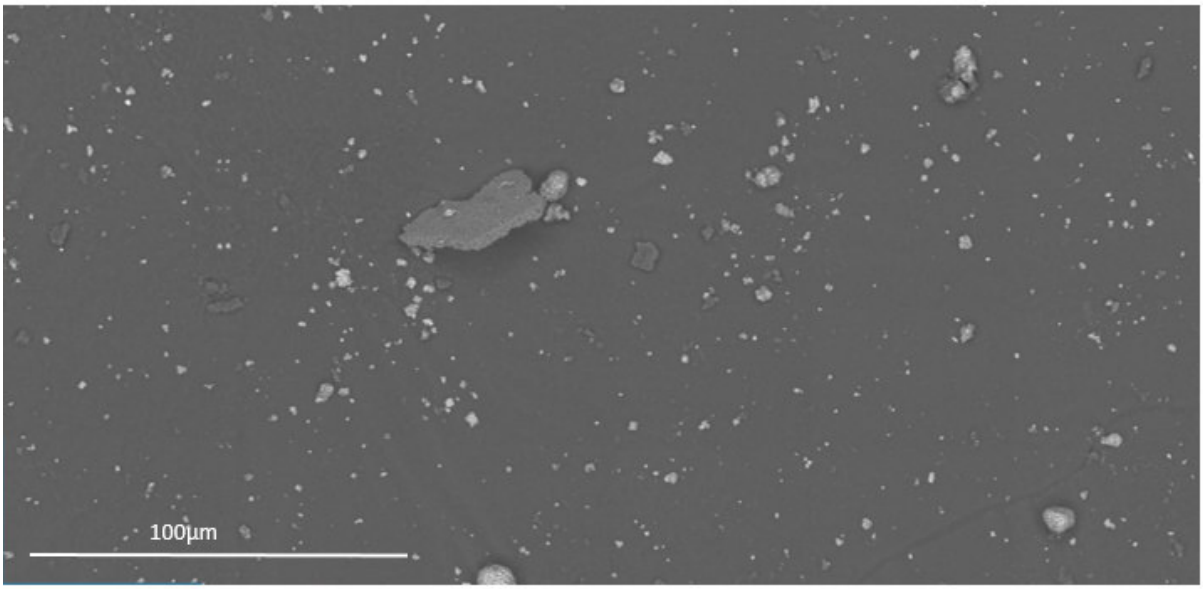

Figure 6.19: *Stitched BSE image of analyzed area of sample 2 of experiment 1*

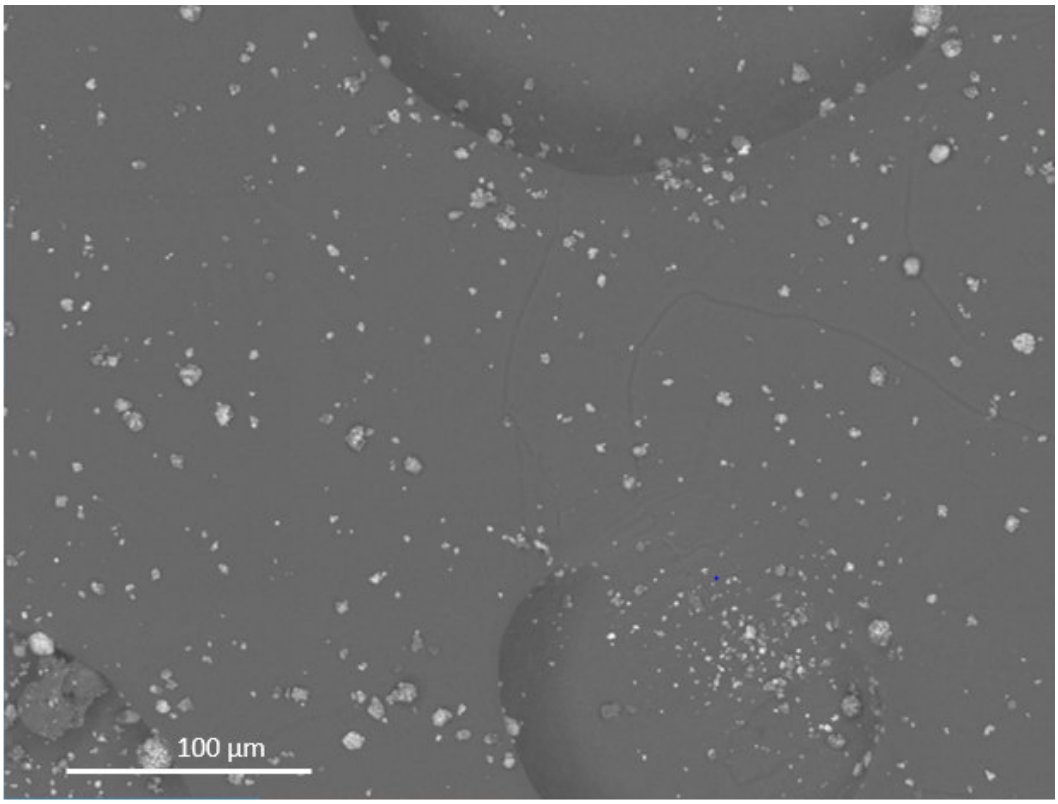

Figure 6.20: *Stitched BSE image of analyzed area of sample 1 of experiment 2*

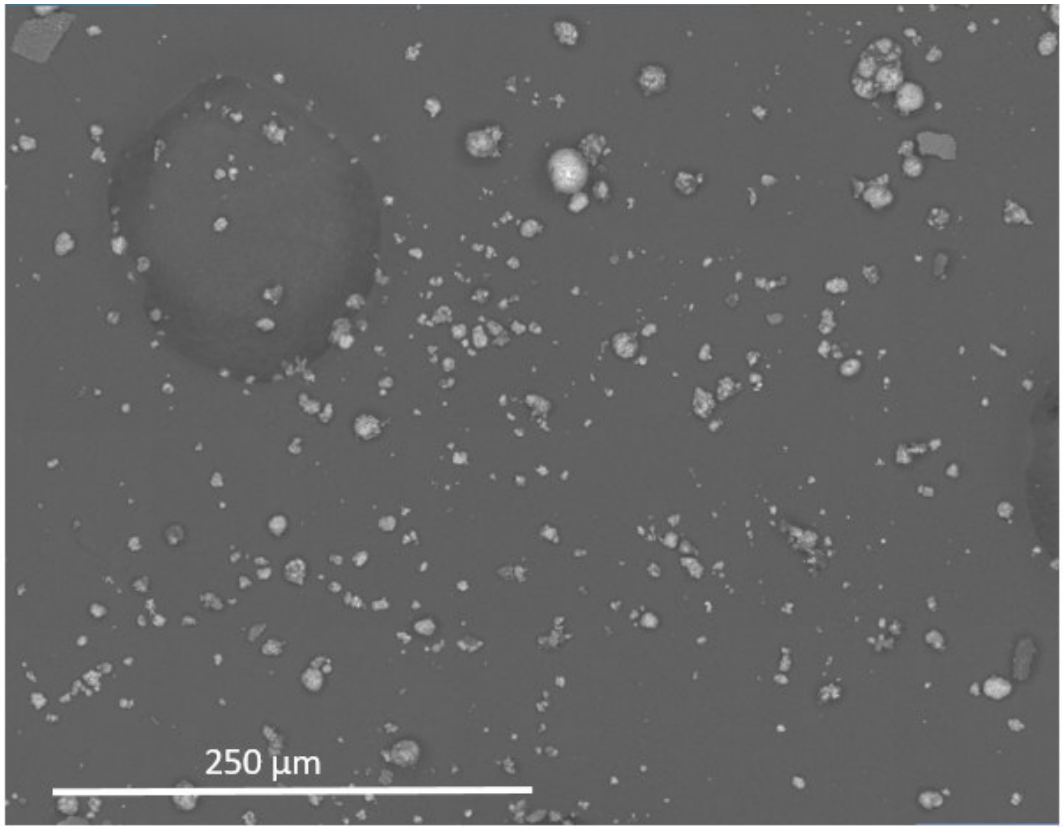

Figure 6.21: *Stitched BSE image of analyzed area of sample 2 of experiment 3*

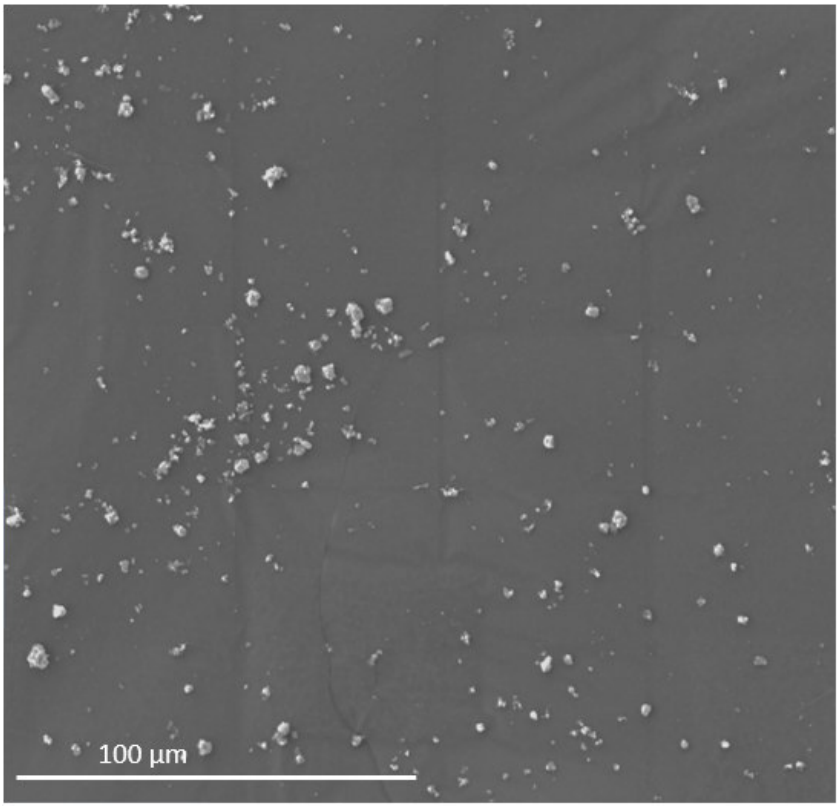

Figure 6.22: *Stitched BSE image of analyzed area of sample 2 of experiment 4*

Due to a similar chemical composition the analyzed particles can be divided into five classes:

- Class 1: Particles, which contain aluminum, but not more than 5 wt% of manganese, cobalt and nickel
- Class 2: Particles, which contain mainly manganese, cobalt and nickel
- Class 3: Particles, which contain more than 5 wt% of manganese, but not more than 5 wt% cobalt or nickel
- Class 4: Particle, which contain mainly carbon
- Class 5: Remaining particles, which do not fit to any of the other classes

Figure 6.28 – 6.39 compare the elemental compositions of class 1, class 2 and class 3 of one sample of each experiment. The figures show the weight fraction distribution of the elements within the particles. For each particle which contains the element a line is drawn at the scale according to the weight fraction. The elemental composition of all measured battery cells coincided well, although within a class there is a broad variation of the values. Likewise, the amount of particles of one class coincide quite well. In the appendix the elemental composition of both samples of experiment 4 are shown.

For the further analysis the relevant elements of each class are considered. For class 1 the relevant elements are aluminum and oxygen. Class 2 particles mainly consist of manganese,

cobalt, nickel and oxygen and class 3 particles of manganese and oxygen. A few particles consisting of Ca, Mg and Cl can be found. These particles may result from contaminations from handling with the battery or residual debris in the reactor.

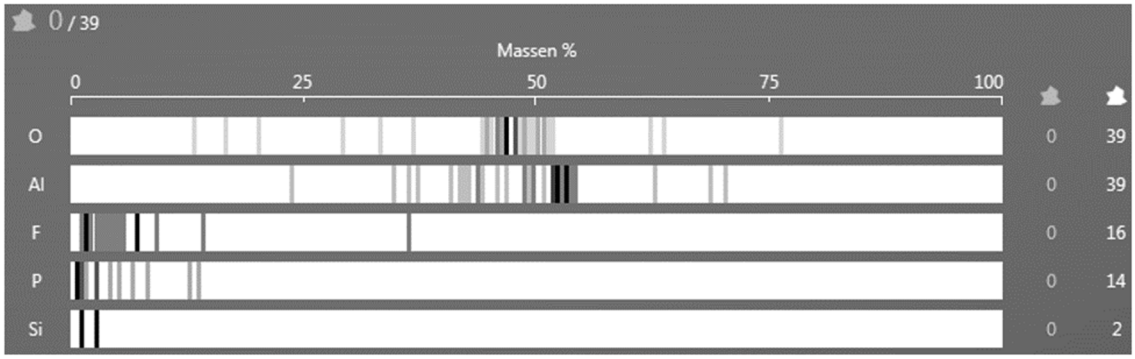

Figure 6.28: *Elemental composition of class 1 (experiment 1)*

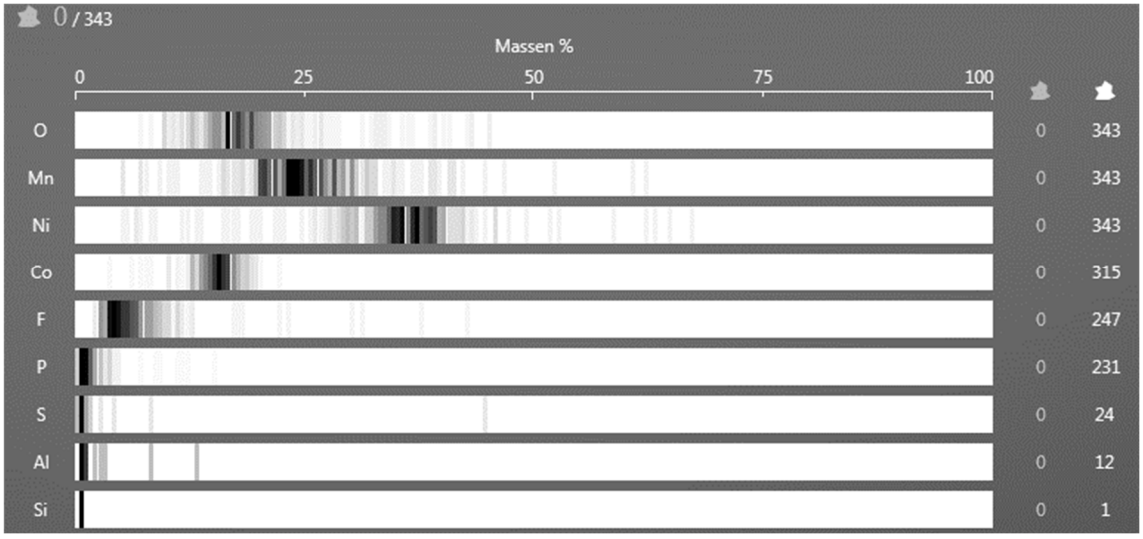

Figure 6.29: *Elemental composition of class 2 (experiment 1)*

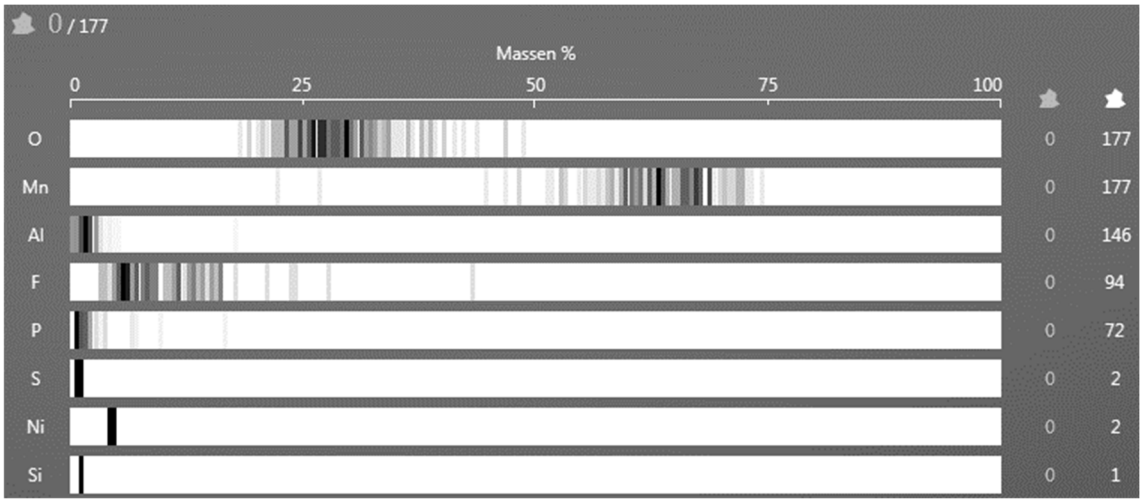

Figure 6.30: *Elemental composition of class 3 (experiment 1)*

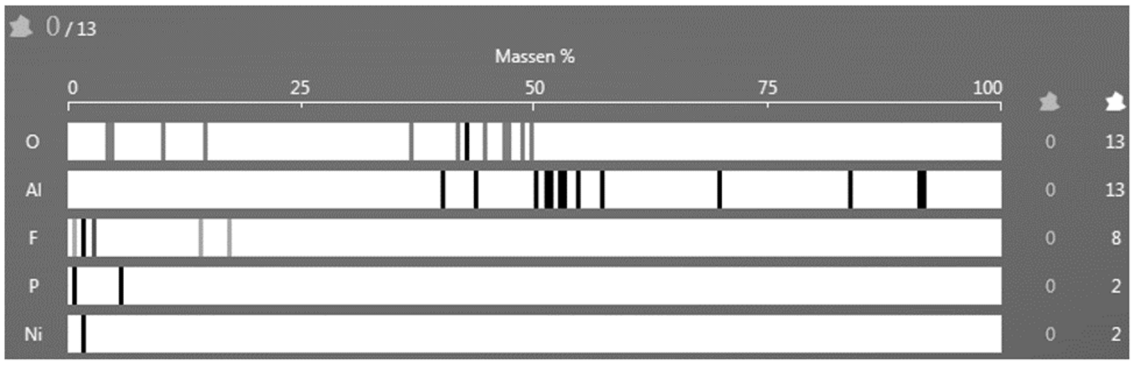

Figure 6.31: *Elemental composition of class 1 (experiment 2)*

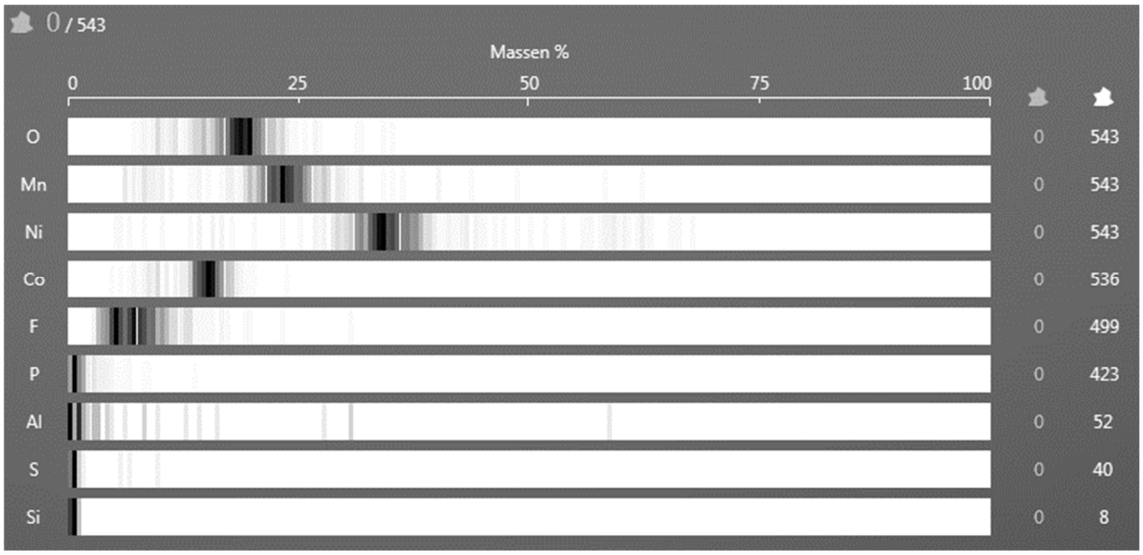

Figure 6.32: *Elemental composition of class 2 (experiment 2)*

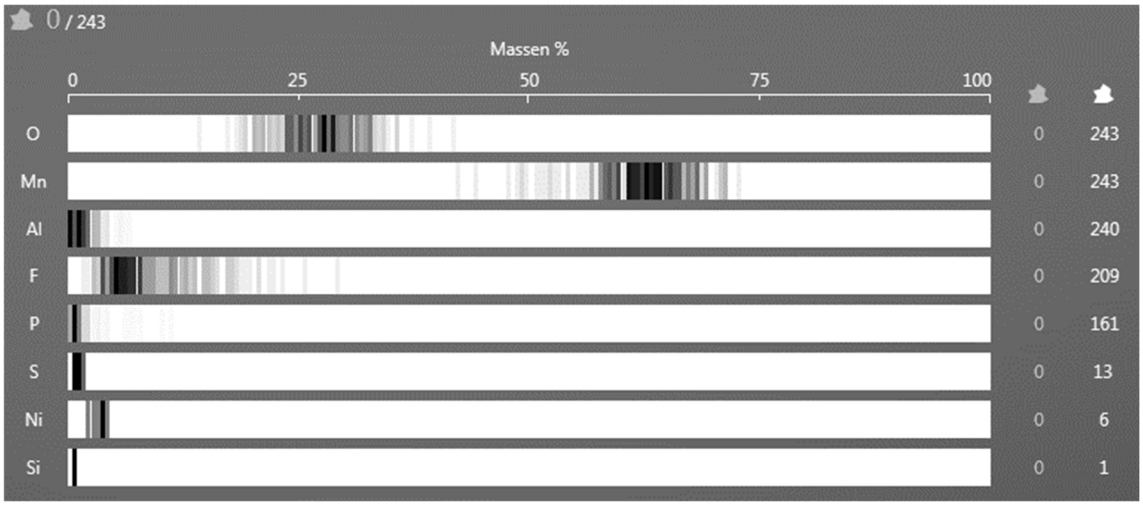

Figure 6.33: *Elemental composition of class 3 (experiment 2)*

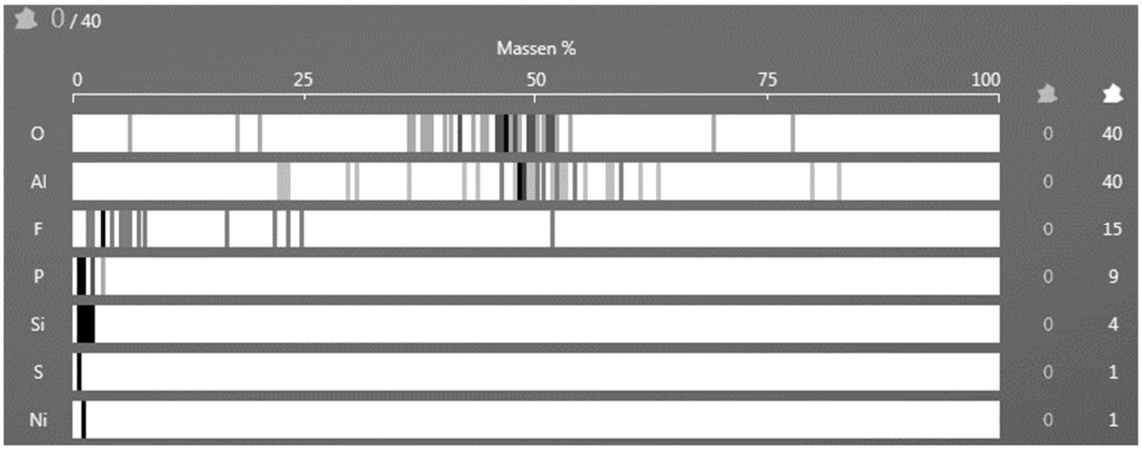

Figure 6.34: *Elemental composition of class 1 (experiment 3)*

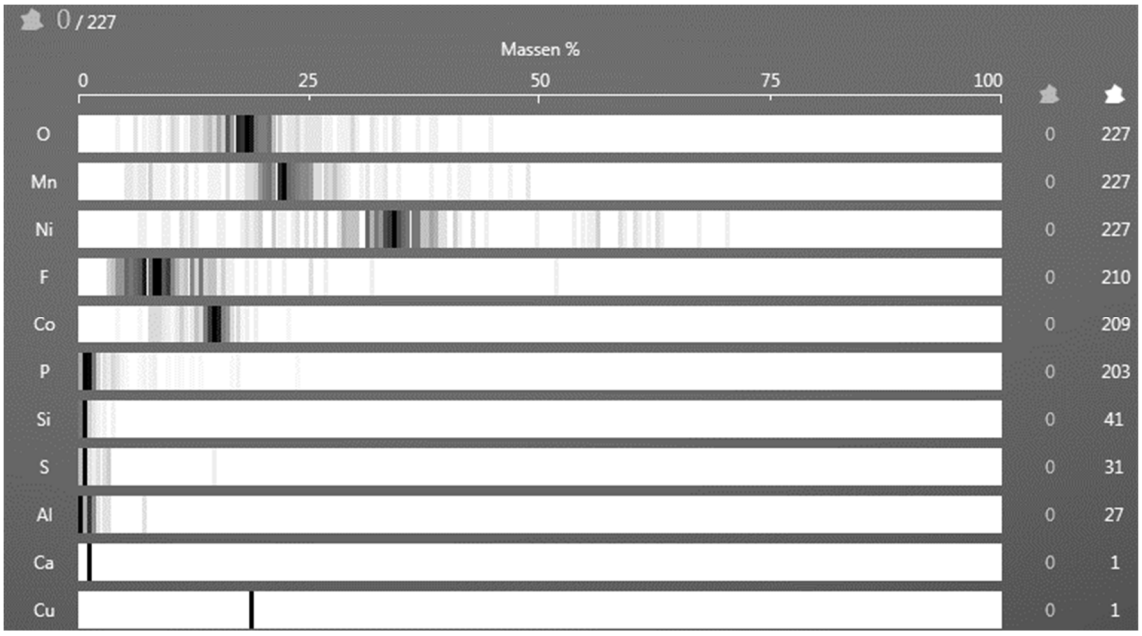

Figure 6.35: *Elemental composition of class 2 (experiment 3)*

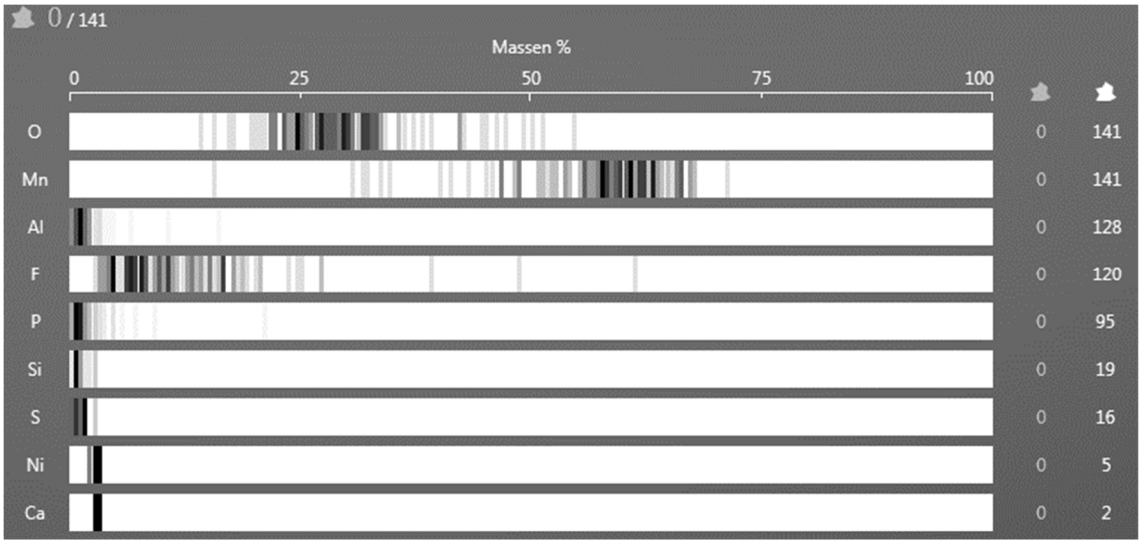

Figure 6.36: *Elemental composition of class 3 (experiment 3)*

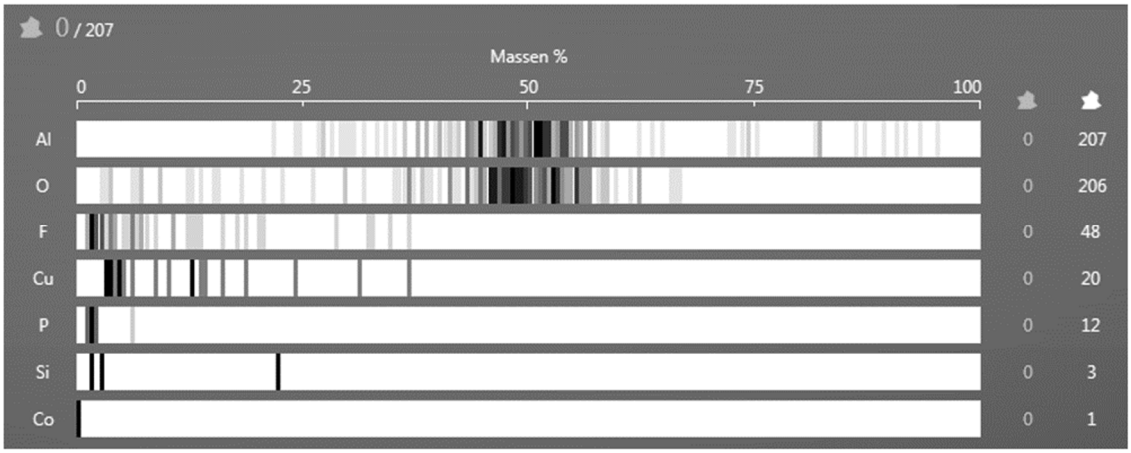

Figure 6.37: *Elemental composition of class 1 (experiment 4)*

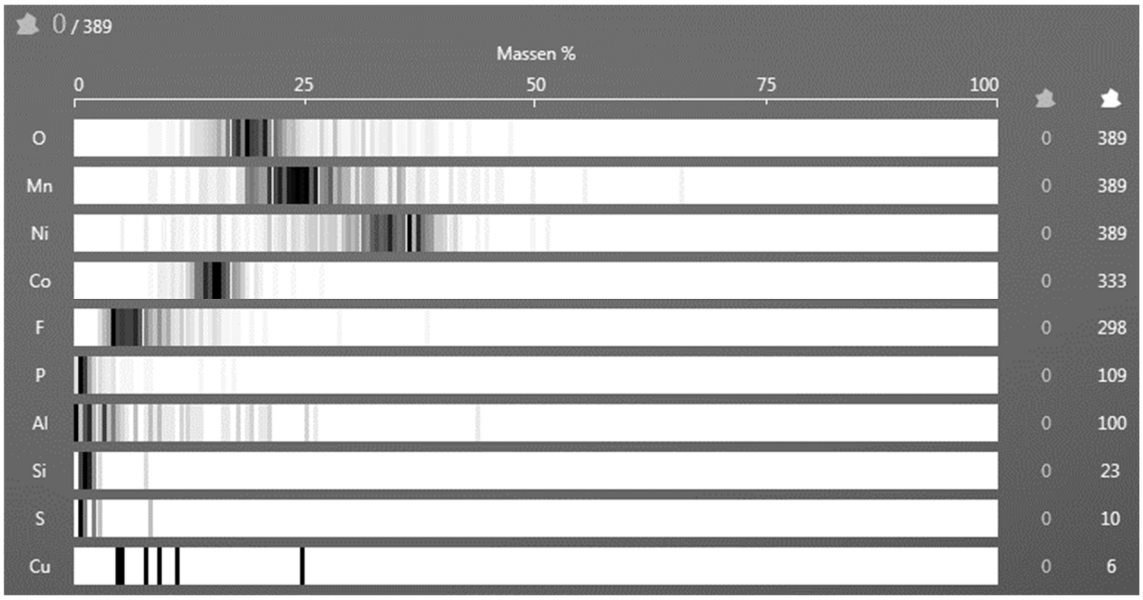

Figure 6.38: *Elemental composition of class 2 (experiment 4)*

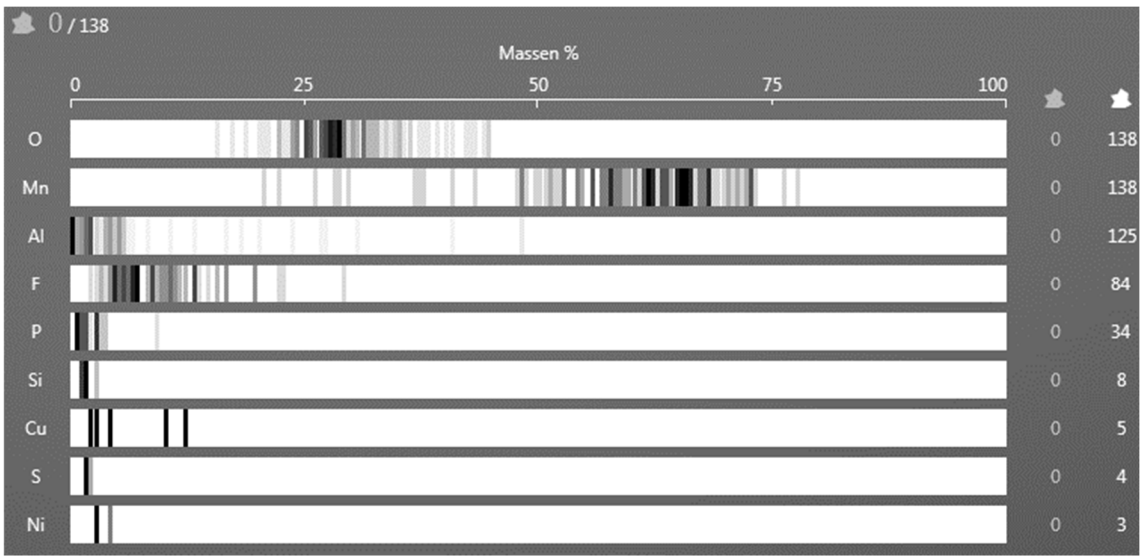

Figure 6.39: *Elemental composition of class 3 (experiment 4)*

In *Table 6.10* the fraction of class 1, class 2, class 3 and class 5 particles of the total number of particles is shown. Class 4 is not included since the particles of this class cannot be measured automatically. Particles of class 4 consist mainly of carbon, but a BSE image of the particles is mandatory for automatic determination. Therefore, the carbon particles cannot be distinguished from the carbon tape. The majority of the particles belongs to class 2, followed by class 3 particles. A smaller number of particles are classified in class 1 and only a few percentages are class 5 particles.

Table 6.10: *Fraction of class 1, class 2, class 3 and class 5 particles of the total number of particles in %*

	Experiment 1	**Experiment 2**	**Experiment 3**	**Experiment 4**
Fraction of class 1 in %	15.4	9.0	8.3	14.8
Fraction of class 2 in %	54.3	45.9	47.1	70.5
Fraction of class 3 in %	30.2	36.3	33.0	13.2
Fraction of class 5 in %	0.2	8.8	11.5	1.5

Beside the weight fraction of the elements of the particles, it is reasonable to consider the atomic fraction (see below). Weight percent (wt%) can be converted to atomic percent (at%) by *Equations 17 and 18:*

$$K = \frac{wt\%}{M} \tag{17}$$

$$at\% = \frac{K}{\sum K} \cdot 100 \tag{18}$$

with *K* the K value for every detected element, *M* the molar mass [g/mol].

Class 1:

In *Figure 6.40,* an SE image, a BSE image and an EDX-spectrum of a particle of class 1 is shown. The main elements are aluminum and oxygen.

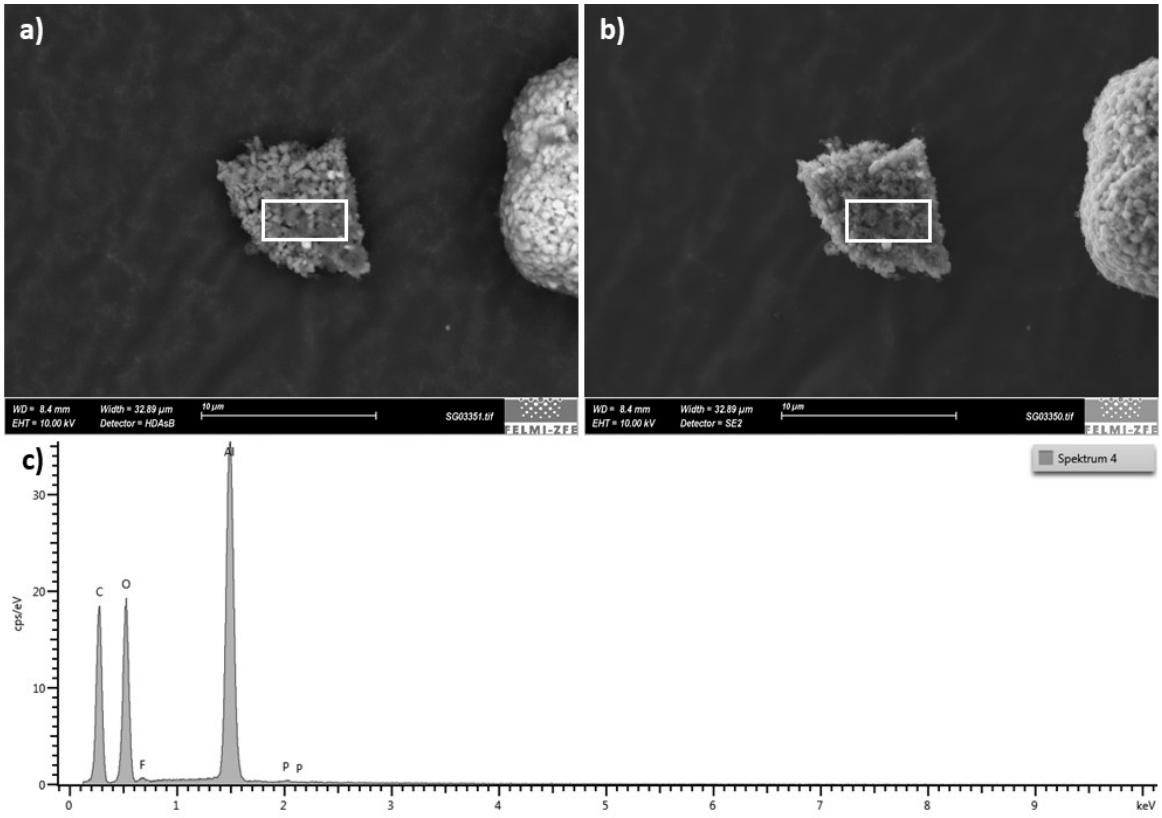

Figure 6.40: *a) SE image, b) BSE image and c) EDX spectrum of a particle of class 1 (measured in the marked area)*

Table 6.11 shows the size distribution of the particles of all tested Li-ion cells.

Table 6.11: *Size distribution of particles of class 1 of experiment 1, 2, 3 and 4; (Concerning the uncertainty of the values see the main text)*

	Amount of particle in %							
Area of particle/ µm²	**Experiment 1**		**Experiment 2**		**Experiment 3**		**Experiment 4**	
Sample	**1**	**2**	**1**	**2**	**1**	**2**	**1**	**2**
< 0.1	21.6	43.9	0.0	23.7	0.0	0.0	24.3	0.0
[0.1 - 0.2)	35.3	21.7	12.5	21.2	10.0	20.3	21.5	11.3
[0.2 - 0.5)	27.5	17.7	31.3	26.3	34.0	27.0	24.7	34.0
[0.5 - 0.8)	9.8	6.6	14.6	8.1	26.0	23.0	8.3	17.3
[0.8 – 1)	0.0	2.5	8.3	9.3	2.0	5.4	3.2	2.7
[1.0 - 2.0)	5.9	4.5	14.6	5.8	14.0	9.5	7.0	14.7
[2.0 - 5.0)	0.0	3.0	16.7	3.4	8.0	9.5	7.5	10.0
[5.0 - 10.0)	0.0	0.0	2.1	2.2	6.0	5.4	3.4	10.0
≥ 10.0	0.0	0.0	0.0	0.0	0.0	0.0	0.0	0.0

The size distributions of all experiments are very similar, except for sample 2 of experiment 1, where most of the particles are smaller than 0.2 µm². It has to be noted that there is an uncertainty in the data, which is typical for this method.[37] The reason is that the threshold cannot be set perfectly for a big amount of particles at once, and sometimes one particle is counted as several smaller particles (see Chapter 6.2.3.). However, most particles (about 70 %) are smaller than 1 µm². Only few percentages (up to 10 %) are between 5 µm² and 10 µm² and no particle is bigger than 10 µm².

The relevant elements of class 1 are aluminum (Al) and oxygen (O). The normalized weight fraction of aluminum and oxygen (i.e. calculation of aluminum and oxygen to 100 %) versus the area of the particles of class 1 of experiment 4 is shown in *Figure 6.41*.

Most of the particles have a weight fraction of aluminum of about 50%, but there are also some particles with a higher amount of aluminum. Aluminum can originate from the housing of the Li-ion cell (consisting of an aluminum polymer composite), or from the current collector of the cathode. For the particles from the housing the chemical formula Al_2O_3 (weight composition 52.9 wt% Al and 47.1 wt% O, atomic composition 40 at% Al and 60 at% O) can be assumed. The particles originating from the current collector may only oxidize at the surface, leading to higher amounts of aluminum, and a small amount of oxygen. Since the housing makes up a larger amount than the current collector, more particles originating from the housing (Al_2O_3) are expected, as confirmed in Figure 6.41.

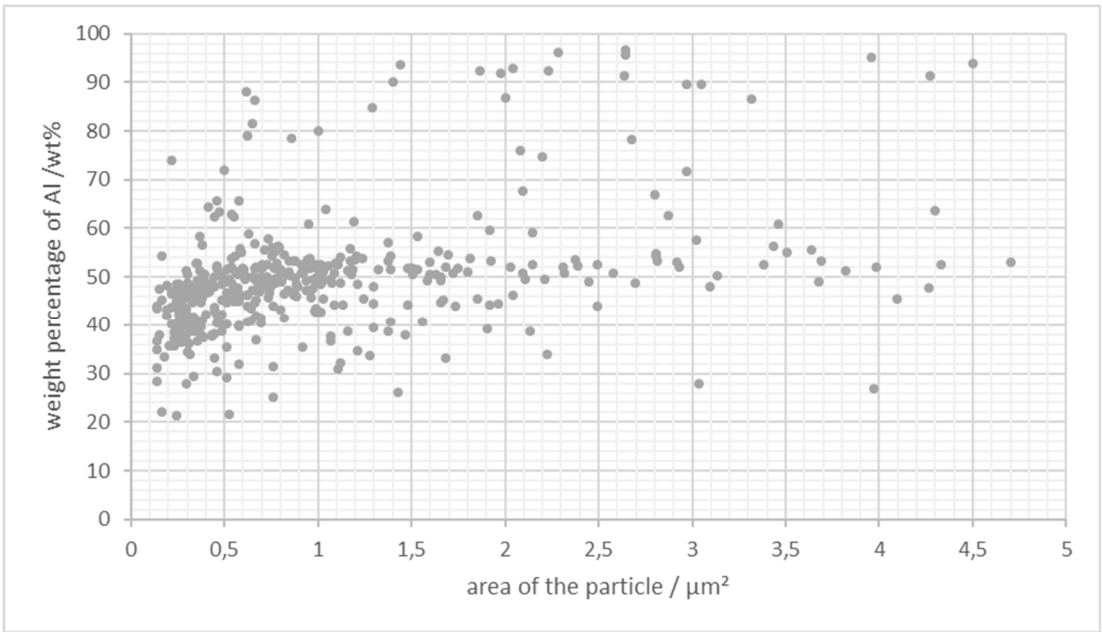

Figure 6.41: *Weight fraction of Al in wt% against the area of particle in µm²*

Class 2

An SE image, a BSE image and an EDX spectrum of a particle of class 2 is shown in *Figure 6.42*. The relevant elements of particles of class 2 are nickel, manganese, cobalt and oxygen.

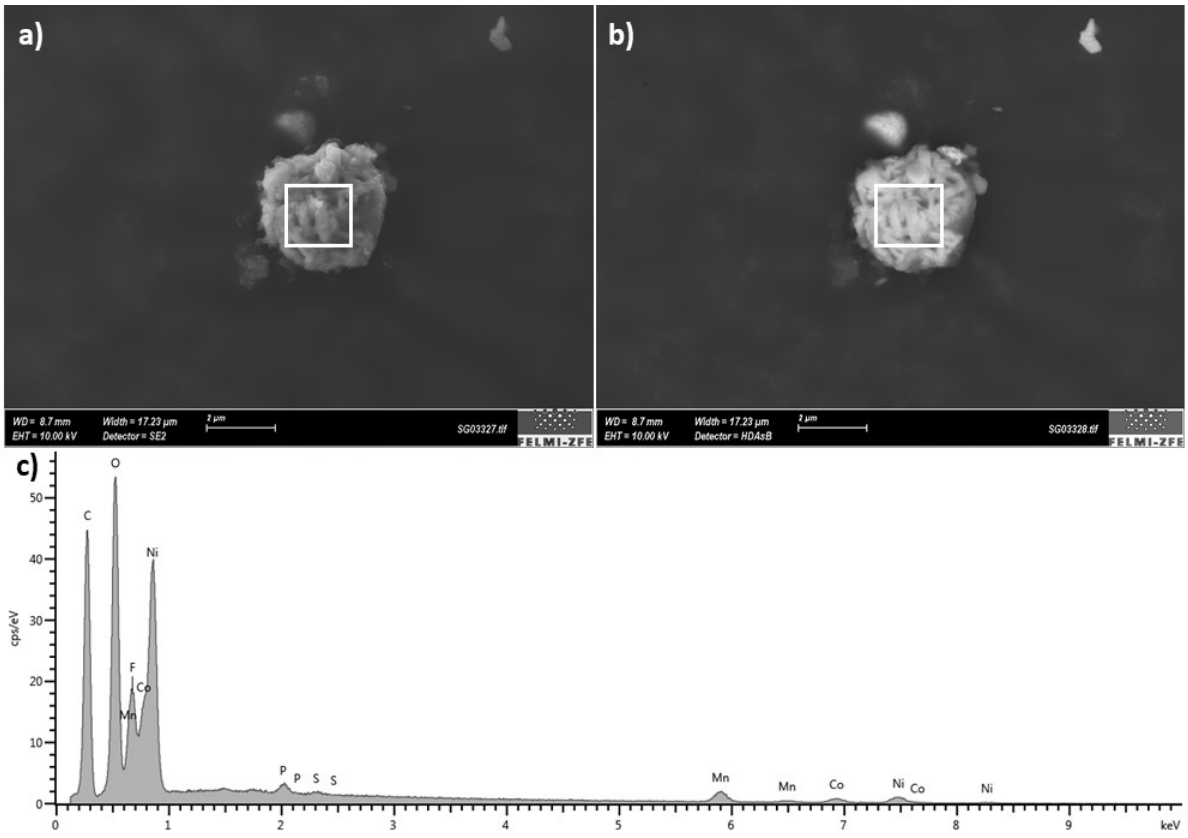

Figure 6.42: *a) SE image, b) BSE image and c) EDX spectrum of a particle of class 2 (measured in the marked area)*

The size distribution of class 2 concerning all experiments is shown in *Table 6.12.* The size distribution of the experiments varies due to the problem of setting the threshold (see Chapter 6.2.3). However, about the half of the particles is smaller than 1 µm² and the other half is between 1 µm² and 10 µm². Hardly any particle with an area bigger than 10 µm² can be found.

Table 6.12: *Size distribution of particles of class 2 of experiment 1, 2, 3 and 4; (Concerning the uncertainty of the values see the main text)*

	Amount of particle in %							
Area of particle/ µm²	**Experiment 1**		**Experiment 2**		**Experiment 3**		**Experiment 4**	
Sample	**1**	**2**	**1**	**2**	**1**	**2**	**1**	**2**
< 0.1	4.5	11.0	0.0	4.3	0.0	0.0	7.4	0.0
[0.1 - 0.2)	11.4	12.9	2.3	7.0	4.0	4.7	13.2	4.0
[0.2 - 0.5)	28.0	30.0	12.6	15.0	20.4	18.8	26.4	13.5
[0.5 - 0.8)	17.4	16.5	12.6	15.8	15.2	14.5	15.2	14.8
[0.8 – 1)	6.3	7.6	6.0	6.7	6.8	8.3	9.3	10.8
[1.0 - 2.0)	17.4	11.8	28.0	21.0	23.5	22.8	14.1	22.8
[2.0 - 5.0)	10.8	8.5	25.1	21.0	19.8	20.7	12.1	27.7
[5.0 - 10.0)	2.4	1.7	13.4	9.1	10.2	10.1	2.3	6.5
≥ 10.0	1.9	0.0	0.0	0.0	0.0	0.0	0.0	0.0

The relevant elements of class 2 are manganese, cobalt, nickel and oxygen. The weight fractions of these elements of experiment 4 are normalized and plotted against the particle area in *Figure 6.43*. It can be assumed that the chemical formula of the particles of class 2 is approximately $Ni_{0.45}Mn_{0.35}Co_{0.2}O$ (weight fraction: 36.0 wt% Ni, 26.2 wt% Mn, 16.0 wt% Co and 21.8 wt% O; atomic fraction: 22.5 at% Ni 17.5 at% Mn, 10 at% Co and 50 at% O). As can be seen in *Chapter 4.1* the cathode consists of manganese oxide and nickel-manganese-cobalt oxide. Therefore, the class 2 particles are assumed to originate from the cathode of the Li-ion cell.

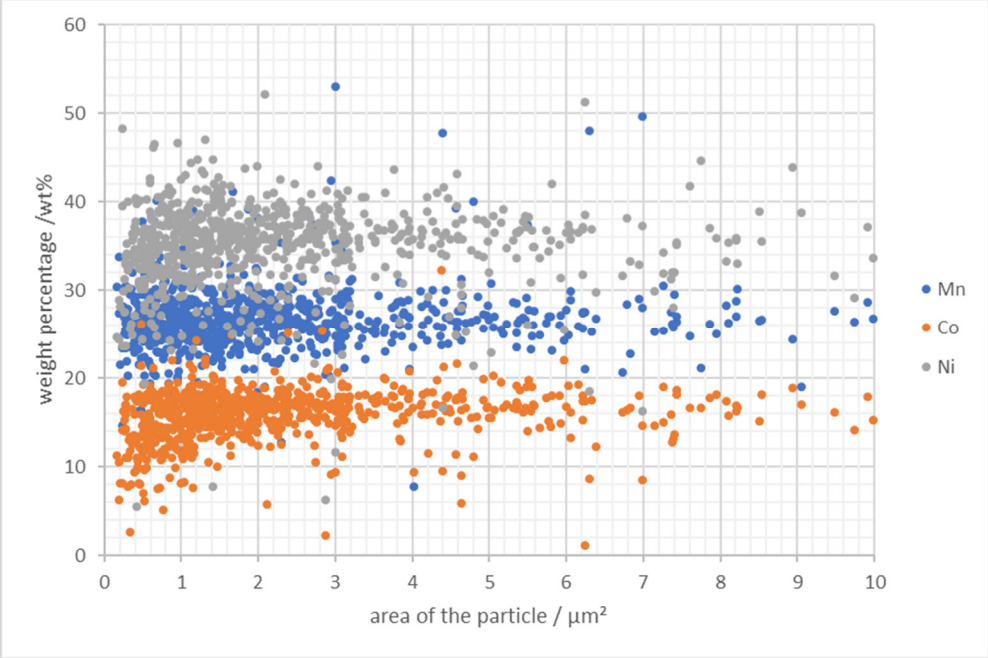

Figure 6.43: *Weight fraction of Mn, Co, Ni and O against area of particle of experiment 4*

Class 3:

Figure 6.44 shows the SE image, BSE image and the EDX spectrum of a particle of class 3. The relevant elements of particles of class 3 are manganese and oxygen.

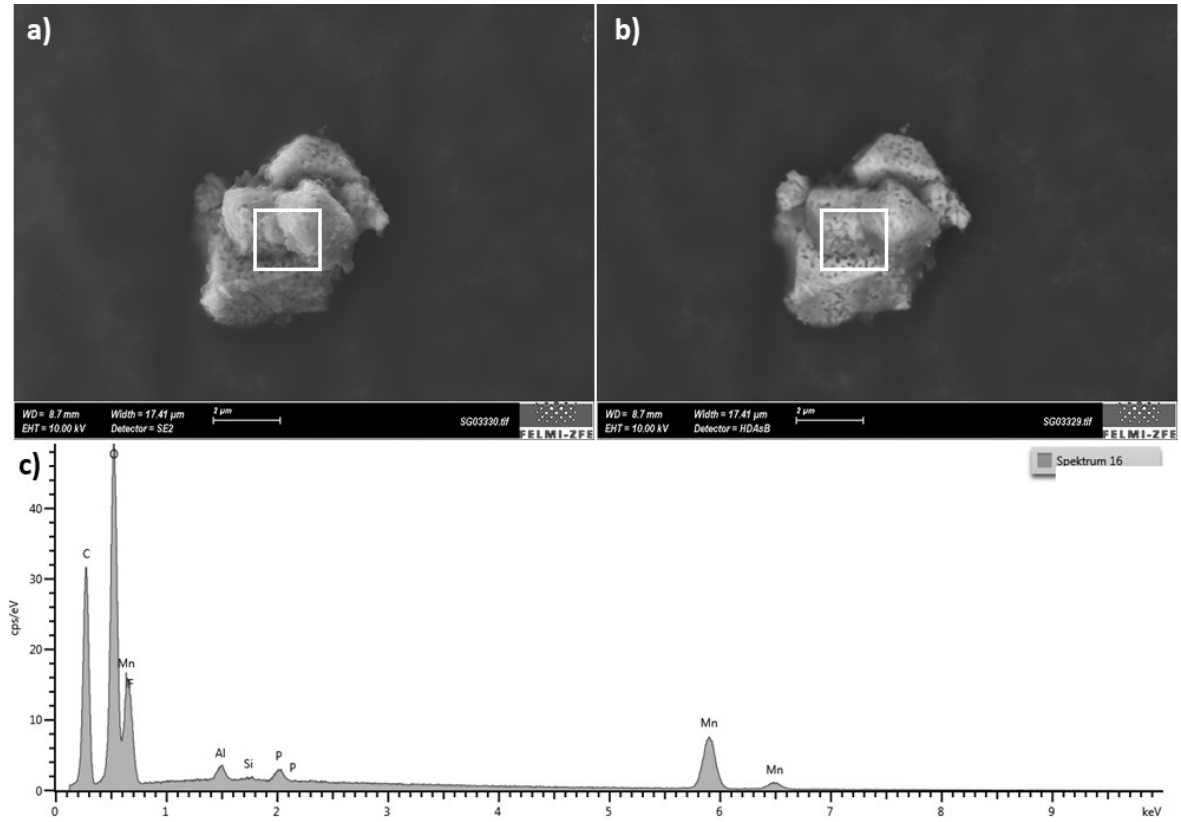

Figure 6.44: *a) SE image, b) BSE image and c) EDX spectrum of a particle of class 3 (measured in the marked area)*

The size distributions and the fractions of class 3 particles of all experiments are shown in *Table 6.13*. About 35 – 50 % of the particles are smaller than 1 µm² and approximately 40 – 55 % are between 1 µm² and 5 µm². About 1 - 25 % of the particles have an area between 5 µm² and 10 µm² and no particle is bigger than 10 µm².

Table 6.13: *Size distribution of particles of class 3 of experiment 1, 2, 3 and 4; ;(Concerning the uncertainty of the values see the main text)*

	Amount of particle in %							
Area of particle/ µm²	**Experiment 1**		**Experiment 2**		**Experiment 3**		**Experiment 4**	
Sample	**1**	**2**	**1**	**2**	**1**	**2**	**1**	**2**
< 0.1	4.6	9.2	0.0	5.3	0.0	0.0	7.3	0.0
[0.1 - 0.2)	7.7	9.2	1.8	7.2	3.2	6.9	8.1	1.8
[0.2 - 0.5)	17.6	17.4	6.3	9.3	15.3	15.2	16.7	9.5
[0.5 - 0.8)	11.5	14.0	5.4	7.6	9.6	8.3	16.6	11.2
[0.8 – 1)	4.2	5.3	3.6	5.5	6.1	5.1	4.7	5.3
[1.0 - 2.0)	23.4	19.3	17.9	17.5	19.8	18.0	23.0	27.8
[2.0 - 5.0)	21.5	24.2	38.6	29.5	31.6	25.3	16.7	32.5
[5.0 - 10.0)	9.6	1.4	26.5	18.1	14.4	21.2	6.8	11.8
≥ 10.0	0.0	0.0	0.0	0.0	0.0	0.0	0.0	0.0

The normalized weight fraction of the relevant elements of class 3 (manganese, oxygen) are shown in *Figure 6.45*. The chemical formula Mn_2O_3 (weight fraction of 69.6 wt% Mn and 30.4 wt% O; atomic fraction of 40 at% Mn and 60 at% O) for the particle of this class can be estimated. As can be seen in Chapter 4.1 the cathode consists of manganese oxide and nickel-manganese-cobalt oxide. Therefore, the class 3 particles are assumed to originate from the cathode of the Li-ion cell.

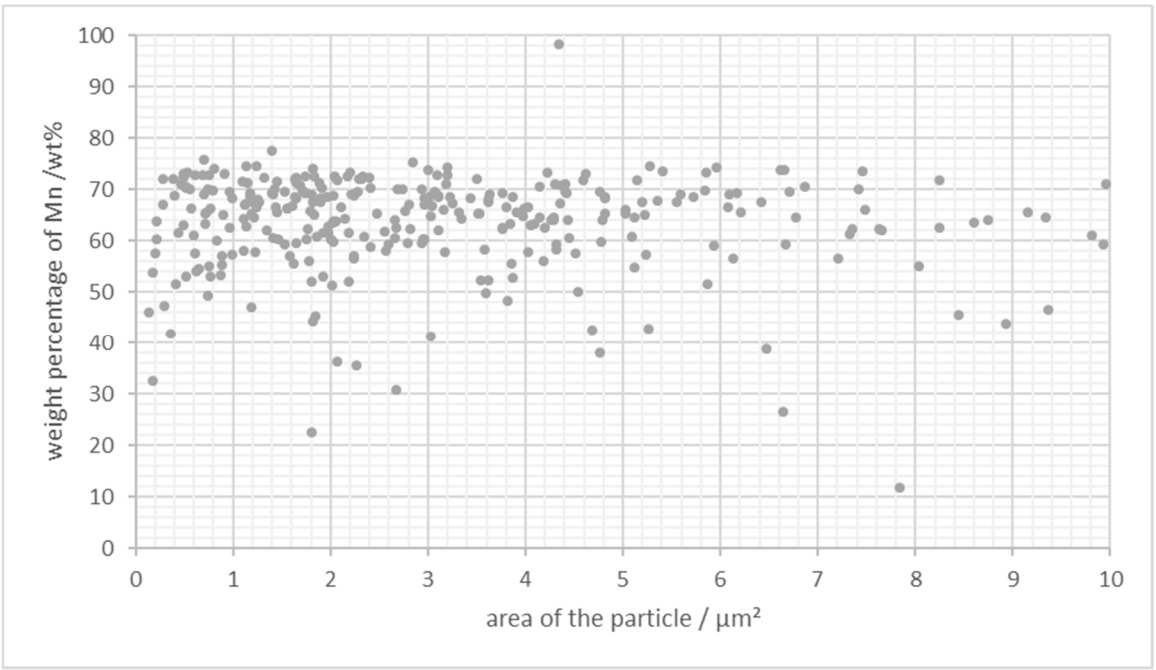

Figure 6.45: *Weight fraction of Mn in wt% against area of particle in µm² of experiment 4*

Class 4:

Class 4 particles contain mainly carbon. Since a BSE image (shows the material contrast) of the particles is used for automatic determination, the carbon particles cannot be distinguished from the carbon tape. To get an idea of the elemental composition and the size of the particles, 28 particles are analyzed individually, and a size determination is created using the software Fiji[36].

In *Figure 6.46* an SE image, a BSE image and an EDX spectrum of a particle of class 4 is shown.

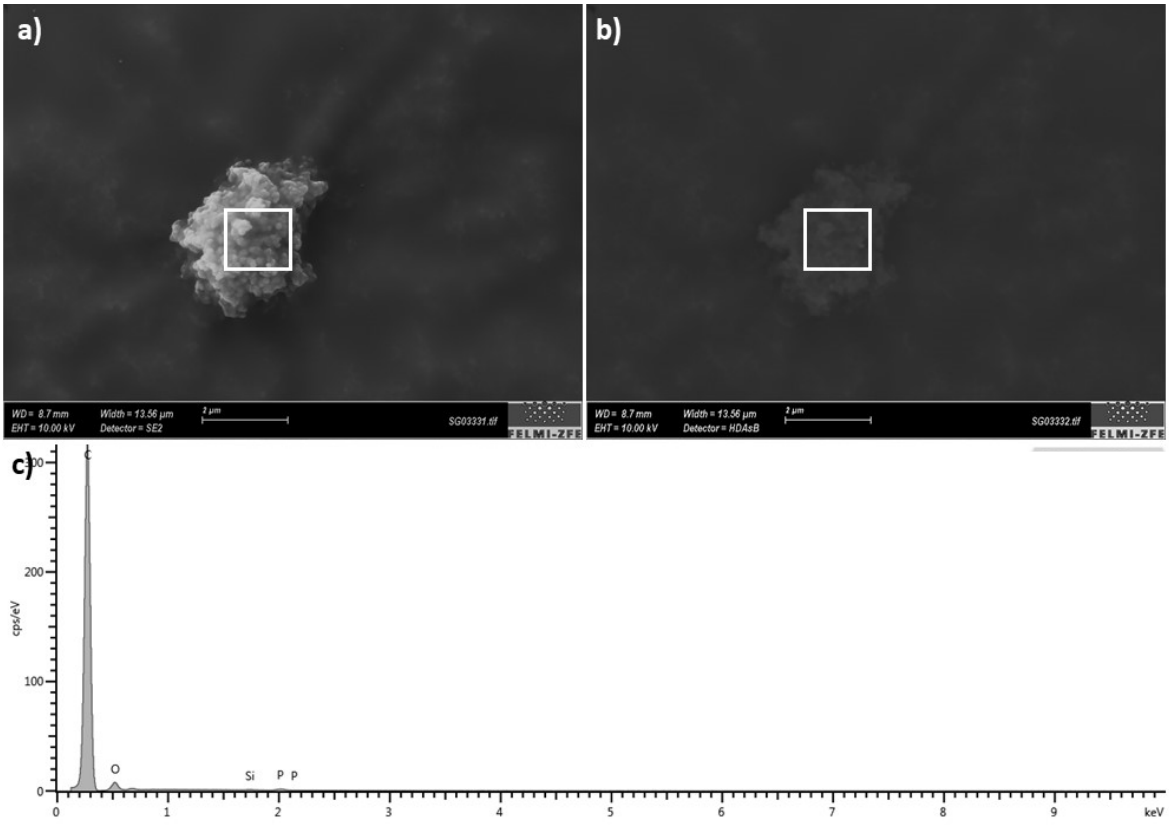

Figure 6.46: *a) SE image, b) BSE image and c) EDX-spectrum of a particle of class 4 (measured in the marked area)*

Table 6.14 presents the size distribution of the particles of class 4. The particles consist in average of carbon and oxygen. The majority of the particles is smaller than 10 µm. As can be seen in *Chapter 4.1* the anode consists of graphite. Therefore, the class 4 particles are assumed to origin from the anode of the Li-ion cell.

Table 6.14: *Size distribution of particles of class 4*

Particle area in µm²	Amount of particles in %
< 0.2	3.6
[0.2 - 0.5)	7.1
[0.5 - 0.8)	7.1
[0.8 – 1)	7.1
[1.0 - 2.0)	10.7
[2.0 - 5.0)	17.9
[5.0 - 10.0)	25.0
≥ 10	21.4

Class 5:

Class 5 contains all particles, which do not fit to any of the other classes. This includes for example agglomerates of the two or more particles of the other classes, where the individual particles cannot be distinguished, and a mixture of both classes is measured. Additionally, this class contains particles with a high mass percentage of fluorine. However, no statistically relevant statement can be made from these data, because of the small number of particles.

Figure 6.47 shows an SE and a BSE image of an agglomerate of different classes. In the BSE image the brightness of the grey level of different areas is based on the elemental composition (material contrast). In the BSE image it can be seen, that different kinds of particles stick on a main particle. The main particle belongs to class 1 (see *Figure 6.48*), whereas the particles on the main particle belong to class 2 (see *Figure 6.49*).

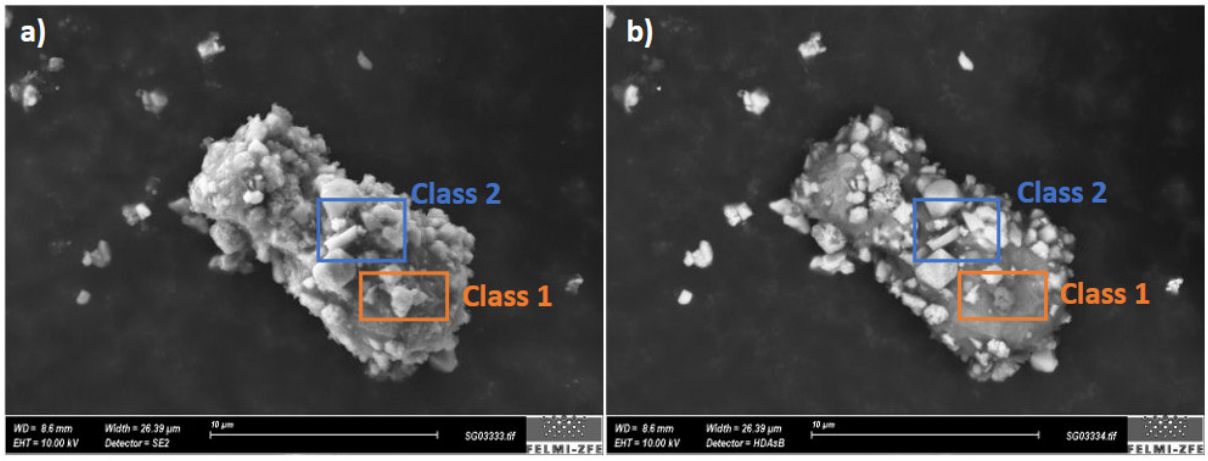

Figure 6.47: *a) SE image and b) BSE image of a particle of class 5*

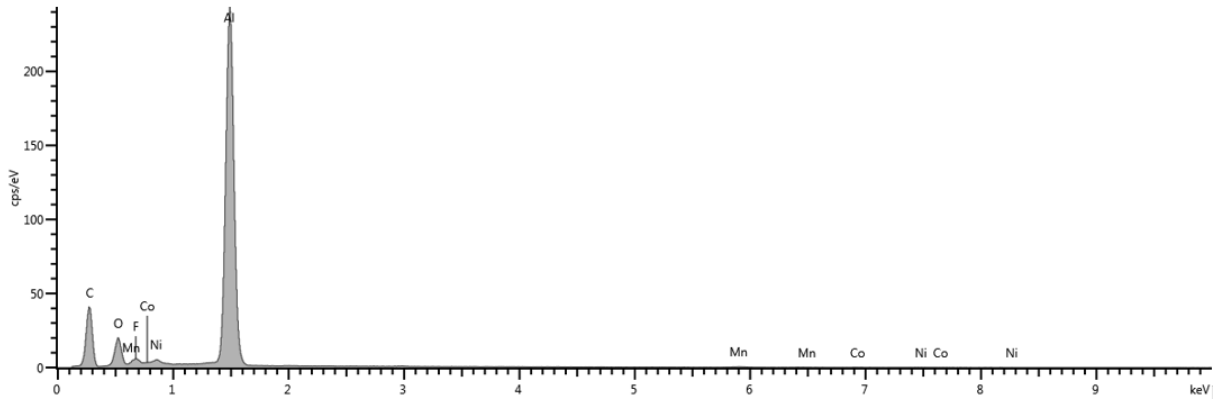

Figure 6.48: *EDX-spectrum measured in the area marked "class 1" in Figure 6.47*

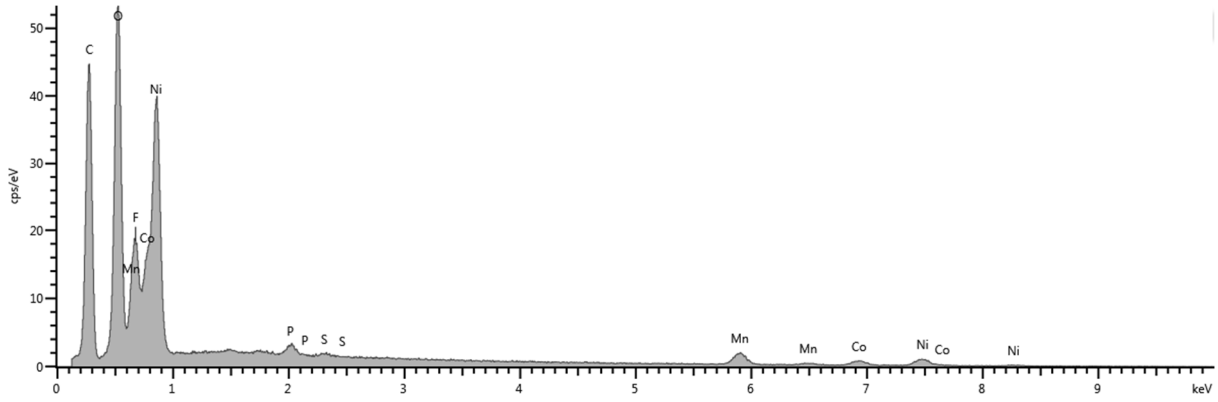

Figure 6.49: *EDX-spectrum of area marked "class 2" in Figure 6.47*

6.4 Discussion of the Particle Analysis

The particles were analyzed using scanning electron microscopy combined with energy dispersive X-ray spectroscopy. This method enables a good estimation of the size distribution of a sample as well as the elemental composition. However, several challenges are encountered in the SEM/EDX analysis of the particles, as summarized in the following paragraphs.

One challenge concerning automated analysis is that the particles have to be well-separated. Therefore, an appropriate sampling method had to be found. In this work, the method of choice was the "air jetting" method, allowing to analyze the particles individually. This method uses a jet of air to apply the particles on an adhesive carbon tape. The criterion was the distinctness of particles for automated analysis. Further measurements are recommended to asses in a statistically relevant manner, whether the remaining particles are representative for the basic set of material. However, the choice of air jetting in the thesis was the definition of a reproducible well-defined handling as it is typical for analytical chemistry.

Various simulations were performed to find the electron beam energy which generates the smallest possible interaction volume and even allows to quantify all expected elements.

Additionally, a particle standard was measured to show the size and beam energy dependence of the determined elemental composition of the particles. The smaller the particle is, the more imprecise gets the quantification. The particle should be bigger than the interaction volume of the electron in the material. This can be achieved by lowering the beam energy.

Further difficulties arise due to the use of the adhesive carbon tape as a substrate. The particles of class 4, which mainly consist of carbon, cannot be analyzed automatically, since BSE imaging has to be performed for the analysis. Therefore, hardly any material contrast is found between the carbon rich particles and the carbon tape. Thus, they cannot be sufficiently distinguished. Furthermore, a non-negligible amount of oxygen was found via EDX analysis of the pure carbon tape, eventually complicating quantifications. Additionally, when using a carbon tape as a substrate, pits arise under vacuum. Although they are assessed to have a subordinate influence on the investigation, it would be an improvement to use a carbon substrate, which is smooth and free from other chemical elements.

The determination of the size distribution by a binary image created by a threshold can be tricky, especially when the sample consists of inhomogeneous particles with different material contrast. In this thesis the influence of several operators on the result was shown, verifying the uncertainty resulting from the interaction between operator and computer. However, the obtained values of the particle size give a realistic estimation of the size of the particles after thermal runaway and help to assess the health relevance.

Concerning the elemental composition, the analyzed particles of the Li-ion cell can be divided into five classes: particles, which contain mainly aluminum and oxygen; particles, which mainly contain nickel, manganese, cobalt and oxygen; particles, which mainly contain manganese and oxygen; particles, which mainly contain carbon and oxygen; a smaller fraction of particles, which do not fit to any of the other classes, for example because they are agglomerates of particles of more than one class.

In summary, almost all particles are smaller than 10 µm² (corresponds roughly to a diameter smaller than 4 µm). This may lead to health risks, since particles with a diameter smaller than 10 µm can be inhaled deeply into the lungs[39]. Additional to the size of the particles also the elemental composition of the particles is relevant. Especially, the nickel-manganese-cobalt particles are problematic, since nickel and its compounds are classified as a carcinogenic working material.[40] Additionally, there may be organic, hazardous compounds which cannot be

analyzed by EDX. To achieve chemical information about such compounds for instance Raman spectroscopy could be used.

Recently FELMI-ZFE built up the system RISE (Raman Imaging and Scanning Electron microscopy) where one region of a surface can be imaged with SEM resolution and after a move of the specimen stage it can be analyzed by a Raman microscope for chemical analysis. This new correlative microscopic method, which is also combined with EDX at this setup, may be a further step of investigating particles resulting from thermal runway.

7. Conclusions

In this Master's thesis, gases and particles released from Li-ion cells during thermal runaway are characterized. Four thermal runaway experiments with the same type of battery cell were performed in a reactor.

The composition and concentration of the generated gas were determined using gas chromatography (GC) and Fourier transformation infrared (FTIR) spectroscopy. Depending on the type and amount of gas, either GC or FTIR provided more accurate results. The gas chromatograph was calibrated with different test gases of known composition, to allow a more precise measurement. The main compounds of the gas released from the Li-ion cell during thermal runaway are carbon dioxide (CO_2) and hydrogen (H_2). Further, higher amounts of carbon monoxide (CO) and water (H_2O) are found. Only few percentages of oxygen (O_2), acetylene (C_2H_2), ethylene (C_2H_4), ethane (C_2H_6), methane (CH_4), diethyl carbonate (DEC), ethyl methyl carbonate (EMC) and butane (C_4H_{10}) are found in the gas. Although, no hydrogen fluoride (HF) could be detected, it is expected to be released by the cell and to undergo further reactions with the materials inside the reactor. The released gas from the cell during thermal runaway is hazardous. The high amount of carbon monoxide is dangerous, since carbon monoxide is toxic and extremely flammable, like nearly all other mentioned gases.

The particles generated during thermal runaway were analyzed for their size distribution and their elemental composition using a scanning electron microscope (SEM) combined with a detector for energy dispersive X-ray spectroscopy and the software AZtec and Fiji. Introductory Monte Carlo simulations were performed, to estimate the interaction of the electron beam with the sample, using the software NIST DTSA-II.

Concerning the sampling of the particles, it was found that a method based on air jetting provides the most suitable specimens with well separated individual particles. In this method, particles are collected in the reactor after the thermal runaway experiment using a spatula and afterwards, they are fixed on an adhesive carbon tape by using a jet of air.

The collected particles were first analyzed in several pretest SEM experiments, in order to understand the difficulties of particle analysis and to find the best approach for obtaining most accurate results. In this respect, the influence of particle size and beam energy was simulated. Additionally, a particle standard with known elemental composition was measured. With decreasing particle size, the quantification of the chemical composition of the particles gets

more imprecise. It was shown that lowering the beam energy can lead to a more accurate determination.

The particles released from the Li-ion cell at thermal runaway can be classified into five main groups: particles, which contain mainly aluminum and oxygen; particles, which mainly contain nickel, manganese, cobalt and oxygen; particles, which mainly contain manganese and oxygen; particles, which mainly contain carbon and oxygen; particles, which do not fit to any of the other classes, for example because they are agglomerates of more than one class.

The manganese oxide and the nickel manganese cobalt oxide particles result from the cathode and the carbon particles originate from the anode of the Li-ion cell. The aluminum oxide particles may come from the housing of the cell. Overall, most of the particles have a smaller diameter than 10 µm and more than the half of the particles are smaller than 2 µm. Particles with a diameter smaller than 10 µm can be inhaled deeply into the lungs. Particles smaller than 2.5 µm can even reach the pulmonary alveoli. These fine particles can lead to negative health effects, depending on their chemical composition. Especially, the nickel-manganese-cobalt-oxide particles can be classified as carcinogenic.

In summary, SEM/EDX analysis gave a good assessment of the size distribution and the elemental composition of the particles, which are released from the Li-ion batteries during thermal runaway. However, it has to be mentioned that the SEM analysis of inhomogeneous particles with a diameter smaller than a few micrometers is highly challenging and several effects hinder a more precise analysis of such particles. Further methods for analyzing the particles released of the Li-ion cell at thermal runaway could be laser diffraction analysis, X-ray crystallography and Raman spectroscopy. Laser diffraction analysis is a method to analyze the particle size distribution and form. The particles are investigated by determining the diffraction angle of a laser. X-ray crystallography can be used to analyze the crystal structure and phase. It is based on diffraction of X-rays after interacting with a crystalline sample. Raman spectroscopy is a vibrational spectroscopic method. Due to the molecular vibrations, chemical compositions of the material can be measured. Combining particle SEM analysis with these methods might help to obtain a deeper understanding of the particles formed upon thermal runaway in the future. Recently the FELMI-ZFE built up a combined system of SEM, Raman spectroscopy (RISE: Raman Imaging and Scanning Electron microscopy) and EDX. Especially concerning the carbon rich particles, RISE could be an obvious next step of investigation.

8. References

1. Kley F, Lerch C, Dallinger D. New business models for electric cars-A holistic approach. Energy Policy. 2011;39(6):3392-3403. doi:10.1016/j.enpol.2011.03.036

2. Umweltbundesamt. Klimawandel. http://www.umweltbundesamt.at/umweltsituation/klima/klimawandel/. Accessed November 4, 2018.

3. Energiefonds K, Zukunft V-M mit. Faktencheck E-Mobilität. https://faktencheck-energiewende.at/wp-content/uploads/sites/4/FC_Mob18_gross_Web.pdf. Published 2018.

4. Gerssen-Gondelach SJ, Faaij APC. Performance of batteries for electric vehicles on short and longer term. J Power Sources. 2012;212:111-129. doi:10.1016/j.jpowsour.2012.03.085

5. Lisbona D, Snee T. A review of hazards associated with primary lithium and lithium-ion batteries. Process Saf Environ Prot. 2011;89(6):434-442. doi:10.1016/J.PSEP.2011.06.022

6. Feng X, Ouyang M, Liu X, Lu L, Xia Y, He X. Thermal runaway mechanism of lithium ion battery for electric vehicles: A review. Energy Storage Mater. 2018;10:246-267. doi:10.1016/J.ENSM.2017.05.013

7. Zhang ZJ, Ramadass P. Lithium-Ion Battery Systems and Technology. In: Brodd RJ, ed. Batteries for Sustainability: Selected Entries from the Encyclopedia of Sustainability Science and Technology. New York, NY: Springer New York; 2013:319-357. doi:10.1007/978-1-4614-5791-6_10

8. Golubkov AW, Scheikl S, Planteu R, et al. Thermal runaway of commercial 18650 Li-ion batteries with LFP and NCA cathodes - Impact of state of charge and overcharge. RSC Adv. 2015;5(70):57171-57186. doi:10.1039/c5ra05897j

9. Golubkov AW, Fuchs D, Wagner J, et al. Thermal-runaway experiments on consumer Li-ion batteries with metal-oxide and olivin-type cathodes. RSC Adv. 2014;4(7):3633-3642. doi:10.1039/c3ra45748f

10. Fernandes Y, Bry A, de Persis S. Identification and quantification of gases emitted during abuse tests by overcharge of a commercial Li-ion battery. J Power Sources. 2018;389:106-119. doi:10.1016/J.JPOWSOUR.2018.03.034

11. Korthauer R. Handbuch Lithium-Ionen- Batterien. Springer Vieweg; 2013. doi:10.1007/978-3-642-30653-2

12. Bottke P. Primäre Und Wiederaufladbare Lithium-Ionen-Batterien.; 2013.

13. Scott RPW. Principles and Practice of Chromatography.; 2003.

14. Agilent 3000 Mikro-GC Benutzerhandbuch.; 2008.

15. Sparkman OD, Penton Z, Kitson F. Gas Chromatography and Mass Spectrometry: A Practical Guide.; 2011.

16. Grob RL, Barry EE. Modern Practice of Gas Chromatography.; 2004.

17. Vickers AK. PLOT Column Selection. https://www.agilent.com/cs/library/eseminars/Public/PLOT Column Selection.pdf. Accessed August 31, 2018.

18. Ball DW. The Basics of Spectroscopy.; 2001.

19. Stokes DJ. Principles and Practice of Variable Pressure / Environmental Scanning Electron Principles and Practice of Variable Pressure / Environmental Scanning Electron Microscopy (VP-ESEM). (Rainforth M, ed.). John Wiley & Sons Ltd; 2008.

20. Goldstein, J., Newbury, D.E., Joy, D.C., Lyman, C.E., Echlin, P., Lifshin, E., Sawyer, L., Michael J. Scanning Electron Microscopy and Y-Ray Microanalysis. Third Edit.; 2003.

21. Dehm G, Howe JM, Zweck J. In-Situ Electron Microscopy: Applications in Physics, Chemistry and Materials Science. Wiley-VCH Verlag GmbH & Co. KGaA; 2012.

22. Periodicals W. CASINO V2 . 42 — A Fast and Easy-to-use Modeling Tool for Scanning Electron Microscopy and Microanalysis Users. 2007;29:92-101.

23. Ritchie NWM. NIST DTSA-II.

24. Echlin P. Handbook of Sample Preparation for Scanning Electron Microscopy and X-

Ray Microanalysis.; 2009.

25. Goldstein JI, Newbury DE, Michael JR, Ritchie NWM, Scott JHJ, Joy DC. Scanning Electron Microscopy and X-Ray Microanalysis. Fourth Edi.

26. SEM Sample Preparation Instructions. https://coefs.uncc.edu/hzhang3/files/2011/05/SEM-sample-preparation-instructions.pdf . Accessed July 6, 2018.

27. Fahlman BD. Materials Chemistry. Third Edit. Springer; 2018.

28. Huber ML, Harvey AH. CRC Handbook of Chemistry and Physics. 92nd ed.; 2011.

29. Scharner S. Quantitative safety characterization of Li-ion cells. Presented at the:

30. Wang Q, Ping P, Zhao X, Chu G, Sun J, Chen C. Thermal runaway caused fire and explosion of lithium ion battery. J Power Sources. 2012;208:210-224. doi:10.1016/J.JPOWSOUR.2012.02.038

31. Yang H, Zhuang G V., Ross PN. Thermal stability of LiPF6 salt and Li-ion battery electrolytes containing LiPF6. J Power Sources. 2006;161(1):573-579. doi:10.1016/J.JPOWSOUR.2006.03.058

32. Sicherheitsdatenblatt Kohlenmonoxid. https://produkte.linde-gas.at/sdb_konform/CO_10021698DE.pdf. Accessed February 22, 2019.

33. Sicherheitsdatenblatt Wasserstoff. https://produkte.linde-gas.at/sdb_konform/H2_10021694DE.pdf. Accessed February 22, 2019.

34. HMW Hauner Online Katalog. https://www.hmw-hauner.de/online-katalog/Titan.html . Accessed July 9, 2018.

35. Air Power. https://www.green-clean.at/fileadmin/user_upload/tx_pfproductcatalog/G_2051_AirVacuumPowerHITECH_400ml.pdf. Accessed April 7, 2019.

36. Schindelin J, Arganda-Carreras I, Frise E. Fiji: an open-source platform for biological-image analysis. Nat Methods. 2012;volume 9:676–682.

37. Sezgin M, Sankur B. Survey over image thresholding techniques and quantitative performance evaluation. J Electron Imaging. 2004;13(1):220. doi:10.1117/1.1631316

38. Internal Magnesium Hydroxid Standard from FELMI-ZFE for Particle Size Monitoring with D-Values D10, D50 and D90.

39. Wolfgang S, Nagl C, Kaiser J, August S. Herkungtsanalyse Der PM10-Belastung in Österreich.; 2006.

40. Liste Krebserzeugender Arbeitsstoffe. https://www.ris.bka.gv.at/Dokumente/BgblAuth/BGBLA_2018_II_254/COO_2026_100_2_1557473.pdfsig. Accessed April 27, 2019.

9. Appendix

Results of the GC and FTIR Measurements

Table 9.1 – 9.3 shows the results of the GC and FTIR Measurements of experiment 2, 3 and 4.

Table 9.1: *Results of the GC and FTIR Measurements of experiment 2*

p... possible np... not possible	FTIR	GC	Results
Gas	C / %Vol	C / %Vol	C / %Vol
O_2	np	0.59	0.59
N_2	np	71.95	71.95
H_2	np	7.42	7.42
C_2H_2	0.03	0.00	0.03
C_2H_4	2.23	1.48	1.48
C_2H_6	0.00	0.16	0.16
CH_4	0.87	0.85	0.87
CO	3.74	3.64	3.74
CO_2	9.85	6.61	9.85
DEC	0.81	np	0.81
DMC	0.00	np	0.00
EC	0.00	np	0.00
EMC	0.21	np	0.21
H_2O	0.92	np	0.92
C_6H_{14}	0.00	p	0.00
HF	0.00	np	0.00
C_4H_{10}	0.34	p	0.34
			98.36

Table 9.2: *Results of the GC and FTIR Measurements of experiment 3*

p…possible np…not possible	FTIR	GC	Result
Gas	c/%Vol	c/%Vol	c/%Vol
O_2	np	0	0
N_2	np	70.33	70.33
H_2	np	3.88	3.88
C_2H_2	0.016	0	0.016
C_2H_4	1.06	1.98	1.98
C_2H_6	0	0.19	0.19
CH_4	0.91	0.74	0.91
CO	3.14	1.83	3.14
CO_2	11.94	8.65	11.94
DEC	1.19	np	1.19
DMC	0	np	0
EC	0	np	0
EMC	0.43	np	0.43

H_2O	1.8	np	1.8
C_6H_{14}	0	p	0
HF	0	np	0
C_4H_{10}	0.45	p	0.45
			96.256

Table 9.3: *Results of the GC and FTIR Measurements of experiment 4*

p... possible np... not possible	FTIR	GC	Results
Gas	C / %Vol	C / %Vol	C / %Vol
O_2	np	0.00	0.00
N_2	np	69.79	69.79
H_2	np	3.97	3.97
C_2H_2	0.02	0.00	0.02
C_2H_4	1.06	2.03	2.03
C_2H_6	0.00	0.20	0.20
CH_4	0.91	0.75	0.91
CO	2.91	1.86	2.91
CO_2	10.54	8.91	10.54
DEC	1.19	np	1.19
DMC	0.00	np	0.00
EC	0.00	np	0.00
EMC	0.43	np	0.43
H_2O	1.80	np	1.80
C_6H_{14}	0.00	p	0.00
HF	0.00	np	0.00
C_4H_{10}	0.45	p	0.45
			94.23

Composition of the test gases

Table 9.4 shows the composition of the test gases, which are used for the calibration of the GC. The test gas is provided by Linde Gas GmbH

Table 9.4: *Composition of the test gases used for calibration*

	Test gas 1	Test gas 2	Test gas 3
H_2	21.10	35.10	0.098
N_2	0	0	44.401
O_2	0	0	0
CO	0.103	26.00	55.00
CO_2	57.0	28.02	0.10
CH_4	10.00	4.96	0.10
C_2H_2	4.84	2.43	0.10
C_2H_4	5.00	2.50	0.101
C_2H_6	2.01	0.99	0.10

Comparison elemental composition of Experiment 4

Figure 9.1 – 9.6 compares the elemental composition of both samples of experiment 4.

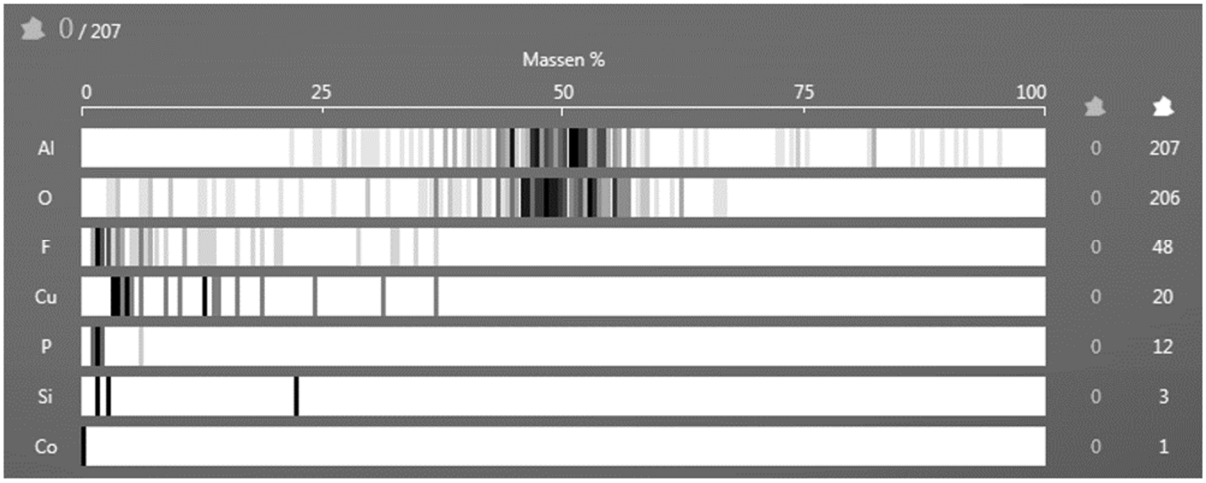

Figure 9.1: *Elemental composition of class 1 of experiment 4*

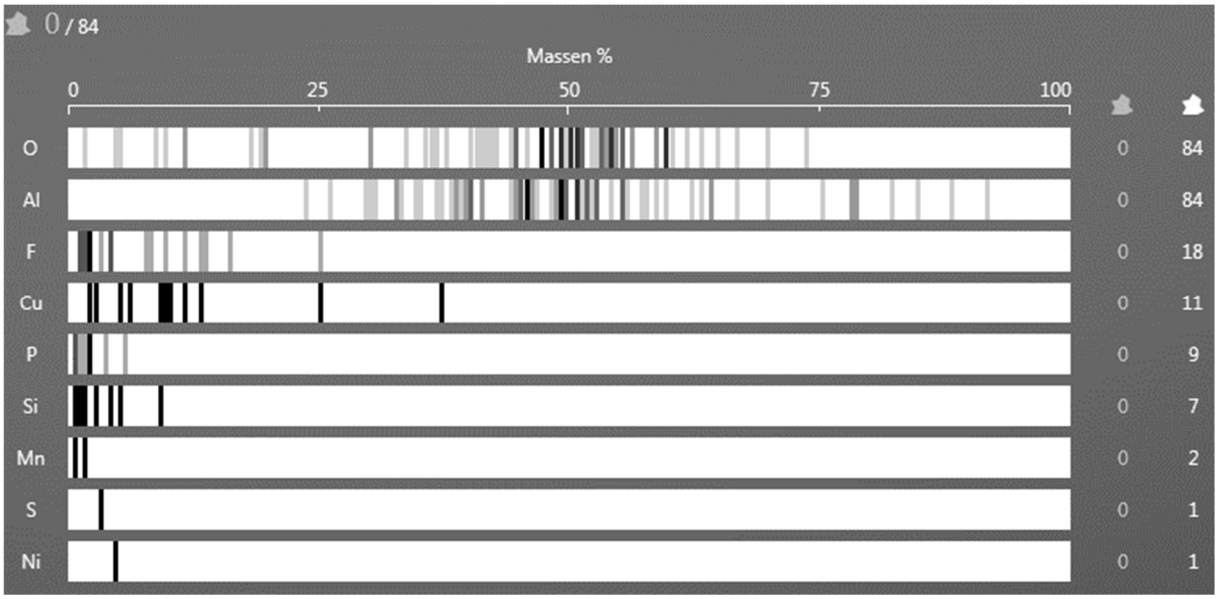

Figure 9.2: *Elemental composition of class 1 of experiment 4*

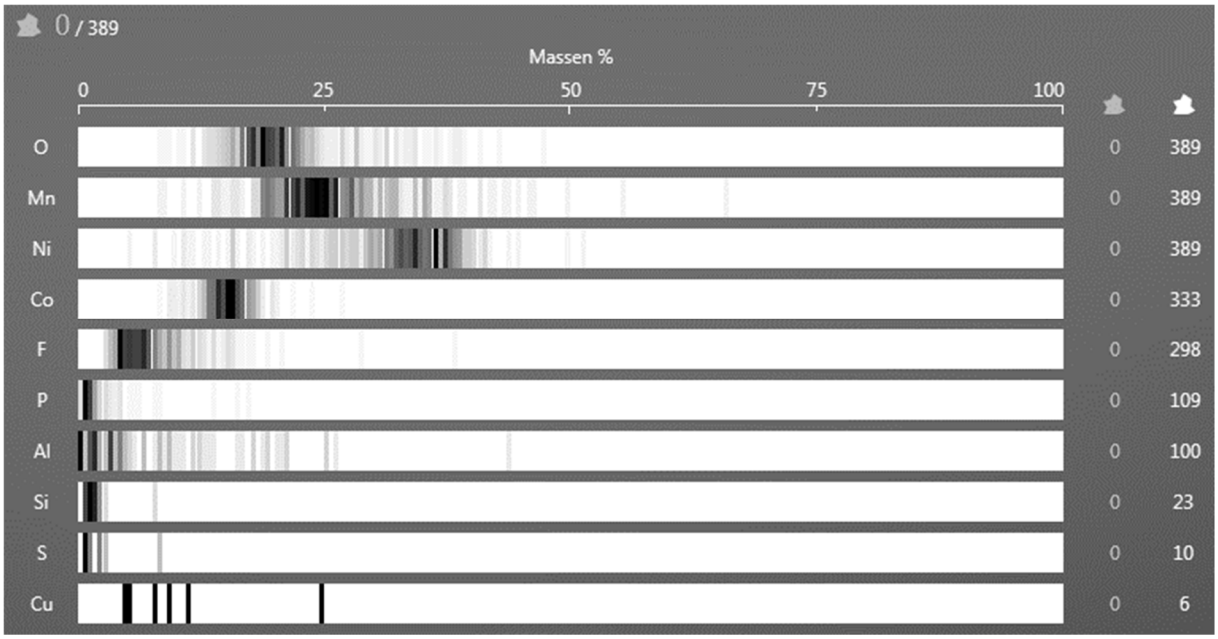

Figure 9.3: *Elemental composition of class 2 of experiment 4*

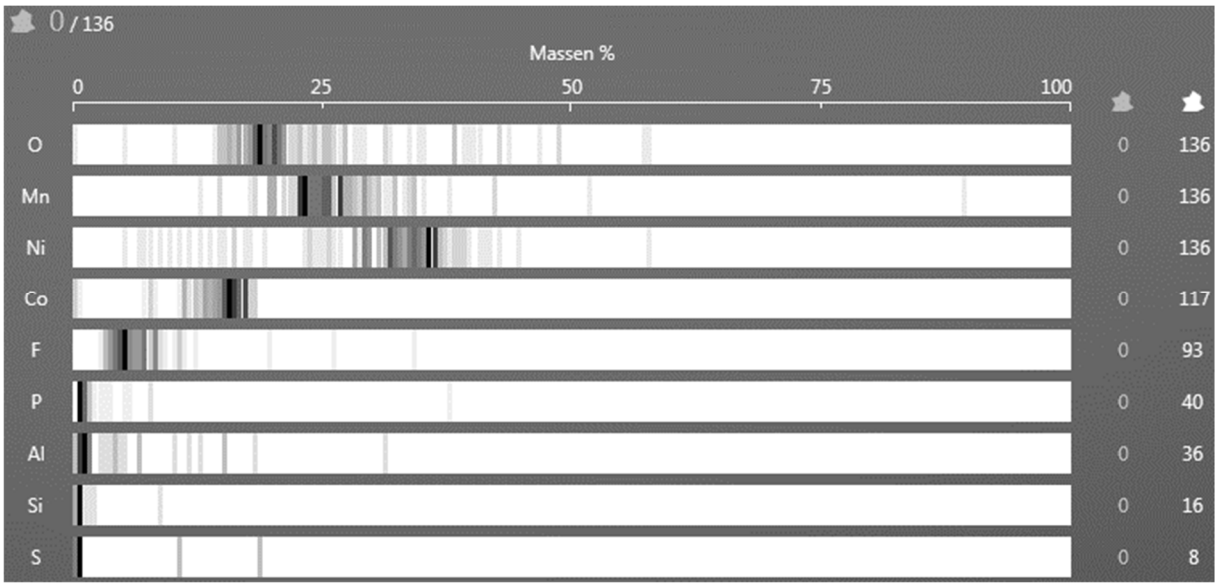

Figure 9.4: *Elemental composition of class 2 of experiment 4*

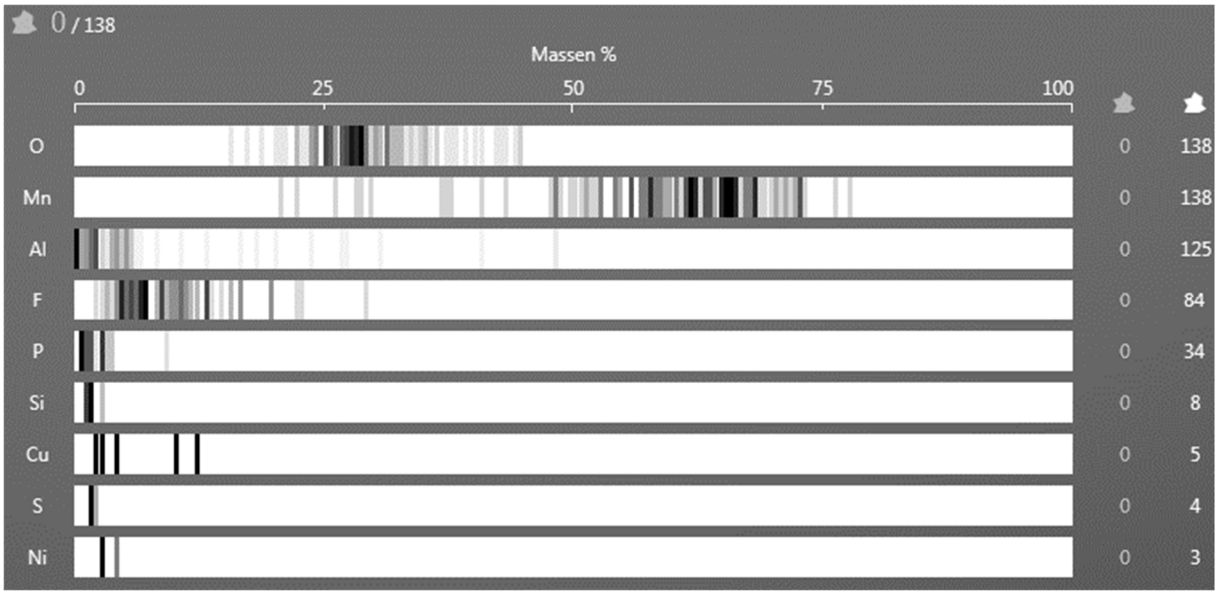

Figure 9.5: *Elemental composition of class 3 of experiment 4*

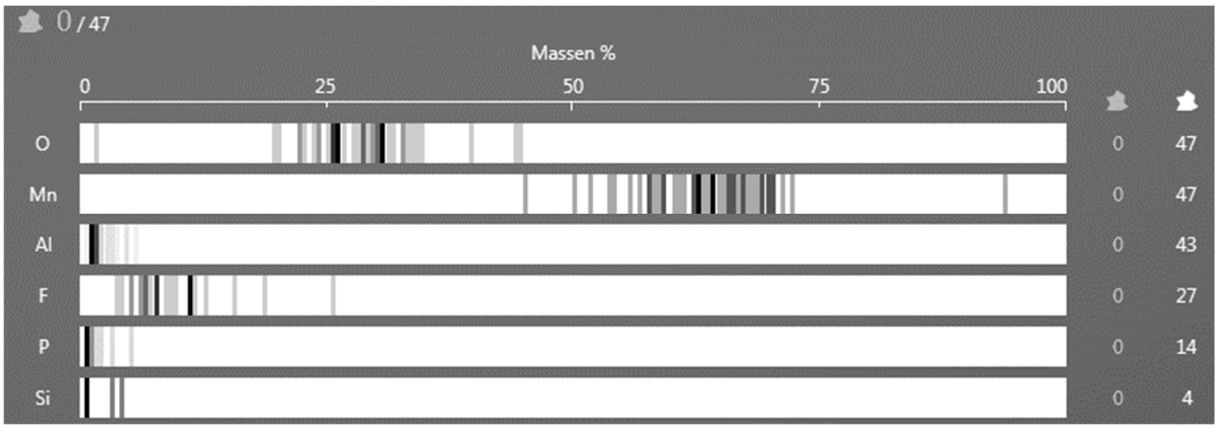

Figure 9.6: *Elemental composition of class 3 of experiment 4*